



מכון ויצמן למדע
WEIZMANN INSTITUTE OF SCIENCE

Thesis for the degree
Doctor of Philosophy

Submitted to the Scientific Council of the
Weizmann Institute of Science
Rehovot, Israel

עבודת גמר (תזה) לתואר

דוקטור לפילוסופיה

מוגשת למועצה המדעית של
מכון ויצמן למדע
רחובות, ישראל

By
Shay Yosef Geula

מאת
שי יוסף גאולה

פענוח התפקיד המולקולרי של מודיפיקציות על רנ"א שליח
והשפעתם על ההתפתחות העוברית ביונקים

**Deciphering the Molecular Role of N6-Methyladenosine mRNA
Modification in Development of Mammalian Stem Cells**

Advisor
Jacob (Yaqub) Hanna
MD PhD

מנחה
יעקוב חנא

February 2016

אדר תשע"ו

Table of Contents

Abbreviations	5
Abstract.....	6
Introduction:	8
Developmental potency	8
Capturing Pluripotency.....	8
Embryonic Stem Cells (ESC).....	8
Somatic cell nucleus transfer (SCNT).....	9
Induced pluripotent stem cells (iPSC).....	10
Epiblast Stem Cells (EpiSC)	10
FIGURE A.....	11
N6-methyladenosine RNA Modification.....	11
N6-methyladenosine writers, erasers and readers.....	12
FIGURE B.....	13
FIGURE C.....	15
Experimental Methods and Procedures.....	16
Stem cell lines and cell culture.....	16
Generation of Mettl3 knockout mice and ESC lines.....	17
Generation of Mettl14 knockout murine ESC lines via CRISPR/Cas9.....	17
Inhibition via siRNA	18
Epigenetic reversion of mouse primed epiblast cells.....	19
<i>In-vitro</i> naïve to primed pluripotent cell conversion	20
Reprogramming of mouse somatic cells to iPSCs	20
LC-MS/MS for m ⁶ A detection and quantification	21
Southern-Blot analysis.....	21
Embryoid bodies and teratoma formation.....	21
qPCR analysis	22
Whole-mount X-Gal staining.....	22
Immuno-fluorescence and immuno-histo-fluorescence staining.....	23
Western blot analysis	24
Cell cycle analysis and Flow cytometry	25
Poly-A RNA Sequencing	25

RNA-seq analysis	26
m ⁶ A IP and Sequencing.....	26
m ⁶ A-seq Analysis	26
Motif search.....	27
m ⁶ A peak scores.....	27
RNA and m ⁶ A Profiles	27
RNA stability assay	28
3' Poly A- RNA-sequencing libraries preparation.....	28
3' Poly A- RNA-sequencing Analysis	29
mRNA Half-Life Calculation.....	29
Ribo-seq analysis.....	30
Stable isotope labeling by amino acids in cell culture (SILAC).....	30
Global similarity matrices	31
Alternative Splicing Analysis	31
RNA editing analysis	31
Results	33
Generation of Mettl3 knockout naïve ESCs with m ⁶ A depleted mRNA	33
Mettl3 KO ESCs resist terminating the naïve ground state of pluripotency.....	39
<i>In vitro</i> -differentiation, embryoid bodies	39
<i>In vitro/vivo</i> -differentiation, teratoma formation.....	42
<i>In vitro</i> -differentiation, EpiSC conversion.....	45
<i>In vivo</i> -differentiation, Blastocyst complementation	45
Rescue of differentiation competence of KO cells by exogenous Mettl3 transgene.....	46
Mettl14 KO ESC loss also m ⁶ A RNA modification and phenocopy the Mettl3 KO phenotype..	51
Divergent response of naïve, primed and metastable mESC to Mettl3-knockdown.....	53
The effect of Mettl3-knockdown on somatic cell reprogramming to pluripotency (iPSC)	58
Mettl3 regulates pluripotent state reconfiguration and lineage priming <i>in-vivo</i>	60
Mettl3 KO embryos show aberrant development in the post-implantation stage.....	60
Mettl3 KO embryos show aberrant pre-implantation markers expression in the post-implantation stage.....	61
Mettl3 KO embryos show do not upregulate normally lineage markers in the post-implantation stage.....	61
The molecular mechanism behind m ⁶ A modification	70
m ⁶ A-seq reveal m ⁶ A modification prevalence in pluripotent and differentiated cells.....	71
m ⁶ A topology and dynamics in pluripotent and differentiated cells	77
Mettl3 depletion leads to specific preferential increase of mRNA levels of methylated transcripts	81

m ⁶ A positively effects the degradation rate of methylated mRNAs.....	84
m ⁶ A mildly represses translation efficiency	88
Effect of m6A methylation on alternative splicing and A-I RNA editing	89
Mettl3 is a study case for how different epigenetic repressors have a divergent effect on naïve and primed murine PSCs	90
Discussion.....	99
m ⁶ A RNA methylation and the decay of naïve pluripotency program	99
Direct and indirect regulatory effects for m ⁶ A on mRNA	102
m ⁶ A as dynamic modification that between different cells state.....	103
Opposing outcomes for defined perturbations in naïve and primed pluripotent stem cells..	103
Supplementary Tables	105
References	107
Student declaration.....	113
List of publication during the course of the Ph.D.	114
Acknowledgements	115

Abbreviations

ESC	Embryonic stem cell
mESC	Mouse embryonic stem cell
hESCs	Human Embryonic Stem Cells
LIF	Leukemia inhibitory factor
iPSC	Induced Pluripotent Stem Cell
m⁶A	N ⁶ -Methyladenosine
METTL3	Methyl transferase-like 3
Dox	Doxycycline
KSR	Knock-out Serum Replacement
FBS	Fetal Bovine Serum
2i	PD0325901 and CHIR99021 (2 inhibitors of the MEK/ERK1/2 and GSK3 β , respectively)
ICM	Inner Cell Mass
EB	Embryonic Bodies
MEFs	Mouse Embryonic Fibroblasts
SCNT	Somatic Cell Nuclear Transfer
PSCs	Pluripotent Stem Cells, including ESCs and iPSCs
EpiSCs	Epiblast Stem Cells
OSKM	Oct4, Sox2, Klf4 and c-Myc
2i/Lif	serum free medium with addition of Lif, Erki and Gsk3 β i
FDR	False Discovery Rate
RPKM	Reads Per Kilobase per Million reads
RQ	Relative Quantity
CRISPR	Clustered Regularly-Interspaced Short Palindromic Repeats

Abstract

While murine naïve and primed pluripotent states retain distinct transcriptional and epigenetic properties, limited knowledge is available on how their circuitry interprets defined perturbations of epigenetic regulators. In this study we identify Mettl3, an N⁶-Methyladenosine (m⁶A) RNA epigenetic modification writer, as a critical regulator for terminating naïve pluripotency and enabling cell priming and commitment to differentiation, both *in vitro* and *in vivo*. Mettl3 knockout pre-implantation epiblasts and naïve ESCs nearly lack m⁶A in mRNAs and are viable. Yet, they fail to adequately terminate the naïve pluripotent state, and subsequently undergo aberrant and partial early lineage priming at the post-implantation stage, leading to embryonic lethality. Our analysis identified m⁶A as a critical determinant that destabilizes naïve specific pluripotency genes (e.g. Nanog, Klf2 and Esrrb), but not Oct4 that is expressed in both pluripotent states. m⁶A restrains transcript stability and translation efficiency, and therefore safeguards rapid exit from naïve pluripotency. On the contrary, Mettl3 depletion in already established EpiSCs perturbs the primed pluripotent state towards differentiation or promotes reversion towards naïve pluripotency, when ground state promoting conditions are provided. In summary, our findings provide, for the first time, evidence for a critical role for an mRNA epigenetic modification in early mammalian development *in vivo*, and identify regulatory modules that functionally influence mouse naïve and primed pluripotency in an opposing manner.

תקציר

תאים פלוריפוטנטים, או תאים רב תכליתיים הם תאי גזע המופקים מעובר מתפתח והם בעלי יכולת להתמייין לכל סוגי התאים בחיה הבוגרת. ניתן להפיק ולגדל בתרבית תאים פלוריפוטנטים משלב הבלסטוציסט שהוא השלב העוברי שלפני ההשרשה ברחם, תאים אלו נקראים תאי גזע "נאיבים". בנוסף לכך ניתן להפיק ולתרבת תאים פלוריפוטנטים מעובר שעבר השרשה ברחם, אך תאים אלו כבר מכילים שינויים אפיגנטיים ולכן הן נקראים תאי גזע "מוחתמים". מעט מאוד ידוע על השינויים האפיגנטיים והגורמים השונים שמבקרים את המצבים הפלוריפוטנטים השונים. בעבודה זו חקרנו שינויים בבקרה של בקרה אפיגנטית ברמת הרנ"א. מולקולת הרנ"א השליח עוברת מתילציה הנקראת m^6A . מתילציה זו מסמנת רבים מהגנים המבוטאים בתאי גזע ואת מרבית מהגנים הפלוריפוטנטים (80%). מתילציה זו (m^6A) נעשית ע"י אנזים הנקרא METTL3 ועם מחיקתו בתאים אנו מאבדים את המתילציה בכל מולקולות הרנ"א השליח. כשאנו מוחקים את הגן שמקודד לחלבון METTL3. אנו מבחינים בתגובה שונה בין שני המצבים הפלוריפוטנטים השונים. התאים המוחתמים עוברים התמיינות מהירה ויוצאים מהמצב הפלוריפוטנטי, אך התאים הנאיבים נשארים במצב הפלוריפוטנטי ומאבדים את היכולת להתמייין בצורה נורמלית. מגמה דומה ניתן לראות גם בעכבר בזמן ההתפתחות העוברית. עוברים שבהם נמחק הגן שמקודד ל METTL3 אינם מצליחים להתמייין בצורה נורמלית ולצאת משלב הבלסטוציסט, ומתים בשלבים מקדמים לאחר ההשרשה. בחיפוש אחר מנגנון מולקולרי שיכול להסביר את התופעה הבחנו כי מולקולות רנ"א שליח שמסומנות במתילציה m^6A הן פחות יציבות, ובעלות זמן מחצית חיים קצר יותר. מולקולות אלו נהיות יציבות יותר כאשר מוחקים את האנזים METTL3 ומונעים את המתילציה. בתאי גזע נאיביים, רוב הגנים הפלוריפוטנטים מסומנים במתילציה m^6A לכן הם הופכים ללא יציבים ומתפרקים מהר בתהליך ההתמיינות. כאשר אנו מוחקים את הגן שמקודד ל METTL3 גנים אלו מאבדים את המתילציה וכתוצאה מכך נהיים יציבים יותר. הם לא מתפרקים מהר מספיק כאשר מגיע איתות להתמיינות והתא נשאר פלוריפוטנטי.

Introduction:

Developmental potency

Life originates following fertilization of the female oocyte by the male spermatoocyte, after which a single cell embryo stage, the zygote, is formed. The zygote subsequently gives rise to an entire multi-cellular organism and has the developmental potential to give rise to any cell type in the embryo proper and extra-embryonic trophoblast tissue that forms the placenta. This unrestricted developmental potential is termed totipotency. During early embryo development the zygote undergoes a number of cell divisions leading to the formation of a dense ball-like structure of sixteen cells called the morula. The cells of the morula are at first closely aggregated, but soon they become arranged into an outer or peripheral layer, the trophoblast, and an inner cell mass¹. This formation is called the blastocyst in which the embryo cells had committed lineage commitment either towards extra-embryonic trophoblast, or the pluripotent pre-implantation epiblast in the inner cell mass (ICM) [FIGURE A]. The ICM of the blastocyst can give rise to all embryonic lineages, but not to any extra-embryonic tissues, and are hence called ‘‘pluripotent’’. The ICM then further gives rise after implantation to the post-implantation pluripotent epiblast that quickly goes on to give rise to all somatic tissues in the embryo. Notably, a small fraction of the post-implantation epiblast cells start reverting back towards pluripotency by becoming primordial germ cells (PGCs) that give rise to sperm and oocytes [FIGURE A]. In the adult somatic tissues different populations of adult stem cells can be found, and can only give rise to cell types within their lineage and are therefore called ‘‘multipotent’’ or ‘‘unipotent’’.

Capturing Pluripotency

Embryonic Stem Cells (ESC)

Capturing pluripotent stem cells and maintaining them *in vitro* in an undifferentiated state has been a difficult task for many years. A major breakthrough was the establishment of immortal pluripotent cell lines from teratocarcinoma tumors.

These cell lines were called embryonal carcinoma cells (ECCs)^{2,3} and could be clonally expanded in culture while retaining pluripotency⁴. The fi

nding that pluripotent cells can be derived from teratocarcinomas, motivated attempts to isolate non-teratogenic pluripotent cells directly from normal embryos.

These efforts led to the derivation of murine embryonic stem cells (ESCs) from the ICM of mouse blastocysts in the 1980's^{5,6} and subsequently, also from human embryos⁷. ESCs are typically derived from the ICM of pre-implantation blastocysts. Under optimized *in-vitro* growth conditions [FIGURE A], ESCs are able to proliferate indefinitely, while maintaining the pluripotent state that shares defining developmental features with that of their founder ICM cells^{1,8}.

The differentiation capacity of ESCs is evident by their ability to incorporate into host blastocyst upon micro-injection, and subsequently differentiate into all cell types in the developing embryo, including the germ cell lineages^{9,10}. And finally by the ability to create a chimeric animal. Another evidence for the pluripotency of ESCs is their ability to form teratomas, a tumor that consist of the 3 germ layers (Endoderm, Mesoderm and ectoderm), upon injection of ESC to immune-deficient mice¹¹. *In-vitro* differentiation of pluripotent stem cells was possible either spontaneously when these adherent cells were detached from the plate and formed embryoid bodies (EB) that contained many cells types, or through specific protocols directed to differentiate the cells to particular cell types such as neurons or cardiomyocytes through control of signaling pathways¹². Finally, mouse ESCs recapitulate epigenetic features of ICM cells, including possessing pre-X inactivation state in female cell lines, and maintaining an open chromatin structure¹³.

Somatic cell nucleus transfer (SCNT)

In parallel to the acquiring of pluripotent stem cells, Briggs, King and Gurdon were pioneering in acquiring pluripotency by somatic cell nucleus transfer (SCNT)^{14,15} In this technology the somatic cell nucleus is “reprogrammed” back to pluripotency by donor host egg or oocyte¹⁶. When nucleus-free oocytes were injected with somatic cell nucleus and stimulated, these zygote-like cell was able to continue to develop and form

an embryo and a whole animal. ESCs can be derived from SCNT blastocysts and these cells resemble ESCs from regular fertilization embryos. SCNT is technically inefficient and requires a large number of non-fertilized oocytes. This technology is limited for application in humans for ethical reasons (generation of new lines require human oocyte donations).

Induced pluripotent stem cells (iPSCs)

After SCNT revealed the plasticity and feasibility of reprogramming the somatic cells, the search for different factors from the pluripotent/totipotent state that can reprogram the somatic cells have been continued. In 2006, Shinya Yamanaka found that transfection of somatic cells with 4 embryonic transcription factors: Oct4, Sox2, Klf4 and Myc (OSKM) reprogrammed the cells to pluripotency¹⁷. These induced pluripotent stem cells (iPSCs) had differentiation potential identical to embryonic stem cells (chimera formation, teratoma formation and in-vitro differentiation) and could proliferate *in vitro* indefinitely. iPSCs can be derived from different somatic cells, including skin fibroblasts and B cells¹⁸, and also from human somatic cells¹⁹. The discovery of iPSCs revolutionized the stem cells field and became the new hope for patient specific regenerative medicine and for human diseases modeling.

Epiblast Stem Cells (EpiSC)

In 2007, a new type of pluripotent stem cells, named epiblast stem cells (EpiSCs), was isolated from the post-implantation epiblast of day E5.5-E7.5 murine embryos [FIGURE A]²⁰. EpiSCs express pluripotency regulator genes such as Oct4 and Sox2, but differ from the ICM-derived ESCs in diminished expression of other bona fide pluripotency genes including Nanog, Esrrb, Rex1 and Klf2, 4, and 5. In comparison to ESCs, EpiSCs are epigenetically and developmentally restricted as evident by their initiation of X chromosome inactivation in female cell lines, and reduced ability to contribute to chimera formation upon blastocyst micro-injection. The cytokines required for the maintenance of EpiSCs in a pluripotent state, bFGF and Activin, are different from those required by ICM-derived mouse ESCs. Since EpiSCs demonstrate lower developmental potential capacity, their pluripotent state is called “primed pluripotency”, while developmentally unrestricted ESCs are in a “naïve pluripotent” state, also referred

to as the “ground state of pluripotency”. **The molecular networks governing the primed pluripotent state and how they compare to those active in naïve ESCs remain poorly understood.**

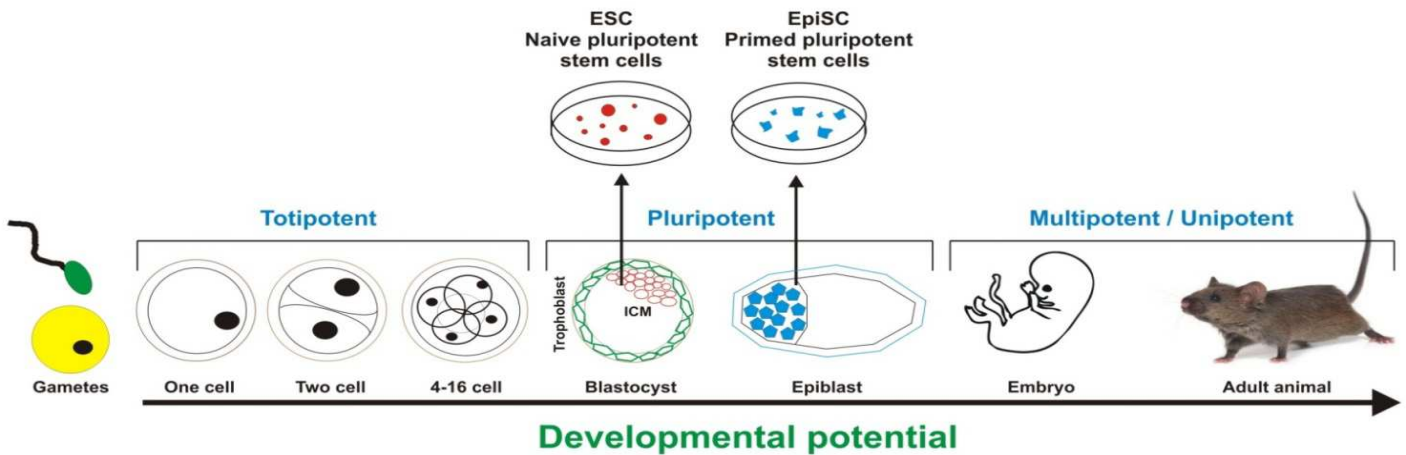


FIGURE A: Basic developmental progress from zygote to adult animal. Capturing pluripotency and derivation of embryonic stem cells *in-vitro* is possible from two different stages – pre-implantation ICM epiblast and post-implantation Epiblast.

N6-methyladenosine RNA Modification

Epigenetic changes in the cell are one of the key factors that regulate cell fate during differentiation and during embryonic development²¹. Epigenetic mechanisms include reversible modifications such as DNA methylation (5-Methylcytosine) and histone protein modifications (Methylation, Acetylation, etc.). These chemical tuning marks regulate gene expression by altering DNA accessibility and by recruiting specific DNA binding proteins. According to the central dogma of molecular biology, the information passes from DNA to **RNA** and then to protein. While RNA is a central player in this dogma, until recently, its chemical modifications were overlooked [FIGURE C]. RNA is decorated by more than 100 different chemical modifications, this modification are done on mRNA, rRNA, tRNA, small nuclear RNA (snRNAs) and small nucleolar RNAs (snoRNAs)²², but their function is still not clear. In the past decade, large efforts were invested in discovering one of the most abundant modifications; N6-methyladenosine (m^6A) that occurs on mRNA^{23–25}.

m⁶A was first discovered on polyadenylated RNA in 1974^{26,27}, these early studies provided evidence that m⁶A is present in mammalian mRNA and in RNA encoded by diverse viruses²⁸⁻³⁰. Subsequent studies showed that m⁶A is a prevalent nucleotide in poly(A) mRNA from nearly all higher eukaryotes and plants^{31,32}. This modification is widely conserved among eukaryotes, from yeast, through plants and flies to mammals. The amount of m⁶A in isolated polyadenylated mRNA was estimated to be 0.1-0.4% of total adenines (2-5 m⁶A sites per mRNA molecule)^{24,33}. M⁶A modification does not influence Watson-Crick base pairing and it is not susceptible to chemical modification like bisulfate that enable the detection of 5-Methylcytosine. That limited detection strategies hamper research of this modification and its global influence in molecular cell biology.

In 2012, the field of m⁶A modification research was revolutionized by a new method of m⁶A RNA immunoprecipitation, followed by high-throughput sequencing (MeRIP-Seq/ m⁶A -seq) that mapped for the first time the m⁶A sites in mammals^{24,33}. m⁶A is prevalent, being distributed on more than 7000 mRNAs and 300 non-coding RNAs. The modification occurs on a consensus motif (Purine(G>A)m⁶AC(A/C/U)) and is enriched around stop codons, 3' untranslated regions (UTRs) and within long exons. The modification sites are highly conserved between human and mouse, but also present dynamic changes between different types of stimuli²⁴.

N6-methyladenosine writers, erasers and readers

The m⁶A methyl-transferase complex (MT) was isolated biochemically for the first time from HeLa cells nuclear lysate¹⁰. From this, 200kDa, complex only one protein was identified MT-A70 or METTL3 (Methyl transferase-like 3). Follow-up work also identified METTL14 (Methyl transferase-like 14)³⁴, and the regulatory unit WTAP (Wilms tumour 1-associated protein)³⁵ as part of the methyl-transferase complex. Knock-down studies of the different components individually showed between 30-50% decrease in m⁶A levels on mRNA^{24,34,36}. *In vitro* studies showed that the complex of METTL3-METTL14 synergy methylated RNA probes 5 time fold as each individual methylase. Additionally³⁴, METTL3 knock-down can also lead to apoptosis, probably by activation of p53-mediated pathway^{24,34}.

Recently, two m⁶A mRNA demethylase enzymes were discovered in mammals^{25,37}, Fat mass and obesity-associated protein (FTO) and (ALKBH5) α-ketoglutarate-dependent dioxygenase alkB homologue 5. Both enzymes reduce m⁶A levels when over-expressed, and increase m⁶A levels by 9-23% when knocked-down^{25,33,37}. However, MeRIP–Seq on FTO KO mouse shows that this reduction is visible in only a few subsets of m⁶A-containing mRNAs^{25,38}. The presence of these m⁶A erasers suggests that m⁶A modifications are dynamic and reversible, at least to some extent, similar to DNA and protein modifications.

RNA pull-down experiments identified several proteins that predominantly bind to methylated RNA (YTHDF1,2,3 and ELAVL1)^{24,36,39}. Extensive studies on YTHDF2 in HeLa cells showed that its binding motif is identical to m⁶A motif, and by this binding, YTHDF2 actively regulates m⁶A-dependent RNA degradation³⁹. Other m⁶A reader proteins may affect RNA splicing, storage, trafficking and translation.

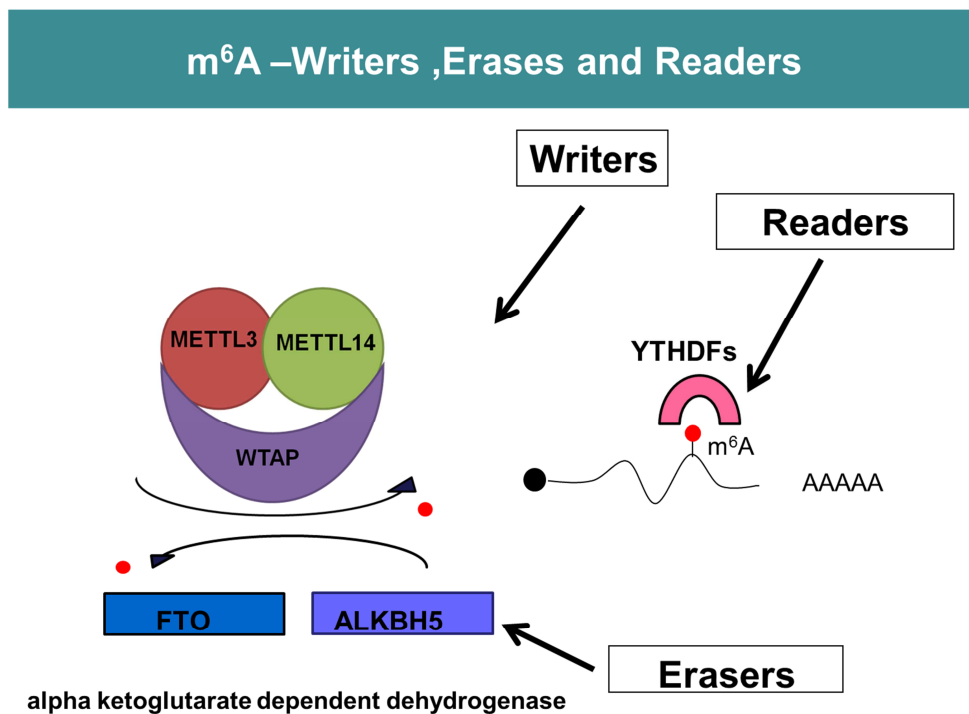


FIGURE B: N⁶-methyladenosine writers, erasers and readers demonstrate m⁶A role in epigenetic regulation.

The concept of m⁶A writers, erasers and readers (FIGURE B) emphasizes the role of this modification in the epitranscriptomic regulation of gene expression (FIGURE C). The original studies in the m⁶A field mainly focus on the biochemical characterization of the protein and enzyme that modulate this modification or try to map and identify the site and the location in which this modification appear. In my Ph.D. work I tried to explore this new emerging field of RNA epigenetic and how it is influence on mammalian development, cell differentiation and pluripotent transition between the primed and naïve states. I probed m⁶A RNA modification in the well-characterized *in vivo* development model of the mouse embryo, and in matched *in vitro* models of embryonic stem cells in culture. I show that Mettl3 and m⁶A have a major role in safeguarding the fidelity of naïve and primed pluripotent states maintenance and transitions, both *in vitro* and *in vivo*. Mettl3 knock-out leads to profound m⁶A depletion in naïve ESCs, resulting in a “hyper-pluripotent” phenotype in which the cells are locked in a naïve state and severely resist to undergo robust priming *in vitro* and *in vivo*. The latter results in embryonic defects as early as E5.0-6.5, and to embryonic lethality. M⁶A marks transcripts of key naïve pluripotency promoting genes and mediates transcript degradation and reduces translation efficiency. Therefore, Mettl3 ablation leads to the hyper-stabilization of the naïve pluripotency circuitry. Finally, our study highlights that depleting m⁶A in already established primed pluripotent cells *in vitro* leads to an opposite effect to that observed in naïve pluripotent cells, and compromises the stability of primed pluripotency due to predominant over-stabilization of lineage commitment transcripts, shifting the cell fate balance toward differentiation.

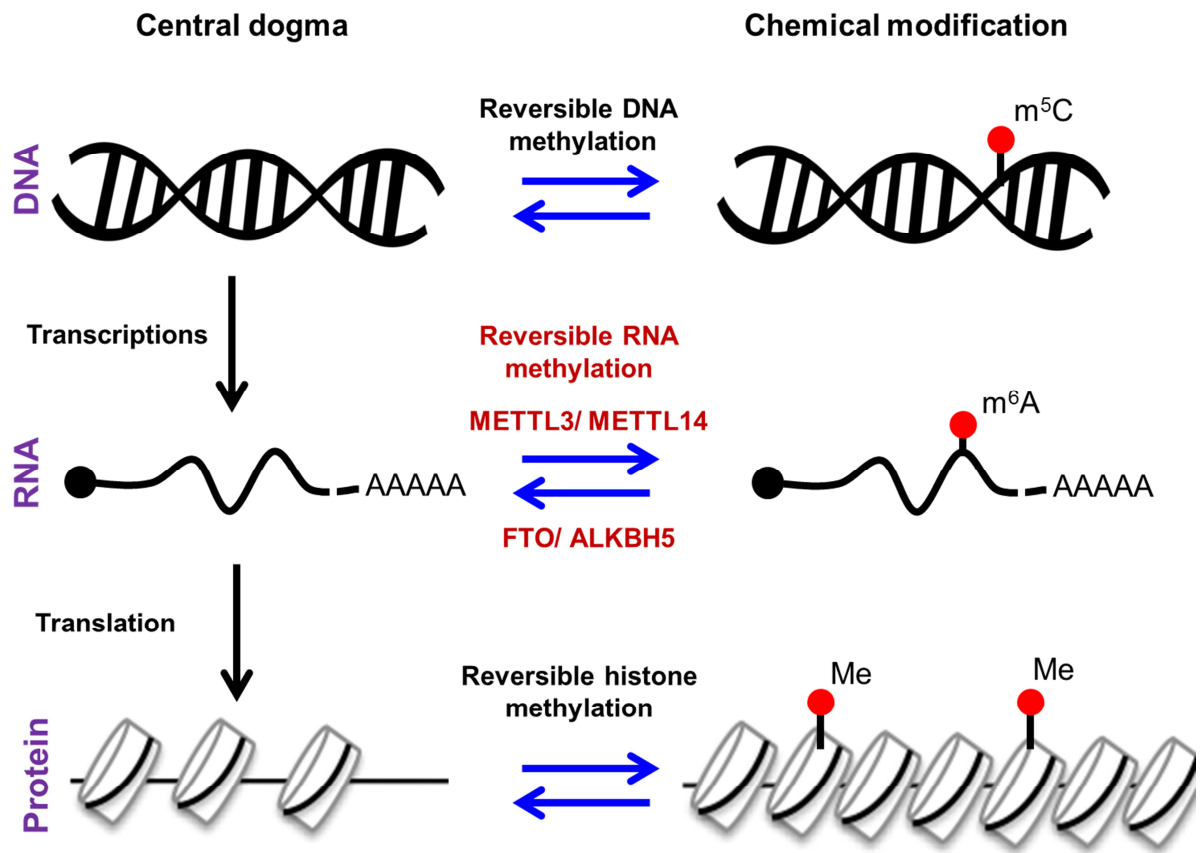


FIGURE C: N6-methyladenosine can serve as a new regulator at the epitranscriptomic level of the cell and influence the central dogma of genetic information flow in the cell.

Experimental Methods and Procedures

Stem cell lines and cell culture

Maintenance of ground state naïve murine pluripotent cells was conducted in FBS free N2B27-based media as described previously⁴⁰. Briefly, 500mL of N2B27 media was generated by including: 240 mL DMEM/F12 (Biological Industries – custom made), 240 mL Neurobasal (Invitrogen; 21103), 5 mL N2 supplement (Invitrogen; 17502048), 5 mL B27 supplement (Invitrogen; 17504044), 1 mM glutamine (Invitrogen), 1% nonessential amino acids (Invitrogen), 0.1 mM β -mercaptoethanol (Sigma), penicillin-streptomycin (Invitrogen), 5 mg/mL BSA (Sigma). Naïve conditions for murine ESC included 10 μ g recombinant human LIF (Millipore; LIF1005) and small-molecule inhibitors CHIR99021 (CH, 1-3 μ M- Axon Medchem) and PD0325901 (PD, 1 μ M - TOCRIS) termed 2i. Primed N2B27 media for murine cells (EpiSCs) contained 8ng/ml recombinant human FGF2 (Peprotech Asia), 20ng/ml recombinant human Activin (Peprotech), and 1% Knockout serum replacement (KSR- Invitrogen). For FBS/LIF growth conditions, ESCs were expanded in 500mL of High-glucose DMEM (Invitrogen), 15% USDA certified fetal bovine serum (FBS- Biological Industries), 1 mM glutamine (Invitrogen), 1% nonessential amino acids (Invitrogen), 0.1 mM β -mercaptoethanol (Sigma), penicillin-streptomycin (Invitrogen), 5 μ g recombinant human LIF (Prepared in house). Cells were maintained in 20% O₂ conditions on irradiation inactivated mouse embryonic fibroblast (MEF) feeder cells, or fibronectin coated plates where indicated. Naïve pluripotent cultures were passaged following 0.2% trypsinization, while primed stem cell cultures were passaged every 3–4 days enzymatically with collagenase type IV (Invitrogen; 1 mg/mL) (with or without pre-treatment with ROCK inhibitor). Chromosomal karyotyping of ESC lines was performed by Multicolor Karyotyping & FISH system (HiSKY) from ASI on 20 metaphase spreads. Cell counts and growth curves were conducted by measurement on Innovatis Cedex XS platform (Roche) according to manufacturer's instructions.

Generation of *Mettl3* knockout mice and ESC lines

Stem cell lines and mice deficient for *Mettl3* were generated by targeted disruption of the endogenous *Mettl3* locus via homologous recombination. A construct, taken from Knockout Mouse Project Repository (*Mettl3*:tmla(KOMP)Wtsi), introduced loxP sites, spanning the fourth exon of *Mettl3*. The targeting of this construct resulted an out-of-frame and truncated product, and introduced LacZ reporter cassette driven by the endogenous *Mettl3* promoter. 50µg DNA of the targeting construct was linearized and electroporated into V6.5 ESC line that was then subjected to selection with G418 (300microg/ml). After 10 days of selection, resistant clones were analyzed for correct targeting of 5' and 3' arms by PCR. Excision of Exon 4 and resistance cassette was done by transfection with pPac-Cre construct and sub-cloning, followed by genotype validation by PCR. *Mettl3*^{+/-} ESC were injected to BDF1 host blastocyst and chimeric mice were generated. Chimeric male mice were mated with C57BL/6 females. F1 offspring (*Mettl3*^{+/-}) were screened for germline transmission by their agouti coat color and validated by PCR of LacZ transgene reporter. In order to generate *Mettl3*-deficient mice, F1 offspring were crossed on C57BL/6 background for 3 generations, and offspring pups or embryos were validated as *Mettl3*-deficient if they were *Mettl3*-Exon4 negative and LacZ positive. Validation was carried out by PCR or by *Mettl3* antibody staining. In order to generate *Mettl3*-deficient ESC line, *Mettl3*^{+/-} mice were crossed and E3.5 embryos were flushed and transferred to MEF coated 96-well-plates, cultured in N2B27 2i/LIF. ESC expansion clones were genotyped by PCR and validated as *Mettl3*-deficient by qPCR and by Western blot.

Generation of *Mettl14* knockout murine ESC lines via CRISPR/Cas9

In order to knock out *Mettl14* gene, oligos encoding gRNAs targeting this gene were inserted into px335 vector⁴¹. Unique gRNA sequences were chosen with the help of Zhang Lab website <http://www.genome-engineering.org/crispr/> (Fig. 13). 100 µg of resulting construct and 10 µg of GFP expressing vector were electroporated into naïve V6.5 mESC. 3 days later GFP expressing cells were sorted by FACS and seeded at low density. 9 days after seeding, colonies were picked for each experiment and genomic DNA was extracted. DNA was analyzed by High Resolution Melt assay (HRM) using

MeltDoctor reagent (Life Technologies) and the clones that showed reduced T_m for both alleles, compared to wild-type controls, were expanded for further validation analysis. In these selected clones targeted locus was amplified and sequenced. Primers for HRM of Mettl14 locus were: Forward: TGTTCCTGGTTTGGCAGGT; Reverse: CACTAATGCTCCCTCCCACC. All relevant plasmids have been directly deposited by our group and are made available through Addgene.

Inhibition via siRNA

Inhibition via siRNA for Mettl3 specific inhibition, male C57BL/6 and C57BL/6x129Jae F1 V6.5 ES and EpiSC lines carrying Oct4-GFP knock-in reporter were used for evaluating effect of Mettl3 depletion on pluripotent cell stability. Mettl3 siRNA (stealth MSS285706 (targeted sequence: GCCAAGCCAGGAGCUUGCUCUUACA), MSS285707 (targeted sequence (CAGGAGAUCCUAGAGCUAUUAAAUA) and the control siRNA (stealth 12935-300) were purchased from Invitrogen. 25 pmol siRNA or control was used for each transfection of pluripotent cells by using LipofectamineTM RNAiMAX (Invitrogen) according to manufacturer's instructions. For naïve and primed pluripotency screen in Figure 1A and Figure S1AB, Oct4-GFP^{+/+} knock-in reporter mice (B6;129S4-Pou5f1^{tm2(EGFP)}Jae/J – Jackson stock 008214) are maintained on C57BL/6 background in our lab for over 10 generations. Male ESC and EpiSC lines were derived from E3.5 and E6.5 embryos in naïve and primed conditions, respectively (13). Cell lines were validated for naïve and primed features pluripotency (including expression of Esrrb, Fgf5, Oct4 enhancer activity) (13). For screening for epigenetic factors that destabilized naïve or primed pluripotent cells, cells were expanded in feeder free fibronectin (2 µg/ml) coated plates at 20% O₂, 5% CO₂. Cells were transfected with 25 pmol of different siRNAs (Invitrogen) in 2 rounds of transfection separated by 72 hours (h) as indicated in Figure 41. After 10 days, cells were harvested and analyzed by FACS for GFP. Transfections were conducted with RNAiMAX (Invitrogen) according to manufacturer instructions for 24 hours. All siRNA mixes used were validated for >70% efficiency knockdown as determined by qPCR in ESCs. In Figure 41, the following Stealth siRNA mix from Life technologies were obtained: Gadd45g siRNA (MSS248270, MSS248271, MSS248272), Oct4 (Pou5f1) siRNA (MSS237605, MSS237606, MSS237607), Sox2

siRNA (MSS277199, MSS277200, MSS277201), Tcf3 siRNA (MSS210710, MSS210711, MSS277871), Tbx3 siRNA (MSS210620, MSS210621, MSS277825), Dnmt3b siRNA (MSS203634, MSS203635, MSS274012), Tet1 siRNA 3 (MSS284895, MSS284896, MSS284897), Satb1 siRNA (MSS208797, MSS208798, MSS276943), Satb2 siRNA (MSS210341, MSS210342, MSS210343), Klf5 siRNA (MSS202449, MSS202450, MSS273427), Hdac3 siRNA (MSS205073, MSS205074, MSS205075), Hdac2 siRNA (MSS205071, MSS205072, MSS274783), Hdac1 siRNA (Utx (MSS212321, MSS212322, MSS212323), Jmjd3 siRNA (MSS211259, MSS211260, MSS211261), Jarid1b siRNA (MSS233166, MSS233167, MSS293343), Jarid1a siRNA (MSS277953, MSS277954, MSS277955), Dnmt1 siRNA (MSS203624, MSS274010, MSS274011), Dnmt3a siRNA (MSS203630, MSS203631, MSS203632), Mbd1 siRNA (MSS206537, MSS206538, MSS206539), Mbd2 siRNA (MSS206540, MSS206541, MSS206542), Mbd3 siRNA (MSS237238, MSS275658, MSS275659), Wdr5 (MSS274289, MSS274290, MSS274291), Arid1a siRNA (MSS234962, MSS234963, MSS234964), Mettl3 siRNA (MSS226050, MSS285706, MSS285707), Eed siRNA (MSS203789, MSS274071, MSS274072), Suz12 siRNA (MSS225221, MSS225222, MSS225223), Rest siRNA (MSS208605, MSS276827, MSS276828), Rnf4 siRNA (MSS208665, MSS276866, MSS276867). Control siRNA stealth 12935-300 was used in the screen. siRNAs for Hdac1 (GS433759) was obtained from Qiagen. The following Stealth siRNAs (Invitrogen) were used for partial rescue experiment: Nanog AM16708 (targeted sequence: ACGCUGCUCCGCUCUCAUAATT); Esrrb (MSS240926 – targeted sequence GCCAUCAAAUGCGAGUACAUGC UUA), (MSS240927 – targeted sequence GGCGUUCUUCAAGAGAACCAUUC AA) (MSS240928 – targeted sequence GCCAUUGACUAAGAUCGUCUCGAAU); Klf4 (MSS275229 – targeted sequence CGGCCGAGUUGGACCCAGUAUACA) (MSS275240 – targeted sequence UUCAUGUGUAAGGCAAGGUGGUCCG) (MSS275241 – targeted sequence ACGACCUCUGGACCUAGACUUUAU).

Epigenetic reversion of mouse primed epiblast cells

Male naive V6.5 mouse ES cells carrying delta-PE-Oct4-GFP naïve specific transgenic reporter (Addgene 52382)(43) were maintained on fibronectin coated plates in

N2B27 FGF2/Activin conditions. For epigenetic reversion of murine EpiSCs to naïve pluripotency, 5000 single EpiSCs were passaged into N2B27 10% KSR, LIF conditions on fibronectin (2µg/ml) and DR4 feeder cell coated plates (without overexpression of exogenous reprogramming factors). After 48 hours 2i was supplemented for additional 6 days. As epigenetic reversion assay involved single cell plating, EpiSC growth medium was supplemented with ROCK inhibitor for 24 hours before trypsinization and throughout the entire assay. *Mettl3* siRNA (stealth MSS285706, MSS285707) and the control siRNA (stealth 12935-300) were purchased from Invitrogen. 10 nM siRNA was used for each transfection with Lipofectamine RNAiMAX (Invitrogen) according to manufacturer's instructions. GFP⁺ colonies were counted at day 8. All reprogramming experiments were done in triplicates.

***In-vitro* naïve to primed mouse pluripotent cell conversion**

For epigenetic reversion of murine naïve pluripotency ESC to primed, 5×10^5 ESC were passaged from N2B27 2i/LIF conditions to Fibronectin (2µg/ml) coated plates with N2B27 FGF2/Activin conditions. Converted cells were maintained permanently in these conditions and passaged with collagenase type IV on Fibronectin (2µg/ml) or feeder MEF-coated plates.

Reprogramming of mouse somatic cells to iPSCs

Mice carrying collagen locus insertion of STEMCCA DOX inducible OKSM (Oct4, Klf4, Sox2, c-Myc) polycistronic vector and *ROSA26* locus insertion of consistently active M2rtTA⁴² were crossed or mated with Oct4-GFP reporter mice (GOF18) for generating secondary double heterozygote mCol-STEMCCA-OKSM^{+/-} ROSA26-M2rtTa^{+/-} (Jackson laboratories mouse strain: #011001) MEFs from E13.5 embryo. 1×10^4 MEF cells were plated on gelatin covered plate and reprogramming was induced by adding 2ng/ul Doxycycline (DOX). siRNA transfections were started at -2, -1, 0, +2, +3, +4 days relative to Doxycycline addition as indicated for each experimental scheme. Reprogramming was conducted in FBS/LIF conditions and under physiological 5% O₂. iPSC formation was analyzed by AP staining and colony quantification, or by

FACS analysis for Oct4-GFP/SSEA-1 pluripotency marker expression. All conditions were conducted in technical triplicates for calculating average and s.d.

LC-MS/MS for m⁶A detection and quantification

Polyadenylated RNA was purified from total RNA by two rounds of oligo-dT selection (GenElute mRNA miniprep, Sigma-Aldrich) followed by one round of rRNA depletion (Ribo-Zero Gold, epicentre). 300 ng of purified RNA were digested by P1 nuclease (2 units) in 25 μ l buffer containing 25 mM NaCl and 2.5 mM of ZnCl₂ for 2 hours at 37 °C. Buffer pH was adjusted by addition of NH₄HCO₃ (1 M, 3 μ l), and alkaline phosphatase (0.5 unit) was added for an additional 2-hour incubation at 37 °C. Samples were diluted to 50 μ l, filtered (0.22 μ m, Millipore) and injected into a C18 reverse phase column coupled on-line to Agilent 6410 QQQ triple-quadrupole LC mass spectrometer in positive electrospray ionization mode. Quantitation was performed based on nucleoside-to-base ion transitions (282-to-150 for m⁶A, 268-to-136 for A) and a standard curve of pure nucleosides.

Southern-Blot analysis

Genomic DNA was extracted from each Neomycin resistant targeted subclones. 10-15 μ g of genomic DNA was digested with EcoRI or AflIII restriction enzyme for 6 hours and separated by gel electrophoresis. The DNA was transferred to a nitrocellulose membrane that was next hybridized with a radioactive labeled probe (against neomycin transgene, Geula et al, Supplementary Table 4) using Random Primers DNA Labeling System kit (Invitrogen). The membrane was exposed to X-ray sensitive film (Fujifilm) for detection of corrected size band formation.

Embryoid bodies and teratoma formation

For embryoid body (EB) *in vitro* differentiation 5x10⁶ ESC were disaggregated with trypsin and transferred to non-adherent suspension culture dishes, and cultured in MEF medium (DMEM supplemented with 1% L-Glutamine, 1% Non-essential amino acids, 1% penicillin/streptomycin and 15% FBS) for 8-21 days. For teratoma generation,

2×10^6 ESC were injected subcutaneously into both flanks of recipient SCID immunodeficient mice. Six weeks after initial injection tumors were harvested for paraffin embedding and sectioning or for FACS analysis. For Mouse embryo micromanipulation naïve ESCs expanded in 2i/LIF were injected into BDF2 diploid blastocysts. Microinjection into blastocysts placed in M16 medium under mineral oil was done by a flat-tip microinjection pipette. A controlled number of 10-12 cells were injected into the blastocyst cavity. After injection, blastocysts were returned to KSOM media (Invitrogen) and placed at 37°C until transferred to recipient females. Ten to fifteen injected blastocysts were transferred to each uterine horn of 2.5 days post coitum pseudo-pregnant females. Determining germ-line transmission was performed by mating chimeric animals with C57BL/6 females, and checking for agouti colored pups. For All animal studies were conducted according to the guidelines and following approval of the Weizmann Institute of Science (IACUC approval #00960212-3).

qPCR analysis

Total RNA was isolated using the Direct-zolTM RNA miniprep (Zymo Research), gDNA was omitted by on-column DNase treatment. One microgram of RNA was reverse-transcribed using High-Capacity cDNA Reverse Transcription Kit (Applied Biosystems). Quantitative PCR analysis was performed in triplicate for each sample by using 10ng of the reverse transcription reaction in a Viia7 platform (Applied Biosystems) with Fast SYBR[®]Master Mix (Applied Biosystems). Primers used for amplification are indicated in **Supplementary Table 4**. Data were extracted from the linear range of amplification. Error bars indicate standard deviation of triplicate measurements for each measurement.

Whole-mount X-Gal staining

The noon of the vegetal plug was considered as E0.5. Embryos were dissected out of the uterus, separated from extra-embryonic membranes, and placed in cold phosphate buffered saline (PBS, PH7.2). E8.5-E12.5 embryos were then fixed in 4% paraformaldehyde (PFA) in PBS for 15 min at 4°C with gentle shaking, washed twice for 10 min in PBS (1st wash at 4°C and 2nd at RT), equilibrated twice for 15 min each at RT

in a X-Gal washing buffer (2 mM MgCl₂, 0.01% sodium deoxycholate, 0.02% NP-40 in PBS). Staining was performed in freshly prepared X-Gal washing buffer containing 5 mM potassium ferricyanide, 5 mM potassium ferrocyanide and 1 mg/ml X-gal at 30°C for 1-16 hours, with shaking and protection from light. When the desired intensity of staining was achieved, usually within 12 hours, embryos were washed twice in pre-warmed PBS, post-fixed O.N in 4% PFA in PBS at 4°C, rinsed twice in PBS, dehydrated in 70% ethanol, and stored at 4°C. Throughout the manuscript, experimental and control samples were handled for staining, exposure and analysis under identical conditions simultaneously to eliminate variability or bias.

Immuno-fluorescence and immuno-histo-fluorescence staining

Immuno-fluorescence on cells was conducted after cells were fixed in 4% paraformaldehyde for 10min at RT, washed three times with PBS and blocked for 15 min with 5% FBS in PBS containing 0.1% Triton X-100. After incubation with primary antibodies (Over night, 4°C in 5% FBS in PBS containing 0.1% Tween20) cells were washed three times with PBST (PBS containing 0.1% Tween20) and incubated with fluorophore-labelled appropriate secondary antibodies purchased from Jackson ImmunoResearch and counter stained with DAPI (1 µg/ml, 0215754; MP Biomedical). Specimens were analyzed on a Zeiss (Oberkochen, Germany) Axioscope microscope, and images were acquired with a Zeiss AxioCam HRM camera. Alkaline phosphatase staining on cells *in vitro* was performed with Vectastain ABC – alkaline phosphatase kit (Vector labs).

For immuno-histochemistry, pre-implantation E3.5 blastocysts were flushed from Mettl3^{+/-} crossed maternal uterus and transferred to watch-glass dish (Genenet), fixed for 15 minutes in 4% PFA in PBS, rinsed three times in PBS containing 3mg/ml PVP (Polyvinylpyrrolidone, Sigma), permeabilized in PBS/PVP with 1% triton X-100 for 30 minutes, and blocked in blocking solution (5% normal donkey serum, 0.05% BSA, 0.01% Tween in PBS) for 1 hour. Embryos were then incubated overnight at 4°C in primary antibodies diluted in blocking solution, washed three times in blocking solution for 15 minutes each, incubated with secondary antibodies for 1 hour at room temperature, counterstained with DAPI for 15 minutes, washed twice in PBS, and mounted in 96 well

glass bottom plates for confocal imaging. Post-implantation embryos were dissected from uterus X-days post coitum (dpc). Embryos fixed in freshly prepared 4% PFA in PBS at 4°C over-night. Afterwards, the tissue was washed in PBS for 10 min, dehydrated and embedded in paraffin using standard procedure. 6 µm sections were cut on a microtome (CM1850, Leica), mounted on Superfrost plus slides (Thermo Scientific, Menzel-Glaser), dried at 38°C for 4h and transfer to H&E or immunofluorescence staining. For immunofluorescence, sections were rehydrated, treated with antigen retrieval, rinsed in PBS for 5 min, and permeabilized in 0.1% Triton X-100 in PBS, then blocked in Blocking solution (5% normal donkey serum in PBST) in humidified chamber for 1 h at RT. Slides were then incubated in the appropriate primary antibody diluted in blocking solution at 4 °C overnight. Sections were then washed three times (5 min each) in PBST, incubated with appropriate fluorochrome-conjugated secondary antibodies diluted in blocking solution at RT for 1 h in the dark, washed once in PBS, counter stained with DAPI for 10 min, rinsed twice in PBS and mounted with Shandon Immu-Mount (Thermo Scientific, 9990412). All images were collected on a Zeiss (Oberkochen, Germany) Axioscope microscope or LSM700 confocal microscope and processed with Zeiss ZenDesk and Adobe Photoshop CS4 (Adobe Systems, San Jose, CA). The following primary antibodies were used: Oct4 (Santa Cruz SC9081 or SC5279), Nanog (Bethyl, A300-397A), SSEA1 (Developmental Studies Hybridoma Bank, MC-480), Mettl3 (Proteintech Group 15073-1-AP), Foxa2 (Santa Cruz,sc-6554) Brachyury (Santa Cruz, sc-17743), Nestin (Millipore, MAB353), Tuj1 (Covance, MMS-435P), Tfe3 (SIGMA, HPA023881), Esrrb (R&D systems, PP-H6705-00), H3K27met3 (Millipore, 07-449), Gata4 (Santa Cruz, sc-1237) Gata6 (R&D systems, AF1700), troponin T (Developmental Studies Hybridoma Bank, CT3), Dnmt3a,b (Imgenex, IMG-268A, IMG-184A), Nanog (eBioscience, 14-5761), Cdx2 (Biogenex, AU392A-UC) and Sox17 (R&D systems, AF1924).

Western blot analysis

SDS/PAGE was performed according to Laemmli and transferred to nitrocellulose membranes for immunostaining. Membranes containing the transferred proteins were blocked with 5% (w/v) non-fat dried skimmed milk powder in PBST and

then incubated with primary antibody in 5% BSA in PBST (Over night, 4°C). Secondary antibodies were horseradish peroxidase-linked appropriate secondary antibodies (Jackson). Blots were developed using ECL (Thermo). The following primary antibodies were used: Mettl3 (Proteintech Group 15073-1-AP), GAPDH, Hsp90, Actin β (Epitomics, 2251-1,1492-1, 1854-1), Oct4 (Santa Cruz, SC9081), Nanog (Bethyl, A300-397A), Klf4 (Santa Cruz, SC20691) Sox2 (Cell Signaling, #2748) Dnmt1 (Cell Signaling, #5032), Dnmt3a,b (Imgenex, IMG-268A, IMG-184A), Esrrb (R&D systems, PP-H6705-00), Foxa2 (Santa Cruz, sc-6554), Klf2 (Millipore, 09-820), Mettl14 (NOVUS Biologicals, NBP1-81392), Wtap (proteintech, 60188-1-Ig).

Cell cycle analysis and Flow cytometry

For cell cycle analysis, 1×10^6 ESCs were incubated with 10 μ M BrdU (SIGMA) for 30 min, then harvested with trypsin, washed with PBS and fixed with ice cold 70% ethanol. The cells were then incubated with 2M HCl for 30 min in RT, washed with PBST, and incubated with FITC conjugated BrdU antibody (Abcam) in 5% BSA in PBST for 1h at 4°C. The cells were afterwards washed and incubated with 20 μ g/ml *propidium iodide* (SIGMA) and RNAaseH (SIGMA) for 30 min at RT. Cells were washed and analyzed by FACS. Flow cytometry analysis and cell sorting were conducted on BD FACS CANTO II analyzed and BD FCAS ARIA III. For surface marker expression analysis, cells were disaggregated with trypsin, washed with PBS and incubated with either: anti-SSEA-1 (BD Bioscience) or anti-Thy1 (CD90, BD Bioscience) in binding buffer (5% BSA in PBST) for 30 min 4°C.

Poly-A RNA Sequencing

Total RNA was extracted from the indicated cell cultures using PerfectPure RNA cultured cell kit (cat#2302340, 5 Prime). To avoid DNA contaminations all samples were treated with DNase (5 Prime). RNA integrity was evaluated on Bioanalyzer (Agilent 2100 Bioanalyzer). Libraries were prepared according to Illumina's instructions accompanying the TruSeq RNA Sample Preparation Kit v2 (RS-122-2001). Sequencing

was carried out on Illumina HiSeq2500 according to the manufacturer's instructions, using 10pM template per sample for cluster generation, and sequencing kit V2 (Illumina).

RNA-seq analysis

Poly-A RNA sequencing was measured in 4 conditions: WT, *Mettl3^{-/-}*, ESC and EB, each condition had 2 duplicates, resulting in 8 RNA-seq samples. The paired-end reads were aligned to mouse genome version mm10 with TopHat2 aligner (v2.0.8b)⁴³, using TopHat2 default input parameters. The number of reads mapped to each of the Ensemble genes (version GRCm38.74) was counted using the HTSeq python package⁴⁴ with the 'union' overlap resolution mode, and `-stranded=no`. Normalized counts were calculated for each gene using DESeq package⁴⁵, or with bioconductor edgeR v.3.2.3⁴⁶ (used for the correlation matrices). DESeq produces counts that are normalized by the sample size, but not by the length of the transcripts. Genes were considered differentially expressed genes if their $FC \geq 2$ and their p value was below $FDR \leq 5\%$ using Benjamini-Hochberg multiple testing adjustment. The normalized expression levels are available alongside the raw data, in NCBI GEO series (Geula et al, 2015).

m⁶A IP and Sequencing

m⁶A mapping was carried out using the m⁶A-Seq protocol as described^{24,47}. In short, RNA samples were chemically fragmented into 100-nucleotide-long fragments and 400 µg of total RNA were subjected to immunoprecipitation (IP) with affinity purified anti-m⁶A rabbit polyclonal antibody (Synaptic Systems). Bound m⁶A-methylated RNA fragments were eluted with free N⁶-methyladenosine (Sigma-Aldrich) and used for library generation. Sequencing was carried out on Illumina HiSeq2500 according to the manufacturer's instructions, using 10pM template per sample for cluster generation, and sequencing kit V2 (Illumina).

m⁶A-seq Analysis

m⁶A IP and total input were measured in ESC (3 biological replicates), EB (3 biological replicates) and fibroblast (MEF, 2 biological replicates). Reads were aligned to

the mouse transcriptome (UCSC mm10) using TopHat2 aligner (v2.0.8b)⁴³. Regions enriched in the IP sample over the input control were identified as m⁶A peaks using MACS2 peak-caller(50) with the following parameters: The "effective genome size" parameter was adjusted to the calculated mouse transcriptome size 994,080,837. Peaks were considered if their MACS2-assigned fold change was $FC \geq 2$ and FDR value $\leq 5\%$, they appeared in at least 2 out of 3 independent biological replicates, and they fall in annotated gene whose expression level was equal or over the first quartile of the expression level of all genes. m⁶A peaks are available alongside the raw data, in NCBI GEO series (Geula et al, 2015).

Motif search

Identified peaks were sorted according to their FC and the top 500 peaks were chosen for *de novo* motif analysis. 101-nucleotide-long sequences derived from the sense strand and centered on the peak summit were used as input for MEME⁴⁸.

m⁶A peak scores

m⁶A peak scores were calculated for all significant peaks in the following way: the number of reads in each peak was counted using bedtools coverage software⁴⁹. This number was normalized by the peak length and by the sample size to give RPKM (reads-per-kilobase-per-million-reads) score. The final score of each peak is the score calculated from the IP sample minus the score calculated from the input sample.

RNA and m⁶A Profiles

Figures of read landscape (e.g. Fig. 28) were generated using UCSC genome browser⁵⁰. Alignment files (.bam) were converted to bedGraph files using genome CoverageBed command from bedtools package (version 2.16.2)⁴⁹. We used a scaling factor (-scale flag) to normalize each sample by its size. The factor is $1/n_i$, where n_i is the number of aligned reads in each sample i . The bedGraph files were then converted to bigwig file using UCSC bedGraphToBigWig software, and were uploaded to UCSC

genome browser as explained in the browser instructions. Profiles are available to view with UCSC genome browser via link http://urlmin.com/ucsc_m6a.

RNA stability assay

For RNA stability 5×10^5 cells were plated on gelatin-coated 6cm plate. 48 hours after the medium replace to fresh medium contain $5 \mu\text{M}$ Actinomycin-D that was used as mRNA transcription inhibitor. Cells samples were harvest in different time point (0,2,4,6,8,10,12h) and total RNA were extract and used for qPCR and for 3' Poly A-RNA-sequencing (described below).

3' Poly A- RNA-sequencing libraries preparation

Total RNA was fragmented into average size of 300 nucleotides by incubation of the RNA in 95°C for 4:30 minutes (NEBNext Magnesium RNA Fragmentation Module). The 3' polyadenylated fragments were enriched by selection on poly dT beads (Dynabeads Invitrogen). Strand specific cDNA was synthesized using a poly T-VN oligo (18 T) and Affinity Script RT enzyme (Agilent). Double strand DNA was obtained using Second strand synthesis kit (NEBNext second strand synthesis module). DNA was purified by adding paramagnetic SPRI beads (Agencourt AMPure XP, Beckman Coulter) pipette-mixed 15 times and incubated for 2 minutes. Supernatant were separated from the beads using a 96-well magnet for 4 minutes. Beads were washed on the magnet with 70% ethanol and then air dried for 4 minutes. The DNA was eluted in EB buffer (10 mM Tris-HCl pH 8.0) by pipette mixing 25 times. For the remainder of the library construction process (DNA end-repair, A-base addition, adaptor ligation and enrichment) a general SPRI cleanup involves addition of buffer containing 20% PEG and 2.5 M NaCl to the DNA reaction. DNA ends are first repaired by T4 polymerase (NEBNext), next, T4 polynucleotide kinase (NEB) adds a phosphate group at the 5' ends. An adenosine base is then added to the blunt-ended fragments, using Klenow enzyme (NEB), and a barcode Illumina compatible adaptor (IDT) was ligated to each fragment using T4 quick ligase (NEB). DNA fragments were amplified by 12 cycles of PCR (Kapa HiFi) using specific primers (IDT) to the ligated adaptors. Library quantity was determined by Qubit

Fluorometric Quantitation (Life Technologies) and the quality of each library was analyzed by TapeStation (Agilent).

3' Poly A- RNA-sequencing Analysis

3'-Poly A-RNA-seq was measured from ESC and EB, WT and *Mettl3*^{-/-}. In each condition, three time points were measured, 0, 4 and 8 hours after Actinomycin-D induction. Reads were aligned to mouse genome version mm10 with BOWTIE2 software⁵¹ using its default parameters. Gene expression levels were estimated in the following way: each gene was divided to 50-bp bins, from its transcription-start-site and to 3kb after its transcription-end-site. The genomic location of the genes was downloaded from UCSC Table browser, “refGene” table. The number of reads in each bin was counted, and the bin with the highest number of reads was chosen as the representative expression level of that gene. Note that in this way, if there are several alternative transcription-end-sites for a specific gene, the transcript with the highest expression is the only one that will be counted. These expression levels were normalized by the sample size, such that each level represents RPM (reads-per-million-reads), and the minimal level was set to be 1. 3' polyA RNA-seq values are available alongside the raw data, in Geula et al GEO files.

mRNA Half-Life Calculation

The half-life of all genes was calculated according to the following equation: $\ln(C_i/C_0) = -kt_i$, where k is degradation rate, C_i is the mRNA value at time i , and t_i is the time interval in hours⁵². We first normalized expression levels to follow median degradation level in mouse ESC, which is 7.1h⁵³. The reason for this normalization is that the number of cells that are used to extract the same amount of RNA after Actinomycin-D treatment is increasing in each time point. We then calculated degradation rate k_i from the normalized expression levels, for each gene and each time point. Half-life $t_{1/2}$ is $\ln(2)/k_a$, where k_a is the average degradation rate measured across the different time points. Using this method we calculated half-life from 3' poly-A RNA-seq data, and from PCR (Fig. 35).

Ribo-seq analysis

Ribosome binding profiles were measured with Ribosomal profiling⁵⁴⁻⁵⁶, in ESC and EB, each in WT and KO conditions. For ribosome profiling cells were treated with Cycloheximide as previously described. Cells were then lysed in lysis buffer (20mM Tris 7.5, 150mM NaCl, 15mM MgCl₂, 1mM dithiothreitol) supplemented with 0.5% triton, 30 U/ml Turbo DNase (Ambion) and 100µg/ml cycloheximide, ribosome protected fragments were then generated as previously described. Reads were aligned to mouse genome version mm10 with TopHat2 aligner⁴³, using TopHat default parameters. Translation levels were estimated for each gene using HTSeq-count and DESeq as explained before. Translation Efficiency was measured for each gene *g* and each condition *i* as $\log_2(\text{Ribo}_{gi}/\text{RNA}_{gi})$. Normalized translation levels (RPM) are available alongside the raw data, in NCBI GEO series (Geula et al, 2015).

RRS values were calculated using mRNA-Seq, Ribo-seq reads as described before⁵⁷. In short- the reads were aligned to the mouse genome (build mm10) using TopHat. For each transcript listed in Ensembl gene list (release 75) we counted the number of reads falling in areas annotated as 3' UTR and CDS. The reads of samples of the same type were averaged and the ratio $\text{count_CDS}/\text{count_UTR}$ was computed for each gene once in the mRNA-Seq and once in the Ribo-seq. The ratio between these 2 ratios is the

$$\text{RRS} = (\text{Count_CDS}/\text{Count_UTR})_{\text{Ribo-seq}} / (\text{Count_CDS}/\text{Count_UTR})_{\text{mRNA-Seq}}$$

The ratio for gene was the maximum ratio amongst all its transcripts.

Stable isotope labeling by amino acids in cell culture (SILAC)

SILAC analysis was carried out as previously described⁵⁸. In short, cells were differentially labeled by growing them in control (L-WT ESC and KO EB) or heavy (H-KO ESC and WT EB) medium (heavy medium was labeled with both Lysine8 and Arginine10). Cell lysates were mixed at 1:1 ratio according to their protein concentration following protein quantitation (BCA kit, Thermo Scientific). Proteins were separated by SDS-PAGE and the gel excised in 40 equally sized segments. Each segment was digested with trypsin (Promega) and the resultant peptides analyzed by liquid chromatography coupled with tandem mass spectrometry (LC-MS/MS) using a Waters NanoAcquity HPLC system interfaced to a ThermoFisher Orbitrap Velos Pro. Data were processed

using MaxQuant searching against Swissprot Mouse and the ratio of heavy-to-light was calculated for each protein. SILAC sample processing and analyses were carried out by MS Bioworks, Ann Arbor, MI, (<http://www.msbioworks.com/>).

Global similarity matrices

Global similarity matrices indicate the similarity between the overall expression profiles of the different cells and conditions. The value in each matrix cell represents the overall similarity (Pearson correlation coefficient) between a pair of expression vectors. Expression vectors were obtained by counting the number of reads falling within each gene according to mm10 RefSeq annotation. For the RNA-seq data the count was based on all aligned reads, while for the Ribo-Seq data, we first removed duplicates (likely an amplification bias) before performing the count. For the SILAC data we used the vectors of the row intensity values of each reported gene. The Pearson correlation coefficients between all vector pairs were calculated by Matlab. The Heat map plots were also generated by Matlab.

Alternative Splicing Analysis

Alternative splicing events were detected from RNA-seq data with MATS software⁵⁹, using the software default parameters. Shortly, the software is looking for splicing events that are different between two given conditions, e.g. KO vs. WT. The events it detects are skipped-exon, retained-intron, mutually-exclusive-exons and alternative 3'-site or 5'-site. The inclusion rate (Fig. 39) reflects the percentage of fragments that included the exon (or intron), out of all fragments. Significance of overlap between alternative-splicing events and m6A peaks (Fig. 39) was calculated with Fischer's exact test.

RNA editing analysis

Identification of hyper-editing sites: We used the previously published pipeline for identifying A-to-I hyper-editing sites⁶⁰. Briefly, we aligned the RNA-seq to the mouse genome (mm10), using BWA and realigned the un-mapped reads to the transformed

genome. Only reads with 5 editing-sites were considered as hyper-edited reads. To calculate the hyper-editing index for specific RNA-seq sample, we calculated the ratio between the number of hyper-edited reads and # of mapped reads.

Editing levels of known A-to-I sites: Reads were mapped to the mouse genome using STAR aligner⁶¹ with default parameters. We used a list of published 9039 mouse sites (after filtering single genomic SNPs and not A-to-I sites)⁶². We calculated the editing levels of these sites using Reditools⁶³ using the following parameters: Minimal coverage-5, minimum quality score-20, minimum number of reads supporting a variation-1, minimal frequency-0.01. Editing levels were measured as the number of inosines divided by the number of inosines and adenosines.

Looking for differential editing levels: We compared editing levels in WT and KO EB and ES separately. Each site that had editing signal in at least one sample was taken into account (totally 1949 sites). Differential sites were defined with the following cutoffs-absolute difference of more than 0.1 editing levels, more than 1.5 fold, and a sufficient coverage (5 reads) in at least 3 out of 4 samples. Sites that have sufficient coverage in all 4 samples but have editing signal in both replicates of one group and none in the other group, were considered "exclusively edited".

Results

Generation of Mettl3 knockout naïve ESCs with m⁶A depleted mRNA

To study the role of m⁶A regulatory activity in pluripotency transitions and in early development, we sought to generate functional loss of this modification in mice and in mouse ESCs. Mammalian cells contain two m⁶A methyl-transferase proteins Mettl3 and Mettl14. Early studies show that Mettl3 or Mettl14 knockdown in HeLA and HEK-293 cells has shown up to 30-50% decrease in m⁶A levels^{24,34,36}. We decided to generate Mettl3 KO ESCs by standard homology recombination method (Fig. 1), and later on we also generated Mettl14 KO ESCs using the CRISPR/Cas9 genome editing technology (Fig. 13). Shortly, we introduced a conditional-KO and knock-in LacZ allele vector that targets the endogenous Mettl3 locus into V6.5 mouse naïve ESC. Correctly targeted Mettl3^{+/flox} cells were analyzed by PCR and southern-blot and treated with transient Cre expression to delete Exon4 of Mettl3 and generate a truncated out of frame product (Fig. 1b-d). Mettl3^{+/-} cells were injected to host blastocyst and chimeric animal were create (Fig. 1e). Those mice than backcross with C57BL/6 mice for 3 generation after germ-line transmission and create a colony of Mettl3 ^{+/-} mice. Mettl3 KO is embryonic lethal and we didn't find any Mettl3^{-/-} pups (Fig. 2a, more than 300 mice have been scanned). This result emphasizes the importance of the Enzyme for normal mammalian development. When we cross our Mettl3^{+/-} mice and take out E3.5 blastocysts we saw that those embryo retained normal morphology and expression of normal pluripotency markers like Nanog and Oct4 (Fig. 2b-d).

Expansion of these blastocysts in-vitro produced naïve Mettl3 KO ESCs at the expected Mendelian ratio in 2i/LIF conditions (Fig. 3a). All obtained Mettl3-null cell-lines were validated by PCR and by Western blot analysis for the depletion of Mettl3 protein (Fig. 3b-c). Naïve Mettl3 ESC in 2i/LIF conditions demonstrate a slightly reduced growth rate compare to WT probably because the stay longer in G1 phase (Fig. 3d-e), nevertheless they retain a normal karyotype (Fig. 3f) and their naïve pluripotent identity, despite the lack of m⁶A in mRNA (Fig. 4b), as evidenced by typical domed-shape colony morphology and expression of bona fide pluripotent markers including Nanog, Oct4, SSEA-1 and positive stain for Alkaline Phosphatase (AP) activity (Fig. 3g).

Figure 1

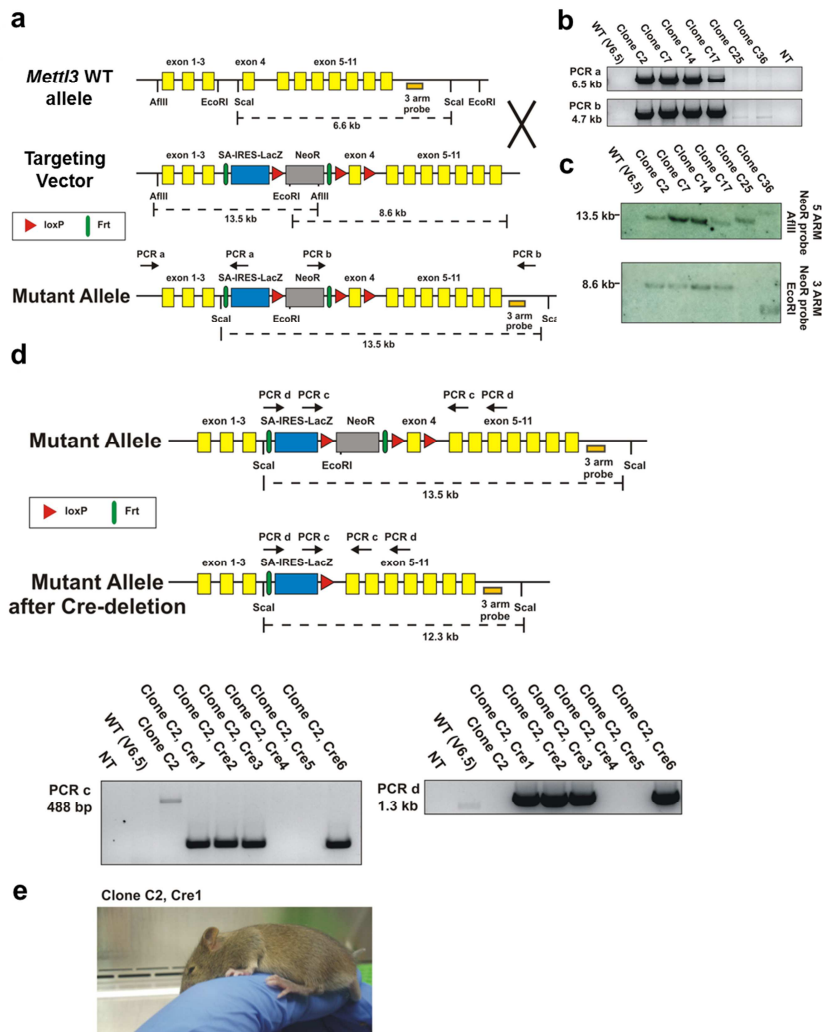


Figure 1: Gene targeting of murine *Mettl3* locus in embryonic stem cells. a) Targeting construct that includes LacZ reporter, neomycin resistance gene and floxed exon4, was inserted to the *Mettl3* locus by homologous recombination in naïve V6.5 ESC and created a mutant allele. The scheme shows and the restriction sites (EcoRI and AflII) and the relative location and direction of the PCR primers (a and b) used for validation of correct recombination event. Correct recombination was validated by PCR (b) and southern blot analysis (c). d) Subsequently we introduced Cre-recombinase enzyme, creating a KO allele that lacks *Mettl3* exon4. Deletion was validated by PCR (bottom panels) with two primer pairs (c and d) and by testing the cells for neomycin sensitivity. e) *Mettl3* mutant chimeric mice were generated by micro-injection of targeted V6.5 ESC into BDF2 blastocysts. Two identified male chimeric mice were crossed with C57B/6 female mice, and *Mettl3*^{+/-} germ-line transmitted mice were validated by color coating and LacZ transgene genotype

Figure 2

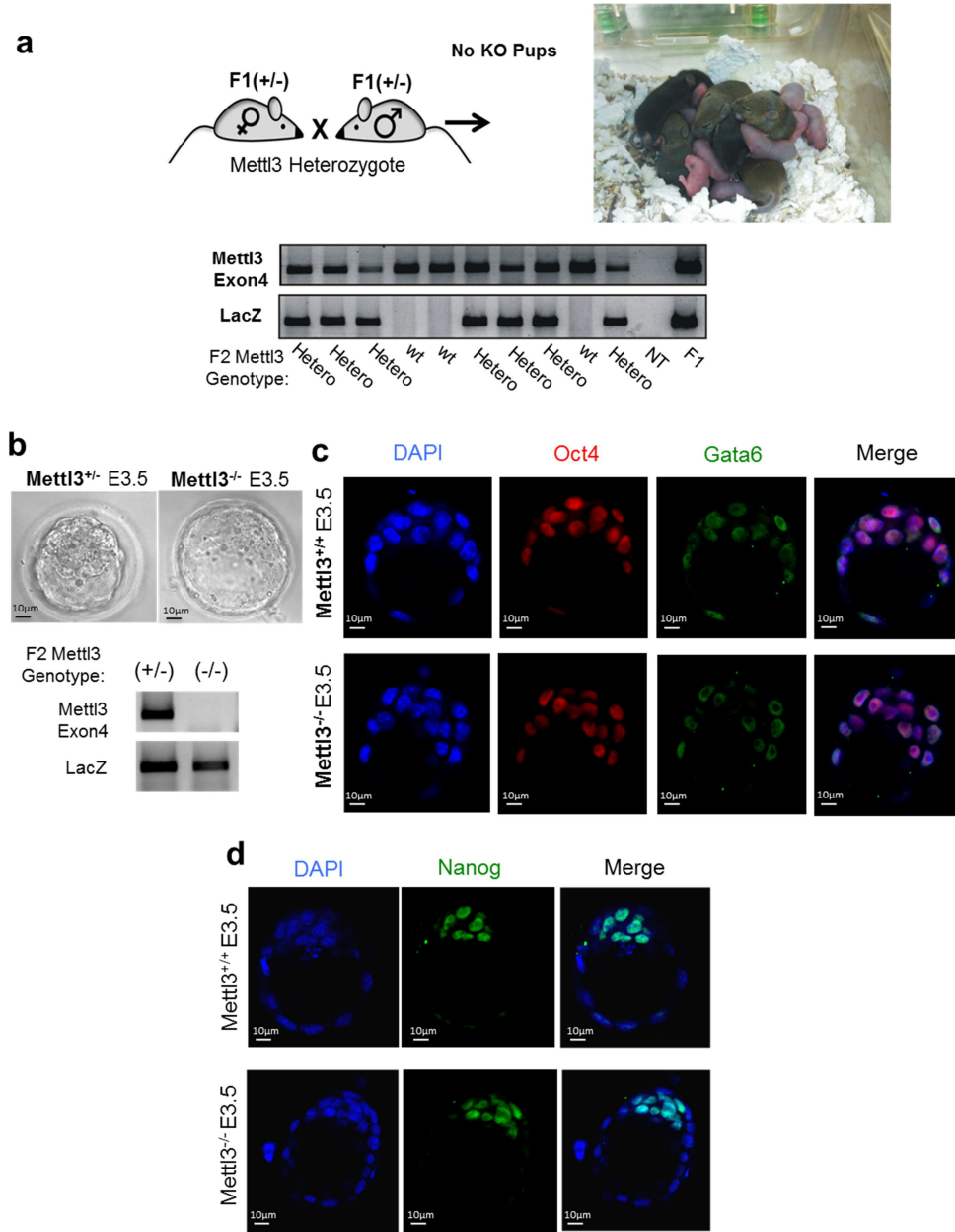


Figure 2: *Mettl3* KO is embryonic lethal, but shows normal pre-implantation blastocyst development. a) *Mettl3*^{+/-} mice were crossed and pups were genotyped for *Mettl3* Exon4 and for the LacZ cassette. PCR genotyping examples of 2 litters are shown. No living embryos carrying double *Mettl3* exon4 deletion were born (n=202 total pups analyzed). b) *Mettl3*^{+/-} and *Mettl3*^{-/-} E3.5 blastocysts showing a normal morphology. Bottom – *Mettl3* genotyping strategy showing the genomic lack of *Mettl3* Exon-4, and the presence of LacZ cassette in KO embryos. c) Immunostaining of WT and *Mettl3* KO E3.5 blastocysts, for DAPI (blue), Oct4 (red) and Gata6 (green). d) Immunostaining of WT and KO E3.5 blastocysts for DAPI (blue) and Nanog (green).

Figure 3

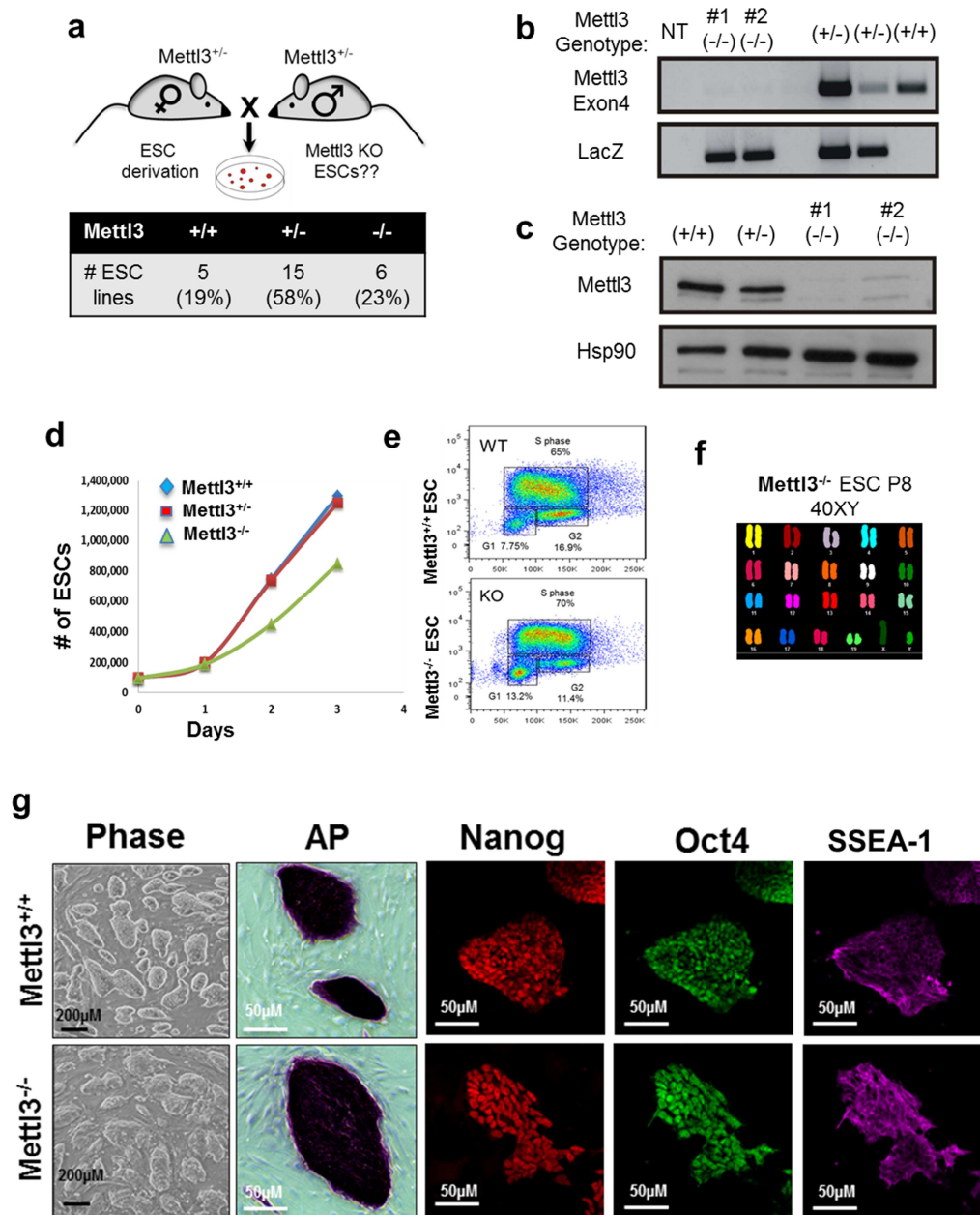


Figure 3: Derivation and characterization of Mettl3 KO ESCs. **a)** ESC derivation efficiency following mating of Mettl3 heterozygote mice. Total of 26 ESC lines were derived. **b)** The KO ESC were validated by PCR as LacZ positive and *Mettl3* exon4 negative. **c)** Mettl3 KO ESC clones were validated by Western-blot analysis for complete depletion of Mettl3 protein. **d)** Growth rate curves of WT and KO ESCs. **e)** Cell cycle profile of WT and KO ESCs. Cells were treated with BrdU and stained with PI. **f)** Karyotype of KO ESC clone at passage 8. **g)** Representative colony morphology and immunostaining images for pluripotent markers: Nanog, Oct4, SSEA1 and AP staining.

Purified mRNA from Wild-type, Mettl3^{+/-} and Mettl3 KO cells were subjected to liquid chromatography-tandem mass-spectrometry for accurate quantification of m⁶A levels²⁵. Importantly, to avoid contamination with rRNA that are methylated by Mettl3 independent pathways⁶⁴, mRNA was purified following 2 rounds of Oligo dT-selection followed by two rounds of rRNA removal, and only then we determined m⁶A levels by LC-MS/MS. Remarkably, m⁶A modification was nearly undetectable in the mRNA fraction of Mettl3 KO ESCs and embryoid bodies (EB) (Fig. 4 a-c), suggesting that deletion of the Mettl3 is sufficient for near complete depletion of m⁶A from mRNA. This argues against a compensatory activity of Mettl14 or WTAP containing complexes in the absence of Mettl3^{34,65}. It is impotent to mention that Mettl3^{+/-} cells do not show significant reduction of m⁶A level even though the reduction of 50% in Mettl3 RNA and protein levels (Fig. 4a, 3c). These results highlight the fact that Mettl3 Enzyme can function even in below normal expression level without reduction in m⁶A levels and only strong reduction in it expression can effect m⁶A RNA modification levels.

The derivation of Mettl3 KO ESCs is particularly exciting since METTL3 knockdown in a variety of mammalian cells leads to massive apoptosis and cell cycle arrest^{24,66}, which has hampered and complicated studying m⁶A functional biology in mammalian cells. This cells allow us in the first time to test the function of m⁶A modification on mRNA biology in viable cell-line during pluripotent state and differentiation.

Figure 4

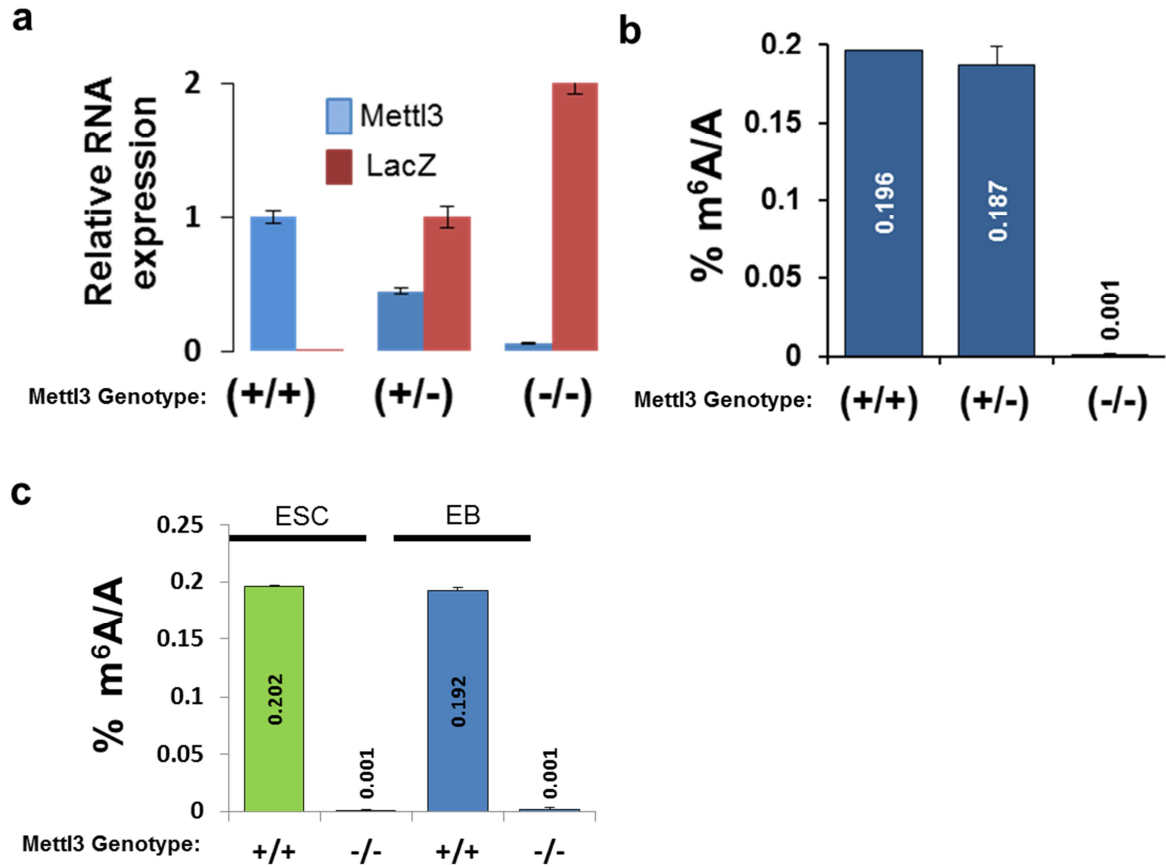


Figure 4: characterization of mRNA m⁶A modification in Mettl3 KO ESCs.

a) qPCR analysis of the relative expression of Mettl3 exon4-exon5 junction and LacZ expression, validating the genotyping results. b) m⁶A fraction relative to adenosine fraction in purified mRNA from WT, heterozygote and KO ESC quantified by LC-MS/MS. The m⁶A ratio does not decrease in the Mettl3 heterozygote cells despite the 50% decrease in mRNA levels. Error bars indicate s.d. (n=2). c) Mass-spectrometry analysis of m⁶A fraction relative to adenosine fraction in purified mRNA from Mettl3 WT and KO ESC and EB. Error bars indicate s.d. (n=2).

Mettl3 KO ESCs resist terminating the naïve ground state of pluripotency

***In vitro*-differentiation, embryoid bodies**

After characterizing the cells in the pluripotent state we next wanted to test the ability of Mettl3^{-/-} ESC to differentiate *in-vitro* by using embryoid bodies (EB) assay. Wild-type (WT) and Mettl3 KO cells were transferred to non-adherent plate with serum-based media without the self-renewal cytokine LIF for 8-21 days, in this condition ESC undergo spontaneous germ layer cell differentiation (Fig. 5a). KO cells generated dense EB spheres but failed to undergo the characteristic cavitation observed in WT EB (Fig. 5b). In addition, analysis of differentiation markers by qPCR and western-blot shows that KO EB failed to robustly up regulate early development markers such as Gata6, Foxa2, Fgf5 and Dnmt3a/b and to adequately repress pluripotent genes such as Nanog, Rex1 and Klf4 after 8 days of differentiation (Fig. 5c-d). The fact that our KO cells do not shut-down the pluripotent gene led us to suspect that they “trapped” in the pluripotent state. To test this hypothesis 21 days old EB were disaggregated and re-plated on feeder cells in ESC naïve condition. KO but not WT cells, efficiently generated ESC colonies and stable ESC lines that were positive for AP, Nanog and Oct4 expression (Fig. 6a-b).

When we tried to apply directed *in vitro* neuronal differentiation protocol by retinoic-acid induction, our KO cells failed to differentiate into mature neurons. The KO samples showed residual number of Nestin⁺, neuronal progenitor, cells and near absence of Tuj1⁺ mature neurons. During the differentiation we observe massive cell death in the KO plate (Fig. 6c).

Figure 5

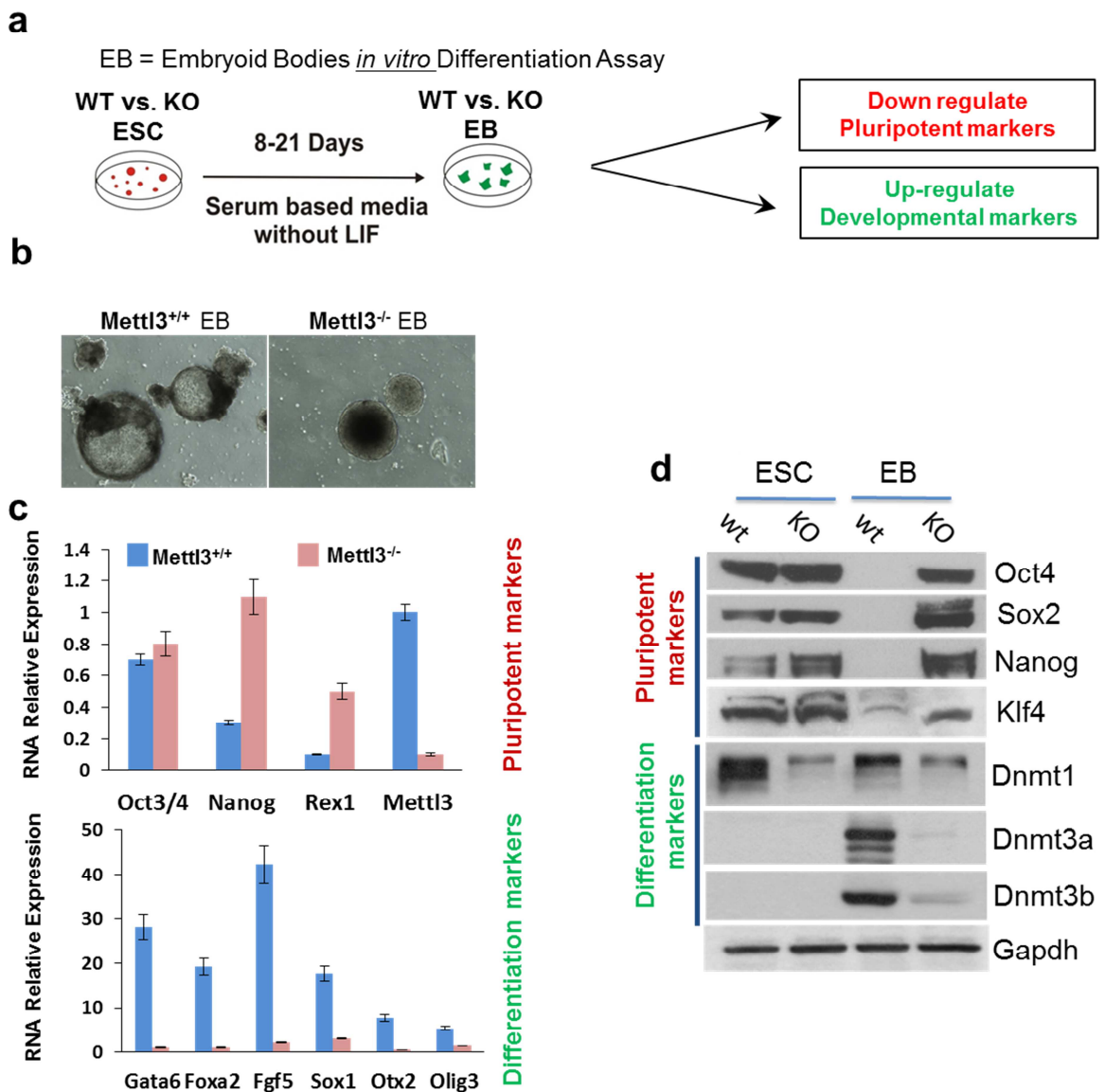


Figure 5: Mettl3 KO ESCs resist termination of naïve pluripotency program *in vitro*. **a)** A schematic illustration of the EB differentiation experiment. WT and KO ESC were transferred to serum-based media without LIF on non-adherent plates, to promote cell differentiation **b)** Phase images showing EB differentiation from WT and KO naïve ESCs after 21 days. WT EBs undergo maturation and cavitation, while KO EBs remain densely packed. **c)** qPCR analysis for differentiation (lower panel) and pluripotency gene expression (upper panel) after 8 days of EB differentiation. Error bars indicate s.d. (n=3). **d)** Mettl3 WT and KO ESC and 11 day EB were subjected to Western-blot analysis to compare the levels of Oct4, Sox2, Nanog, Klf4, Dnmt1 and Dnmt3a and b. Gapdh was used as loading control. Mettl3 KO EB failed to down-regulate the tested naïve ESC markers Oct4, Sox2, Nanog and Klf4, as well as to up-regulate differentiation markers (Dnmt1/3a and 3b)

Figure 6

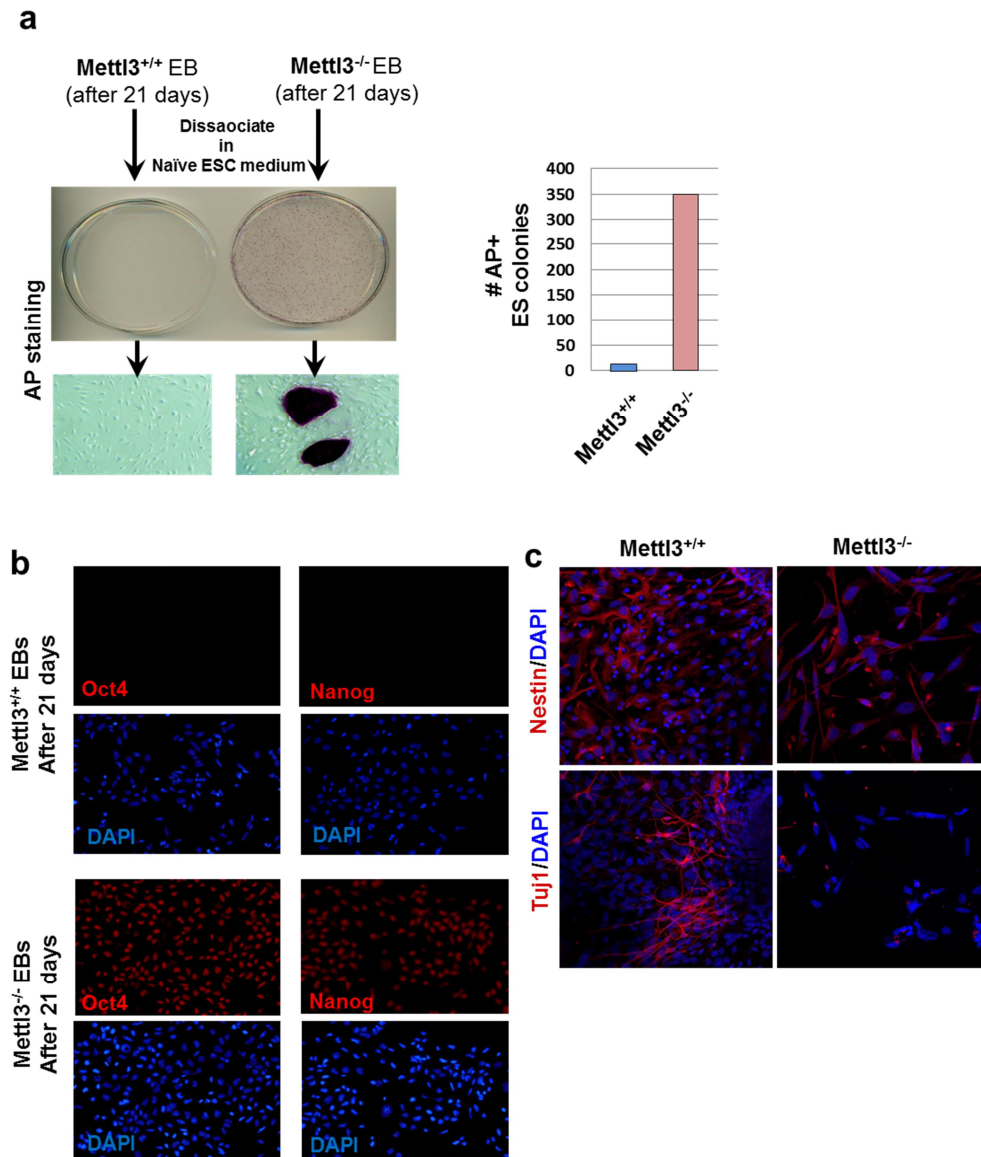


Figure 6: Mettl3 KO ESCs resist termination of naïve pluripotency program *in vitro*

a) WT and KO ESC were transferred to serum-based media without LIF for 21 days, to promote cell differentiation. The cells were then disaggregated, re-plated on feeder cells and grown in ESC conditions for 7 days. Mettl3 KO, but not WT cells generated ESC colonies positive for AP enzymatic activity. **b)** Cells were immunostained for Nanog and Oct4 expression and imaged by fluorescent microscopy. KO cells maintain Oct4 and Nanog expression even after 21 days of *in vitro* EB differentiation. **c)** WT and Mettl3 KO ESC were subjected to retinoic acid neuronal differentiation assay for 20 days. Mettl3 WT cells started to adopt neuronal shape and expressed the early neuronal marker Nestin and mature neuronal marker Tuj1. Mettl3 KO cells underwent massive cell death and showed severely poor differentiation ability.

***In vitro/vivo*-differentiation, teratoma formation**

To test the ability of *Mettl3*^{-/-} cells to differentiate in a more stringent developmental assay, WT and KO cells were introduced with Oct4-GFP pluripotency reporter and injected into immunodeficient mice in order to generate mature teratomas (Fig. 7a). After 6 weeks we surgically removed the tumors and analyzed them by FACS and by histological section staining. While *Mettl3*^{-/-} ESC generated very large tumors (Fig. 7b), the histological section analysis showed that KO teratomas were poorly differentiated and did not exhibit characteristic germ layer structures, while mature structures were abundant in WT ESC derived teratomas (Figure 7c). Immunostaining for specific differentiation markers showed that KO teratomas poorly expressed differentiation markers such as Gata4, Gata6 and Troponin, and diffusely expressed pluripotent markers such as Oct4, Esrrb and Nanog even after 6 weeks following subcutaneous *in vivo* injection (Fig. 7d-f). Single cell disaggregation of KO dissected tumors followed by FACS analysis, demonstrated that >75% their cells still expressed the Oct4-GFP reporter (Fig. 8b). Dramatically, the KO, but not WT, teratomas contained pluripotent cells that could rapidly recover in culture and give rise to ESC colonies within 6 days, and formed stable ES lines that retain Oct4-GFP expression and other pluripotency markers (Fig. 8c). In addition FACS analysis of dissociated teratoma cells were stained with anti-Thy1 (somatic marker) and anti-SSEA-1 (an embryonic stem cell marker). This analysis revealed that *Mettl3* KO cells express high levels of SSEA-1 and low levels of Thy1 relative to WT after 42 days of *in vivo* differentiation (Fig. 8d).

Figure 7

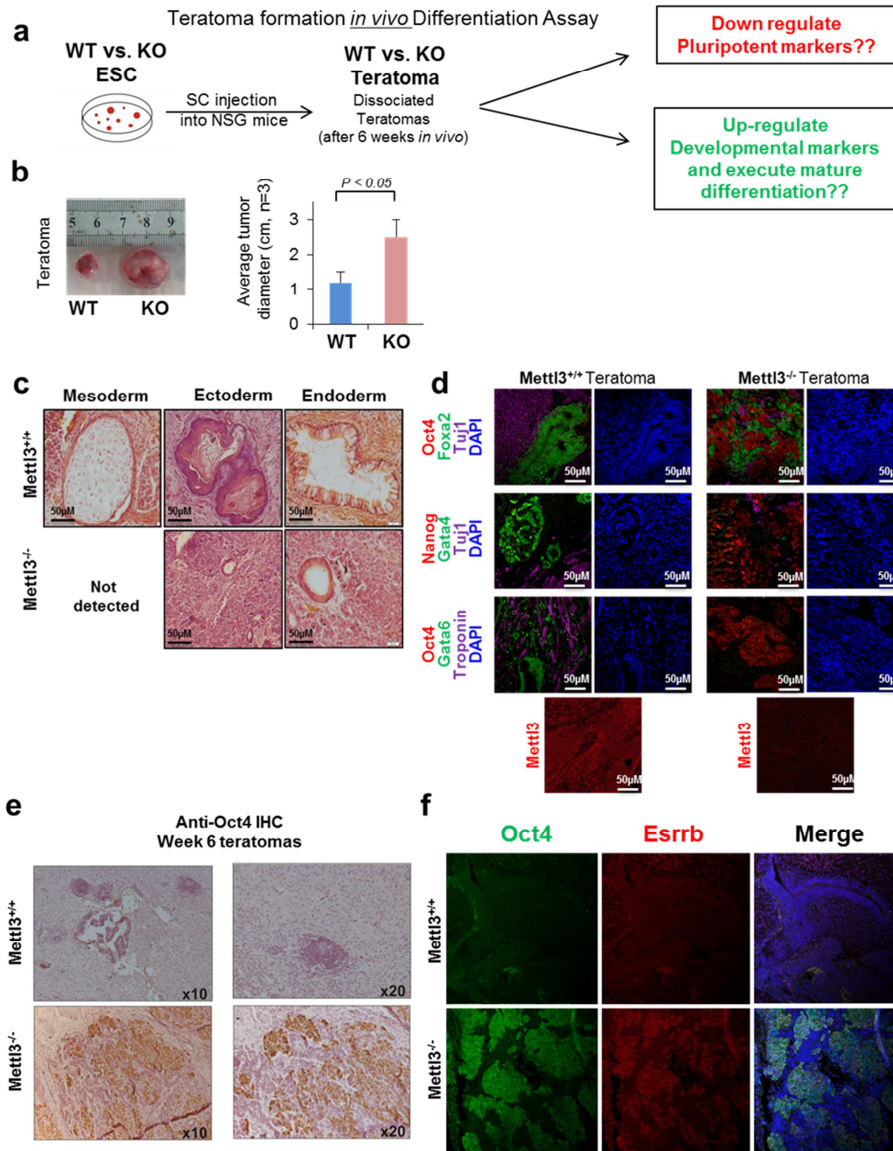


Figure 7: Mettl3 KO ESC show severely impaired *in vivo* differentiation into mature teratomas. **a)** A schematic illustration of the Teratoma differentiation experiment. 5×10^6 WT or KO ESCs (with or without Oct4-GFP pluripotency reporter) were injected subcutaneously to NSG immune-deficient mice, and teratomas were collected after 42 days. **b)** KO teratomas were significantly bigger (WT=1.2±0.3cm, KO=2.5±0.3cm). **c)** Paraffin sections and H&E staining reveal characteristic three germ layers structure (gut-like epithelia - endoderm, cartilage - mesoderm and keratin pearls - ectoderm) in WT, but not in KO teratomas. Only immature neuroectoderm and endodermal pseudo-structures were detected. **d-f)** Representative immunostaining of teratoma sections for differentiation markers (Foxa2, Tuj1, Gata4, Gata6 and Troponin) and pluripotent markers (Oct4, Nanog and Esrrb). Mettl3 KO teratomas do not up-regulate differentiation genes and do not turn off the expression of pluripotent genes.

Figure 8

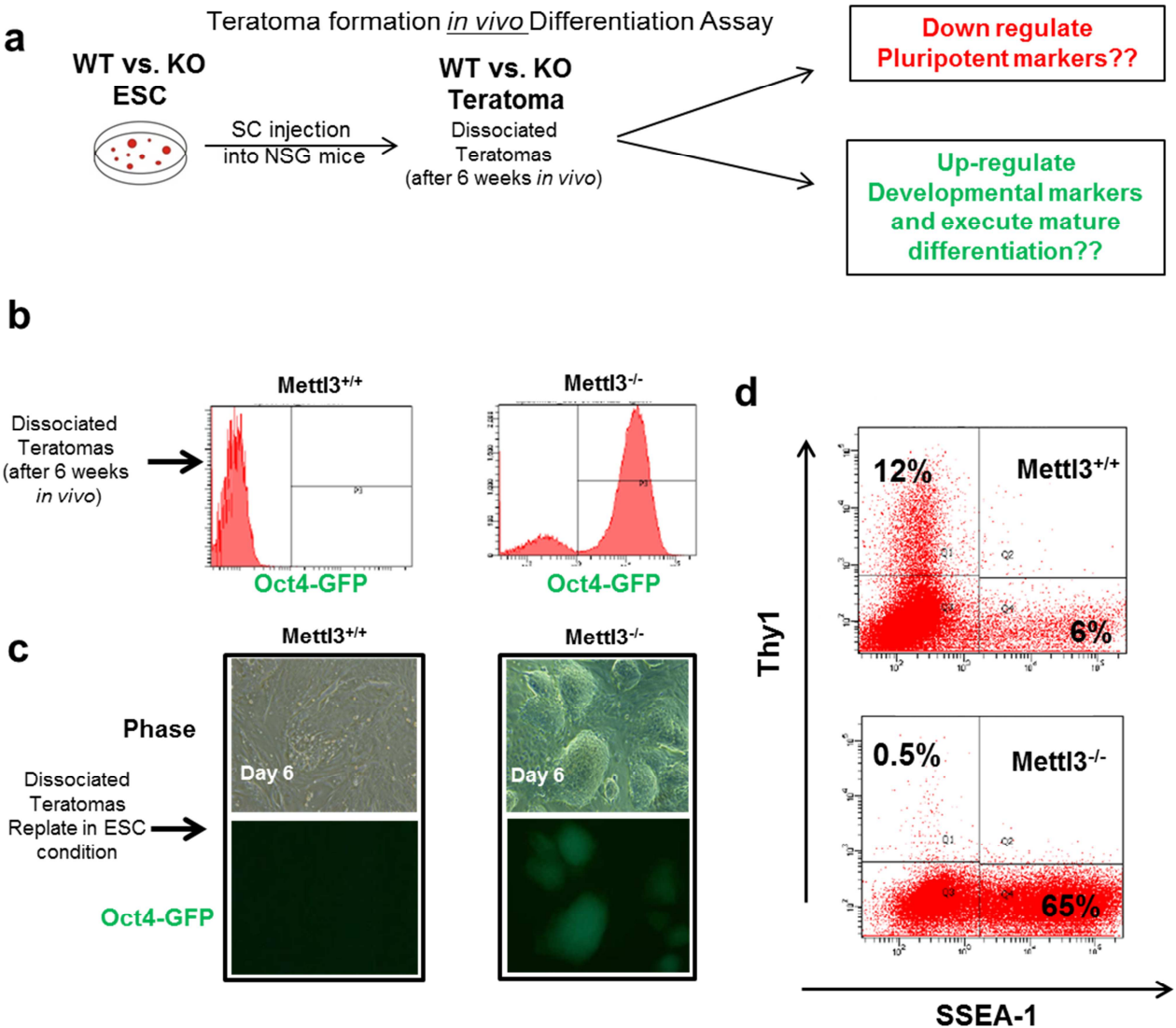


Figure 8: Mettl3 KO ESC show severely impaired *in vivo* differentiation into mature teratomas. **a)** Schematic illustration of the experimental design. **b)** Teratomas generated from WT and Mettl3 KO expressing GFP under the control of Oct4 promoter (Oct4-GFP) were generated as described in Methods. The teratomas were disaggregated and GFP levels were analyzed by FACS. KO, but not WT teratomas show a very high amount of Oct4-GFP+ cells **c)** Mettl3 WT or KO teratomas were disaggregated and plated for 6 days on MEF cover plates with ESC-supporting media. KO, but not WT cells recreated ESC colony morphology, expressed Oct4-GFP and generated stable ES lines. **d)** FACS analysis of dissociated teratoma cells were stained with anti-Thy1 somatic marker and anti-SSEA-1, an embryonic stem cell marker. This analysis revealed that Mettl3 KO cells express high levels of SSEA-1 and low level of Thy1 relative to WT after 42 days of *in vivo* differentiation.

***In vitro* -differentiation, EpiSC conversion**

We next wanted to test the ability of *Mettl3*^{-/-} ESC to convert from naïve pluripotent state into primed epiblast-like state. This can be done *in-vitro*, by changing the medium from naïve-supporting N2B27 2i/LIF to primed-supporting FGF2/Activin media^{67,68}. By 2 passages in primed pluripotency growth conditions, WT colonies showed a typical flat morphology rather than the characteristic domed morphology of naïve cells (Fig. 9a). In addition, WT cells down-regulated expression of naïve markers such as *Nanog*, *Rex1* and *Klf4* and up-regulated primed markers such as *Xist*, *Foxa2* and *Fgf5* (Fig. 9b). *Mettl3*^{-/-} colonies, on the other hand, kept their naïve-domed shape, failed to down-regulate naïve markers, and up-regulated only *Fgf5* but not *Xist* or *Foxa2* (Fig. 9b). We observed a similar trend after extended passaging also by immunostaining and by Western blot analyses (*Esrrb*, *Klf2* and *Nanog*= Naïve markers. *Foxa2* and *Brachyury*=Primed markers, Fig. 9c-e 10a). Enriched cytoplasmic localization of *Tfe3* upon pluripotency priming was observed only in KO cells (Fig 10b), consistent with a general deficiency in exiting naïve and entering the primed pluripotent state. One of the major changes that occur in epigenome in the conversion between naïve to primed pluripotent state is the inactivation of one of the X chromosome in female cells. *Mettl3* KO female cells (XX) do not up regulate the *Xist* lincRNA (Fig 9b) that involve in the X inactivation process and do not marked with the repressive histone marker H3K27me3 (Fig 10c) that coated one of the X chromosome in WT female cells.

***In vivo* -differentiation, Blastocyst complementation**

In order to complete the characterization of the differentiation impairing of the *Mettl3* KO cells we perform blastocyst complementation and test the ability of the cells to contribute to chimera embryo formation. WT and KO cells were introduced with mCherry constitutive tg reporter and injected to BDF1 host blastocyst (Fig 11a). After 10 days embryos have been taken out for the analysis of chimera formation. Not surprisingly only WT cells can contribute to chimera formation as can indicated by embryo Whole-mount mCherry imaging and by FACS analysis (Fig 11b-c).

Overall, *Mettl3*^{-/-} cells maintain normal and predicted characteristics of embryonic stem cells *in-vitro*, but show a "hyper-pluripotent" phenotype; where naïve *Mettl3*^{-/-} cells are highly resistant to terminate their already established naïve pluripotency program in response to a variety of stringent differentiation induction protocols, and subsequently fail to upregulate key developmental markers. To the best of our knowledge, this is one of the most dramatic resistances to exit pluripotency phenotypes observed thus far.

Rescue of differentiation competence of KO cells by exogenous *Mettl3* transgene

In order to validate that our phenotype is *Mettl3* specific we decided to perform a rescue experiment. We cloned the mouse *Mettl3* coding sequence from ESC RNA extract and cloned it into constitutive pBRY-CAG plasmid. The recovery plasmid encoding a mouse *Mettl3* transgenic allele (tg) and IRES-PURO selection cassette (Fig 12a). *Mettl3* KO cells were introduced with the plasmid and after 10 days of selection with puromycin we validate the rescue of *Mettl3* protein by WB analysis (Fig 12a). For analyzing the rescue phenotype we repeated our *in vitro* differentiation experiment and test the ability of the rescue cells to differentiate to EBs and to teratoma. qPCR analysis for differentiation and pluripotency gene expression after 8 days of EB induction show that the *Mettl3* tg restore the WT differentiation phenotype (Fig 12b). In the teratoma assay, our rescue line were able to differentiate as validated by histological H&E staining that reveal characteristic three germ layers structure (gut-like epithelia - endoderm, cartilage - mesoderm and neurons - ectoderm) (Fig 12c). In other assay Teratomas generated from WT, *Mettl3* KO and *Mettl3*-tg rescued KO ESCs, expressing Oct4-GFP specific reporter, were used. The teratomas were disaggregated and Oct4-GFP levels were analyzed by FACS. KO, but not WT or *Mettl3*-tg rescued teratomas show a very high amount of Oct4-GFP⁺ cells (Fig 12c), despite being 6 weeks *in vivo* without supplementation of exogenous pluripotency promoting conditions.

Figure 9

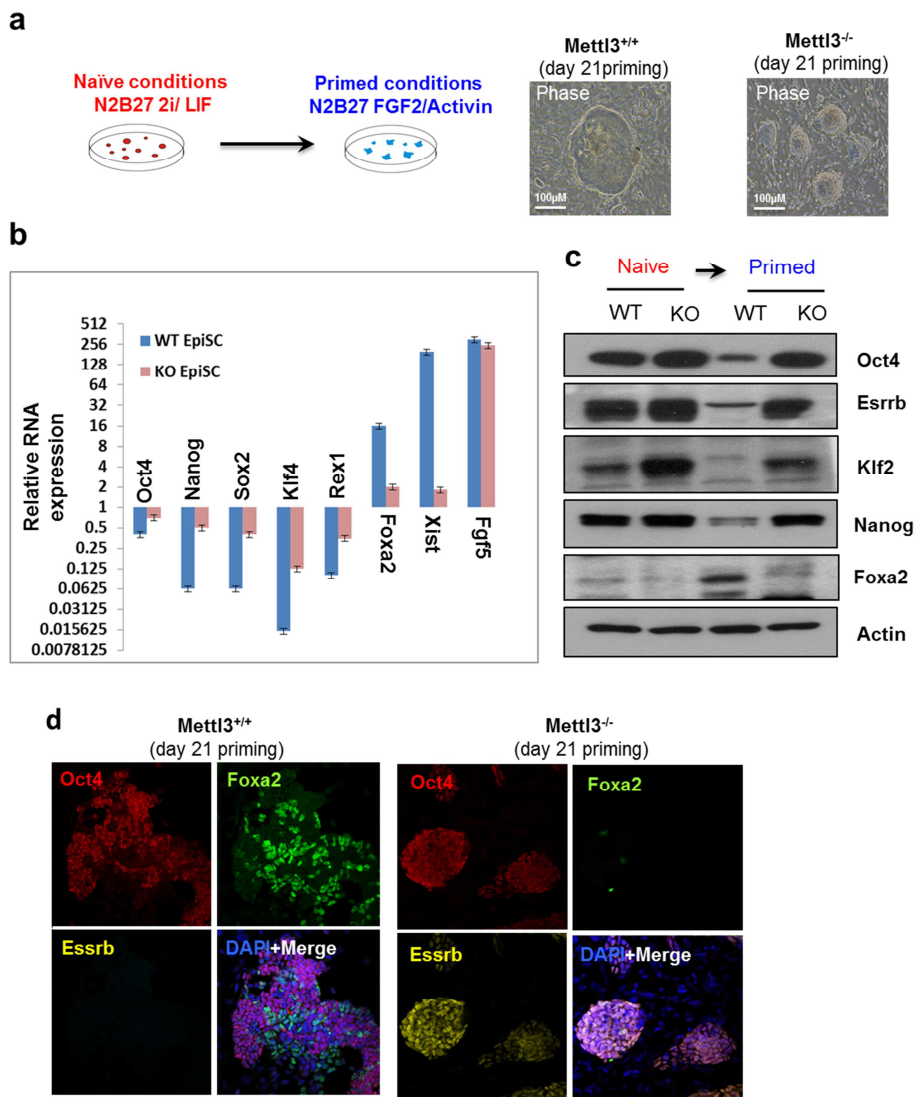


Figure 9: Mettl3 KO ESC resist *in-vitro* conversion into primed epiblast-like cells.

a) Schematic illustration of the experimental design. Mettl3 WT and KO cells that were transferred from N2B27 2i/LIF naïve conditions to N2B27 FGF2/Activin primed conditions for 21 days. Typical Morphological images of the cells after the conversion. **b)** qPCR analysis re-indicated that Mettl3 KO ESC exhibit reduced down-regulation of pluripotency markers (Oct4, Nanog, Sox2, Klf4 and Rex1) as well as reduced induction of primed markers (Foxa2 and Xist). Notably Fgf5 is upregulated Mettl3 KO cells upon priming, indicating that the cells undergo partial upregulation of some primed genes. qPCR and WB analysis of converted cells. **c)** Western blot analysis of WT and Mettl3 KO naïve and primed ESC lysates revealed that Mettl3 KO cells fail to down-regulate the naïve markers; Oct4, Esrrb, Klf2 and Nanog and fail to induce expression of Foxa2. Actin was used as a loading control. **d)** Immunostaining for the pluripotent markers; Oct4 (red), and Esrrb (yellow), and for the differentiation marker Foxa2 (green) are shown. KO cells fail to express Foxa2 and to down-regulate Esrrb.

Figure 10

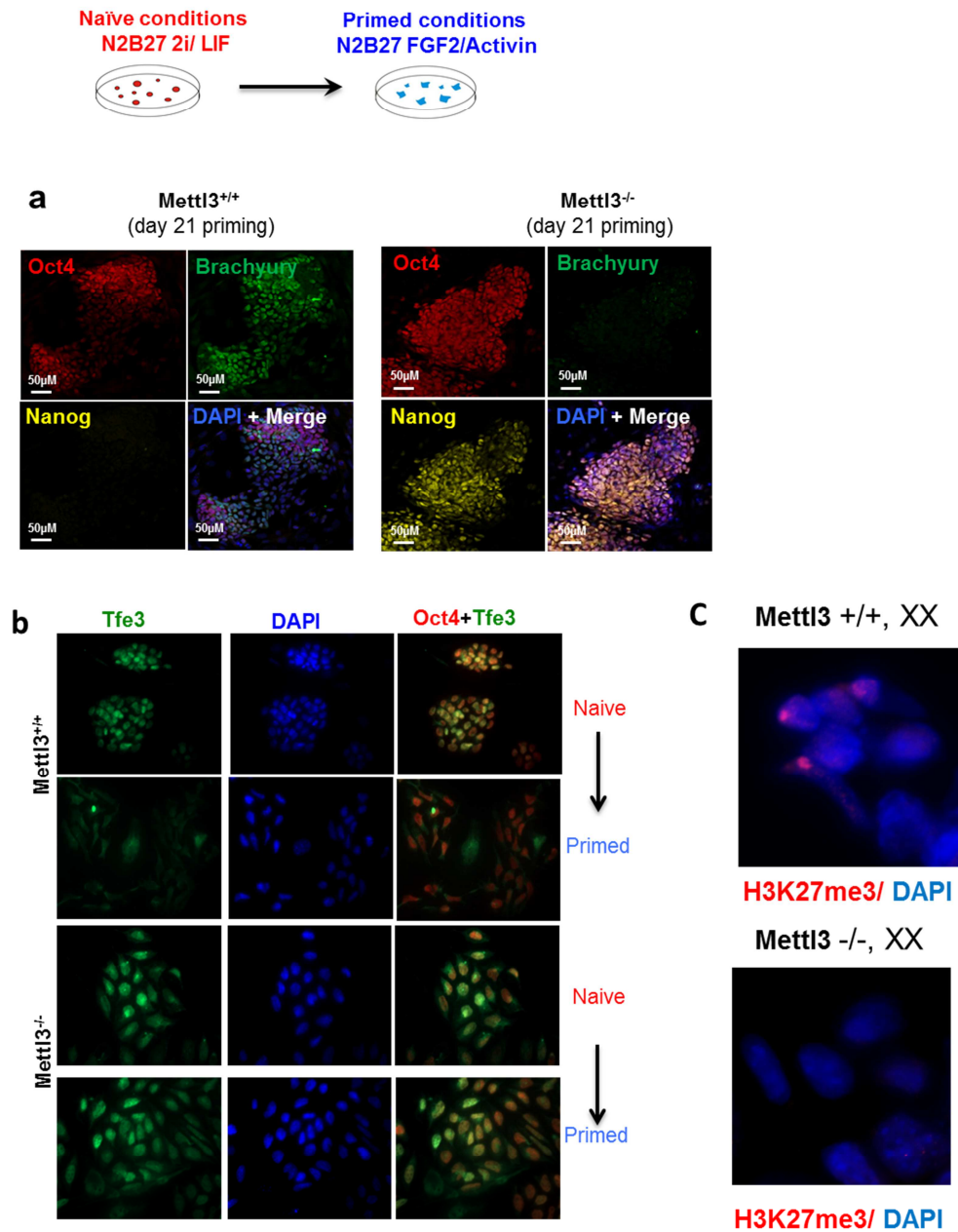


Figure 10: Mettl3 KO ESC resist *in-vitro* conversion into primed epiblast-like cells.
a) Immunostaining for the pluripotent markers; Oct4 (red), and Nanog (yellow), and for the differentiation marker Brachyury (green) are shown. KO cells fail to express Brachyury and to down-regulate Nanog. b) Immunostaining for Oct4 (red) and the Tfe3 (green) marker that is exported from the nucleus to the cytoplasm in primed cells, demonstrate that KO cells retain the Tfe3 predominant nuclear localization in primed conditions. c) Immunostaining for K27met3 (red) shows strong nuclear foci that indicated for X inactivation.

Figure 11

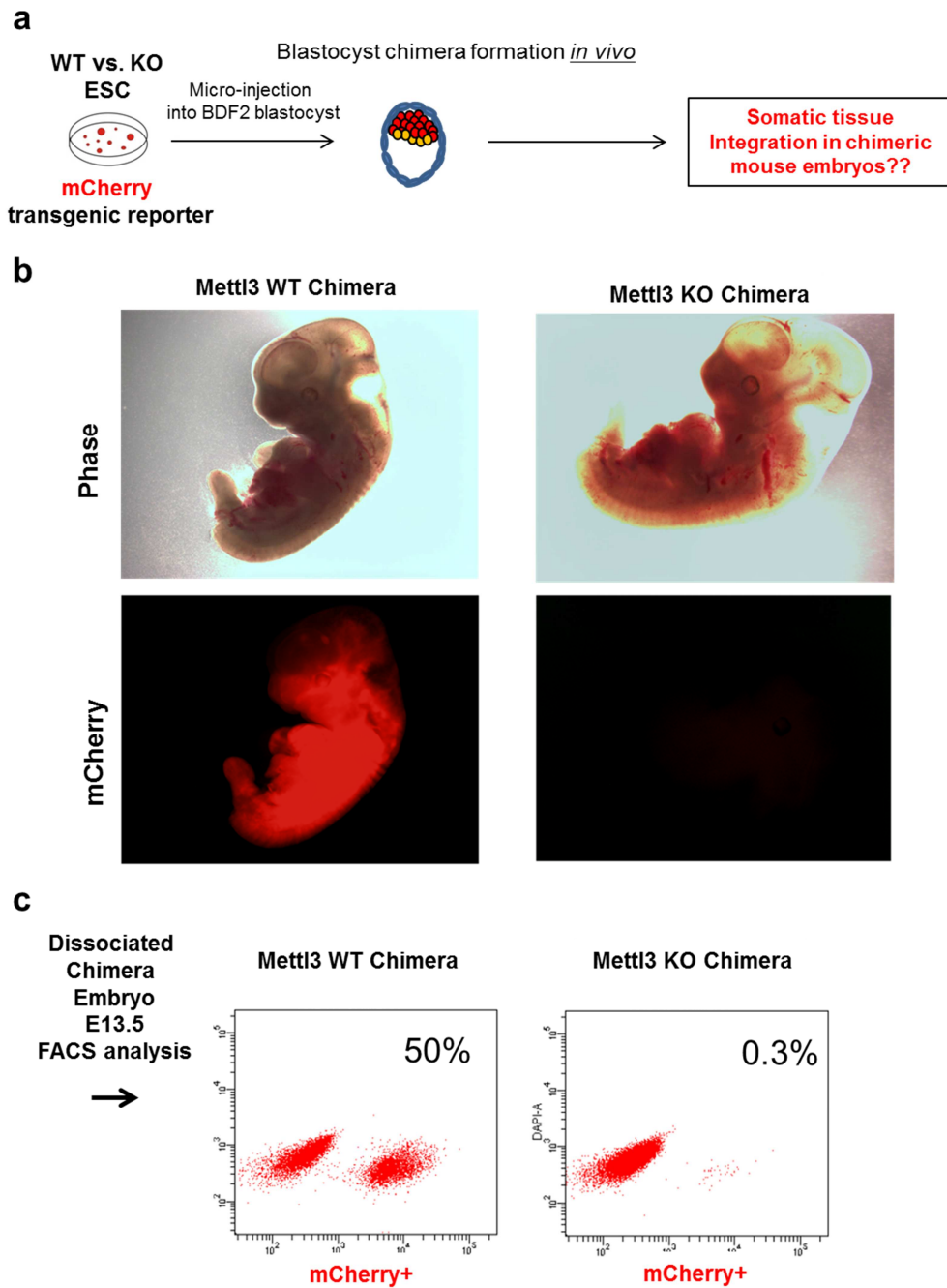


Figure 11: Naïve Mettl3 KO ESCs show impaired ability to contribute to chimeric embryos. **a)** Schematic illustration of the experimental design for microinjecting WT and Mettl3 KO naïve ESCs, constitutively labeled with a constitutive mCherry reporter. **b)** Representative phase images showing lack of contribution with Mettl3 KO ESCs in E12.5 BDF2 host embryos (total of n=12, E12.5 embryos were analyzed). **c)** FACS analysis of chimeric embryos shows little contribution of Mettl3-KO cells to host embryo.

Figure 12

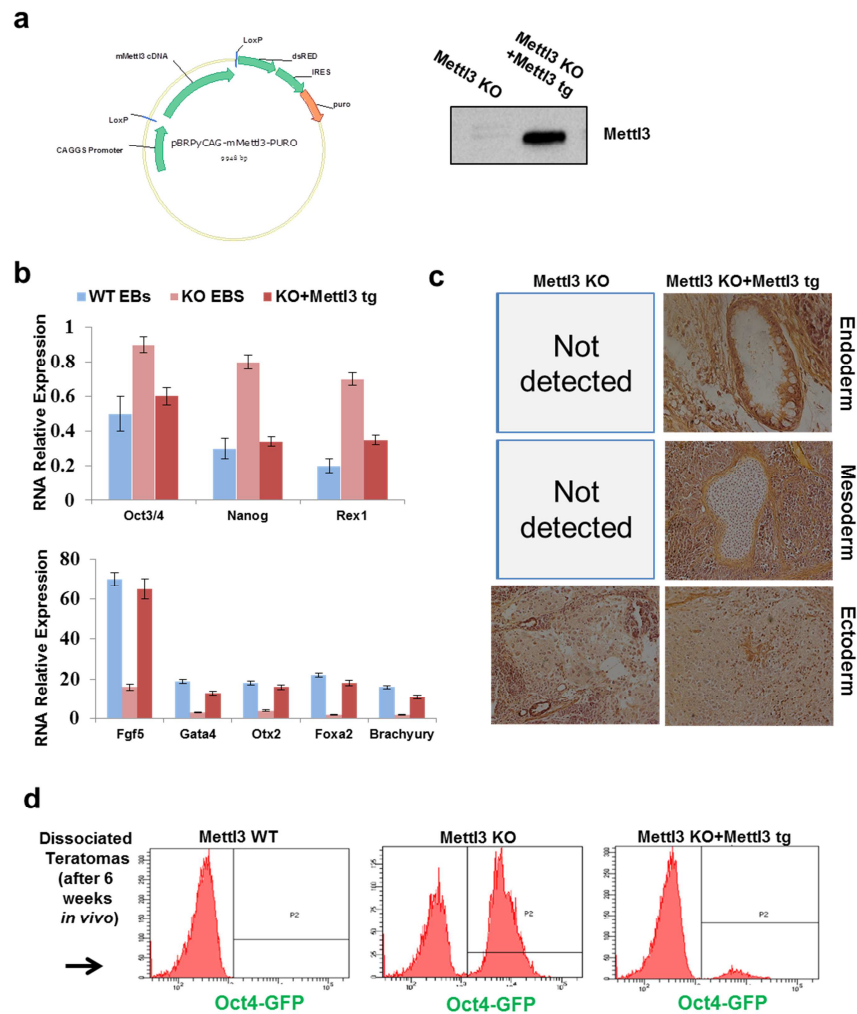


Figure 12: Rescue of differentiation competence of KO cells by exogenous Mettl3 transgene. **a**) Schematic representation of pBRY-CAG plasmid encoding a constitutive mouse Mettl3 wild type (WT) transgenic allele (tg), and IRES-PURO selection cassette. Western blot validating rescue of Mettl3 expression by the transgene in Mettl3 KO ESCs (rescued cell line = Mettl3 KO + Mettl3 tg. **c**) qPCR analysis for differentiation (lower panel) and pluripotency gene expression (upper panel) after 8 days of EB induction. Error bars indicate s.d. (n=3). **c**) Paraffin sections and H&E staining reveal characteristic three germ layers structure (gut-like epithelia - endoderm, cartilage - mesoderm and neurons - ectoderm) in Mettl3-tg rescued KO teratomas, but not in KO teratomas. Only immature neuroectoderm pseudo-structures were detected in KO teratomas. **d**) Teratomas generated from WT, Mettl3 KO and Mettl3-tg rescued KO ESCs, expressing Oct4-GFP specific reporter, were used. The teratomas were disaggregated and Oct4-GFP levels were analyzed by FACS. KO, but not WT or Mettl3-tg rescued teratomas show a very high amount of Oct4-GFP+ cells, despite being 6 weeks *in vivo* without supplementation of exogenous pluripotency promoting conditions.

Mettl14 KO ESC lose m⁶A RNA modification and phenocopy the Mettl3 KO phenotype

Different reports^{34,36} had previously shown that Mettl14, a mammalian homolog of Mettl3, possesses also m⁶A RNA methyltransferase activity. In order to assess the activity of Mettl14 in ESC we knocked-out Mettl14 using the CRISPR/Cas9 technology (Fig. 13a). Clones that contain deletion in the Mettl14 locus scan by high resolution melting curve analysis (HRM), and positive clones were sequence and analysis by WB for Mettl14 depletion (Fig. 13a,b). To our surprise, Mettl14 KO ESC showed identical phenotype as Mettl3 KO ESC. Mettl14KO showed equivalent reduction in m⁶A in mRNA (Fig. 13c) and equivalent reduction in cell proliferation (Fig. 13d). Mettl14KO ESC maintained their naïve pluripotent markers and morphology (Fig. 13e) and showed the same *in vitro* resistance to differentiation in EB assay as was seen with Mettl3 KO ESCs (Fig. 13f). WB analysis of different component of the m⁶A methyltransferase complex showed that the depletion of Mettl3 or Mettl14 results in destabilization of the other. The results suggested that this protein may indeed work as METTL3/METTL14 complex, and the depletion of each one of them hampers the stability of the other partner and abolishes the m⁶A methyltransferase activity in the mammalian cell. This result was recently supported by an independent follow-up study³⁶.

The fact that Mettl14 KO recapitulated the *in vitro* resistance to differentiation as seen with Mettl3 KO ESCs shows that the phenotype occurs due to the loss in global m⁶A modification that has important regulatory effects in mammalian cells.

Figure 13

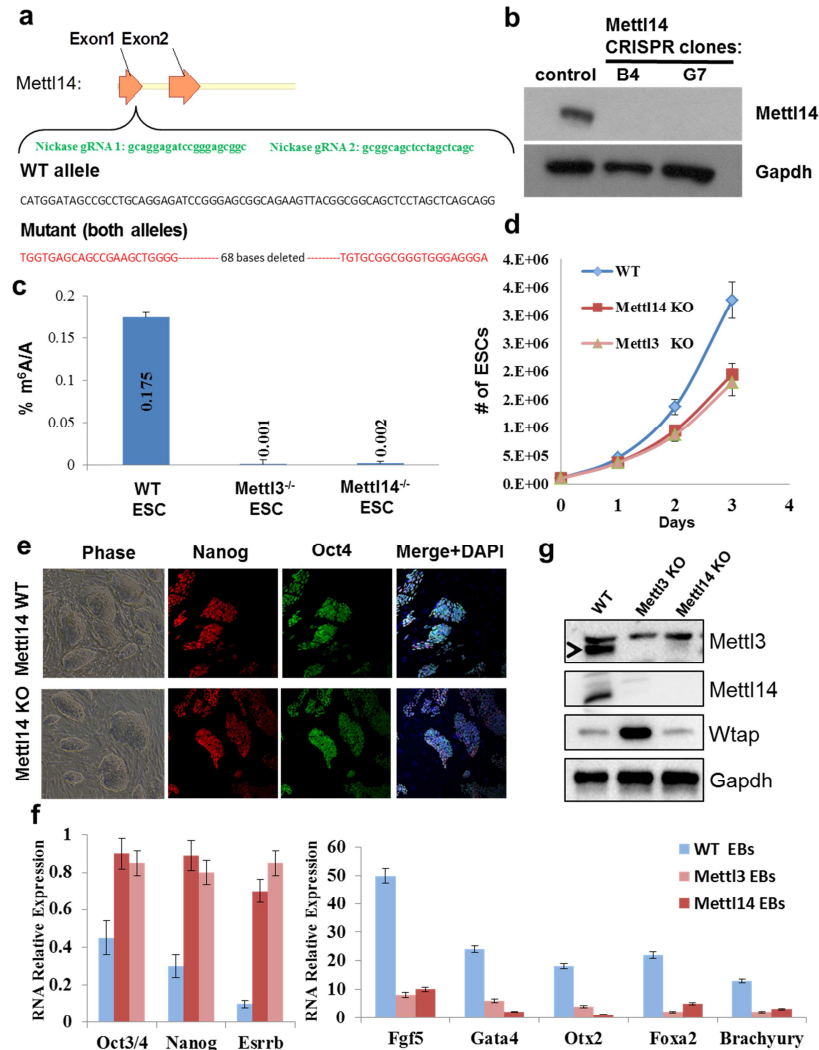


Figure 13: Mettl14 KO ESCs recapitulate m⁶A depletion and differentiation block seen in Mettl3 KO ESCs. **a**) Schematic representation showing sgRNA sequences used to target Exon1 of Mettl14 mouse locus. Locus sequence after deletion in clone G7 that was used for further analysis is shown. **b**) Western blot confirming ablation of Mettl14 in two correctly targeted clones (B4 and G7). **c**) LC-MS/MS analysis of m6A fraction relative to adenosine in purified mRNA. Error bars indicate s.d. (n=3). **d**) Growth rate curves of WT and KO ESCs in 2i/LIF. **e**) Phase and immunostaining for pluripotency markers on WT and Mettl14 KO naïve ESCs. **f**) qPCR analysis for differentiation (left panel) and pluripotency gene expression (right panel) after 8 days of EB induction. Error bars indicate s.d. (n=3). **g**) Western blot analysis for naïve WT, Mettl13 and Mettl14 KO ESCs. The results indicate that direct knockout of Mettl3 or Mettl14 results in protein loss of the other. Arrows highlight specific relevant band.

Divergent response of naïve, primed and metastable mESC to Mettl3 depletion

Crystal Zhao group conducted in 2014³⁶ perturbation experiments with shRNA against Mettl3 and Mettl14 in mouse ESC. The paper described that mouse ESC undergo differentiation under Mettl3/Mettl14 KD and suggested that m⁶A destabilized developmental regulation genes and upon its depletion, the latter gene group becomes more stable and the ES cells undergo differentiation.

The results of that study³⁶ seems inconsistent with our results that show that KO of Mettl3/Mettl14 makes our ESC "hyper-pluripotent" and the cells lose their normal ability to exit the naïve pluripotent state and further differentiate. However, we believe that this is not the case. Looking more closely at the culture condition of Wang et al. we could see that they culture their mouse ESC on feeder free gelatin coated plate with FBS/serum conditions. This sup-optimal culture condition generate metastable naïve condition that share several features in common with primed EpiSC (e.g. H3K27me3 deposition at bivalent genes in FBS/LIF expanded ESC is similar to primed EpiSCs, and not to ground state naïve ESCs grown in 2i/LIF)⁶⁹. We can appreciate by the morphology of Wang et al. cells that they expand in poor culture condition and lose the naïve-like pluripotent morphology (Fig. 14).

To deeply investigate this discrepancy in our results we thought to compare side-by-side the effect of Mettl3 depletion in ground state naïve (2i/LIF), metastable naïve (FBS/LIF) and primed EpiSC genetically matched mouse pluripotent cells that carry Oct4-GFP (pluripotent reporter) or deltaPE-Oct4-GFP (Naïve specific pluripotent reporter). The cells were expanded 10 days in each culture condition before the transfection with Mettl3 siRNA. Indeed Mettl3 knockdown in FBS/LIF (C57BL/6) or EpiSC (C57BL/6 and C57BL/6/129Jae cells), led to differentiation and down-regulation of Oct4-GFP+ cells, while Mettl3 knockdown in naïve 2i/LIF cells did not compromise their stability, consistent with our initial KO results (Fig. 15a). Importantly, the divergent response to Mettl3 depletion of naïve and primed pluripotent cells was evident by qPCR analysis, which showed that naïve cells express high levels of pluripotency genes and low levels of lineage commitment markers. Mettl3 depletion amplifies the highly expressed

naïve pluripotency genes and further boosts naïve circuitry stability (Fig. 16b-d). As the cells progress towards primed EpiSCs, pluripotency genes are down regulated and lineage commitment markers become highly expressed (Fig. 16b-d). At this stage, *Mettl3* depletion by siRNA leads to minimal amplification of pluripotency genes and further boosts the already upregulated lineage commitment markers, leading to tipping the balance towards differentiation (Fig. 3e).

We next evaluated influence for *Mettl3* depletion on reprogramming towards naïve pluripotency (Fig. 15b). During primed EpiSC reprogramming to naïve pluripotency, early depletion of *Mettl3* had a negative effect on efficiency (Fig. 15c), consistent with its negative influence on stability of primed pluripotent state (Fig. 16b). However, *Mettl3* depletion during late stages of EpiSC reprogramming significantly boosted reversion efficiency (Fig. 15d).

These results highlight the divergent dependence on *Mettl3* to maintain naïve and primed pluripotent cells, and the importance in carefully evaluating outcomes following introducing perturbations in distinct pluripotent states (Fig. 17).

Figure 14

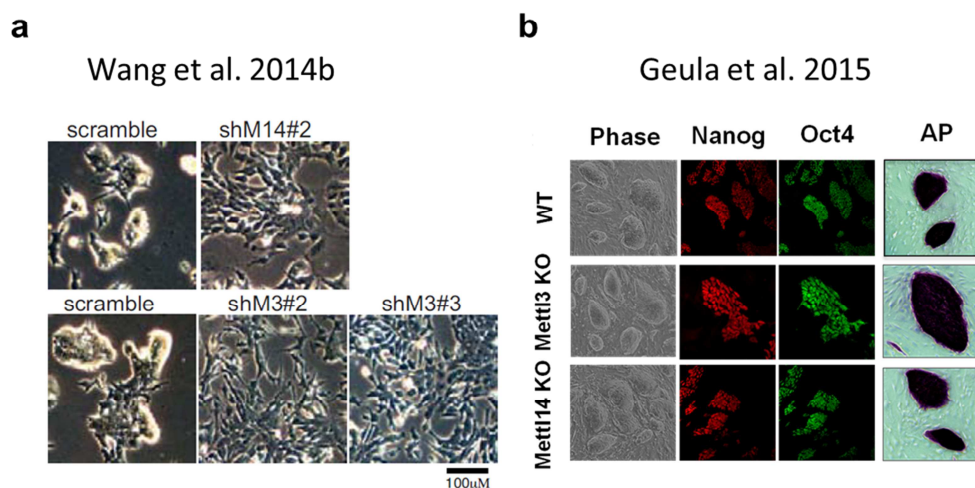


Figure 14: Wang et al paper- *Mettl3/14* Knock-down leads to destabilization of pluripotency a) mouse ESC morphology after Know-down of *Mettl3/14*. The cells cultured in non-stringent conditions (gelatin+serum/LIF), and can see that the cell morphology is not typical to naïve mESC. b) mESC morphology under stringent naïve promoting culture conditions (feeders+N2B27 2i/LIF).

Figure 15

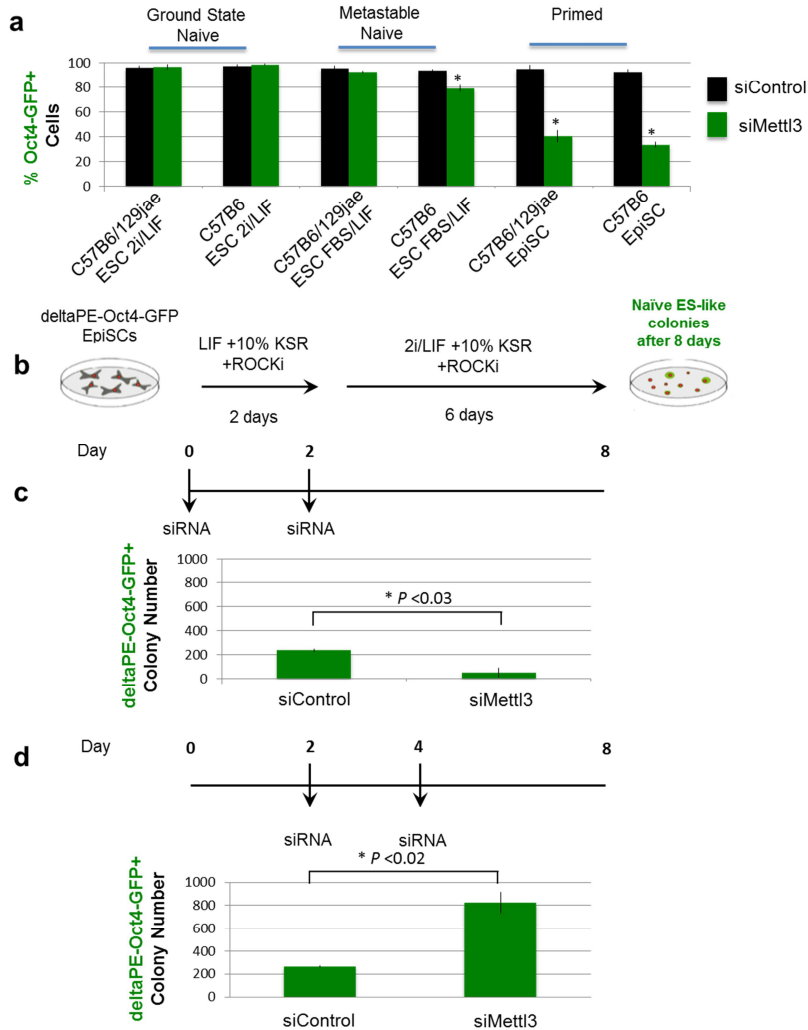


Figure 15: Divergent effect of Mettl3 depletion on naïve and primed mouse pluripotent cells. **a)** Oct4-GFP knock-in V6.5 and C57B/6 pluripotent cells expanded in either ground state naïve N2B27 2i/LIF, Metastable Naïve FBS/LIF, primed-N2B27 FGF2/Activin on matrigel coated plates. Mettl3 depletion did not compromise pluripotency stability of naïve cells, but only primed cells. Metastable naïve cells, only C57B6 cells showed a slight decrease in pluripotency maintenance upon Mettl3 depletion. This result is consistent with the fact that C57B6 ES cells are less stable and have increased primed pluripotency feature in comparison to hybrid V6.5 C57B6X129Jae F1 ES cells which are relatively more stable in FBS/LIF conditions. **b)** Schematic for EpiSC reversion and reprogramming strategy to naïve pluripotency. **c)** Efficiency of EpiSC reversion to naïve pluripotency was evaluated by counting deltaPE-Oct4-GFP+ colonies. Note that early depletion of Mettl3 hampers the reversion; consistent with the fact that it disturbs primed pluripotent cells. **d)** Depletion of Mettl3 at later stage of the reversion positively regulates reprogramming to naïve pluripotency. These results show an opposing effect for Mettl3 depletion on murine naïve and primed pluripotency.

Figure 16

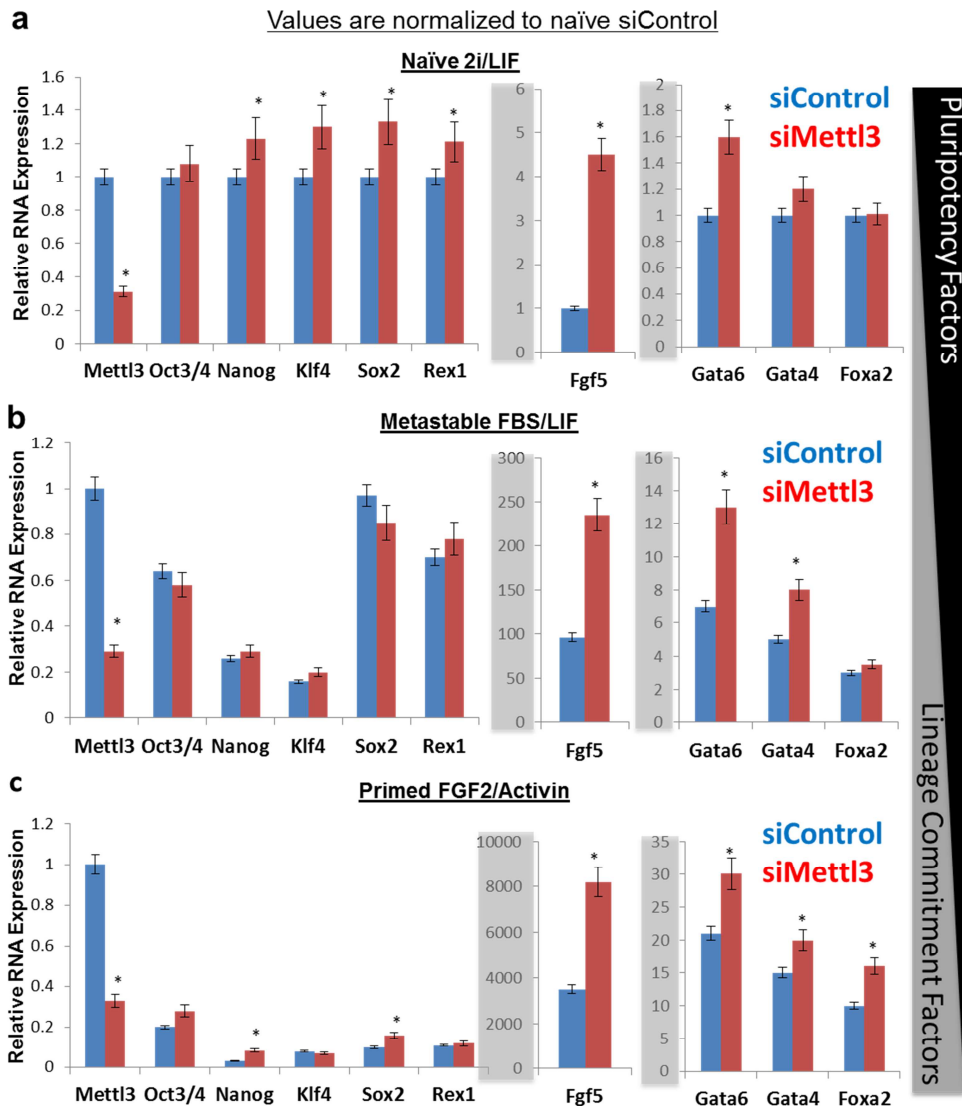


Figure 16: Divergent effect of Mettl3 depletion on naïve and primed mouse pluripotent cells. a-c) V6.5 derived pluripotent cells were cultured in different media conditions (Ground state naïve N2B27 2i/LIF, Metastable Naïve FBS/LIF, primed-N2B27 FGF2/Activin), on matrigel covered plates. The cells were transfected with Mettl3 or control siRNA. After 120h RNA was extracted and cells were analyzed by qPCR. Mettl3 knockdown enhanced stabilized both pluripotent genes (Nanog, Klf4, Sox2 and Rex1) and differentiation genes (Fgf5, Gata4, Gata6). Values were normalized to ground state siControl naïve sample. This demonstrates the high levels of pluripotency genes in naïve cells, and low levels of lineage commitment markers. The opposite occurs as the cells become primed. Mettl3 depletion leads to amplification of already expressed genes, thus those expressed at high levels dominate. For example note that Fgf5 levels become extremely high in Mettl3 depleted primed cells.* indicates p value < 0.05 .

Figure 17

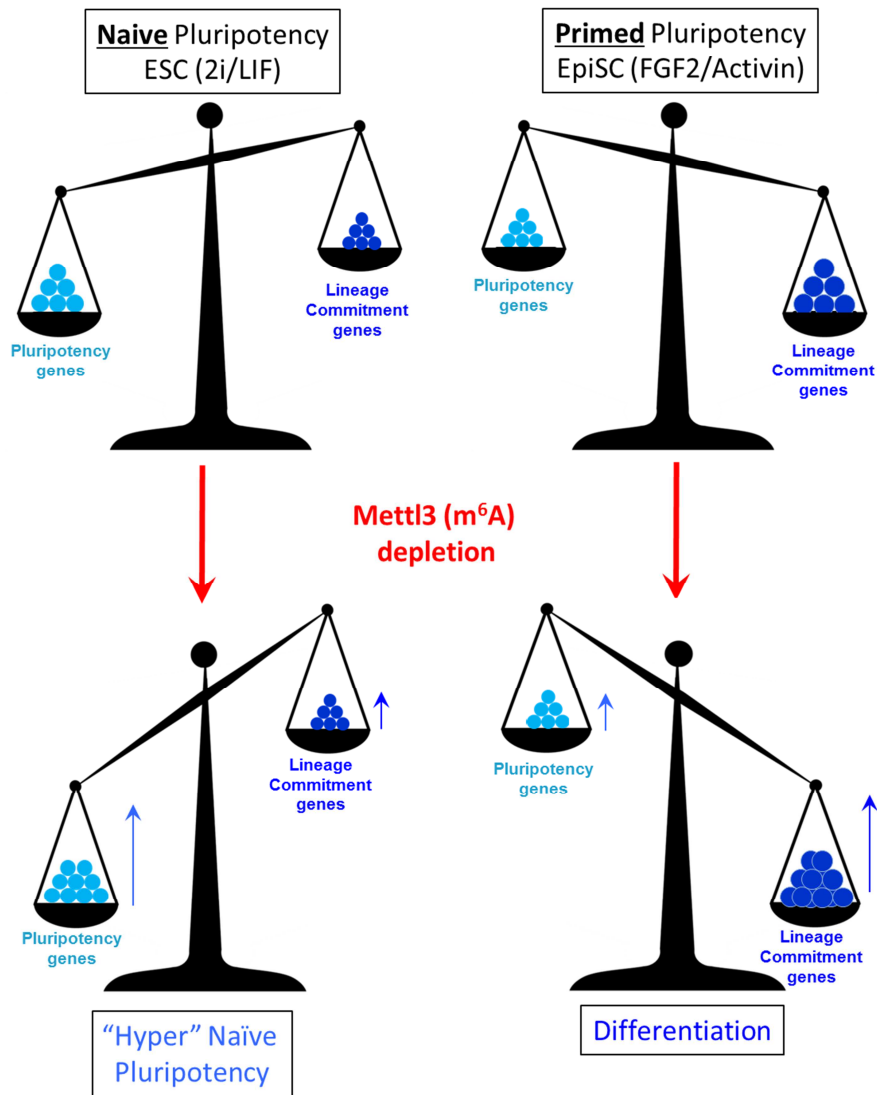


Figure 17: Divergent effect of *Mettl3* depletion on naïve and primed mouse pluripotent cells. A schematic illustration demonstrating the balance between expression levels of pluripotency genes and of lineage commitment genes in naïve and primed states. The expression levels of differentiation markers in naïve cells are very low, and it increases with priming. The opposite applies to pluripotency genes. Thus the outcome of *Mettl3* depletion has an opposite effect on naïve and primed states, because in primed cells the primed genes are expressed at much higher levels, and their further boosting pushes a threshold toward differentiation, despite the slight increase in the weakly expressed pluripotency genes. *Mettl3* depletion in Naïve pluripotent cells creates a “hyper” naïve pluripotent states because the already high naïve pluripotency genes become increased, while the lineage commitment genes remain at residual very low levels. Thus, the outcome of the pluripotency (de)stabilization can change between media conditions depending on the state they promote (naïve or primed).

The effect of Mettl3 depletion on somatic cell reprogramming into iPSCs

Finally, we wanted to check the effect of Mettl3 depletion on mouse iPSC generation. We used secondary OKSM tetracycline induced MEF system that also carry Oct4-GFP pluripotent reporter and analyzed iPSC formation after 16 days of dox induction by Oct4-GFP FACS analysis, SSEA-1 (pluripotent surface marker) and AP staining.

Applying Mettl3 depletion during somatic iPSC reprogramming after at least 3 days of reprogramming factor induction did not compromise iPSC reprogramming efficiency (Fig. 18 a-d), consistent with Mettl3 being dispensable for ICM naïve pluripotency establishment *in vivo* (Fig. 2, Fig 3). Notably, Mettl3 depletion during early stages of reprogramming reduced iPSC derivation (Fig. 18 e-f), however this can be attributed to severe block in somatic cell replication (Fig. 18g), rather than epigenetic reconfiguration per se. Collectively, loss of Mettl3 compromises the stability of adequately established primed pluripotent cells and promotes establishment of naïve pluripotency from EpiSCs.

Figure 18

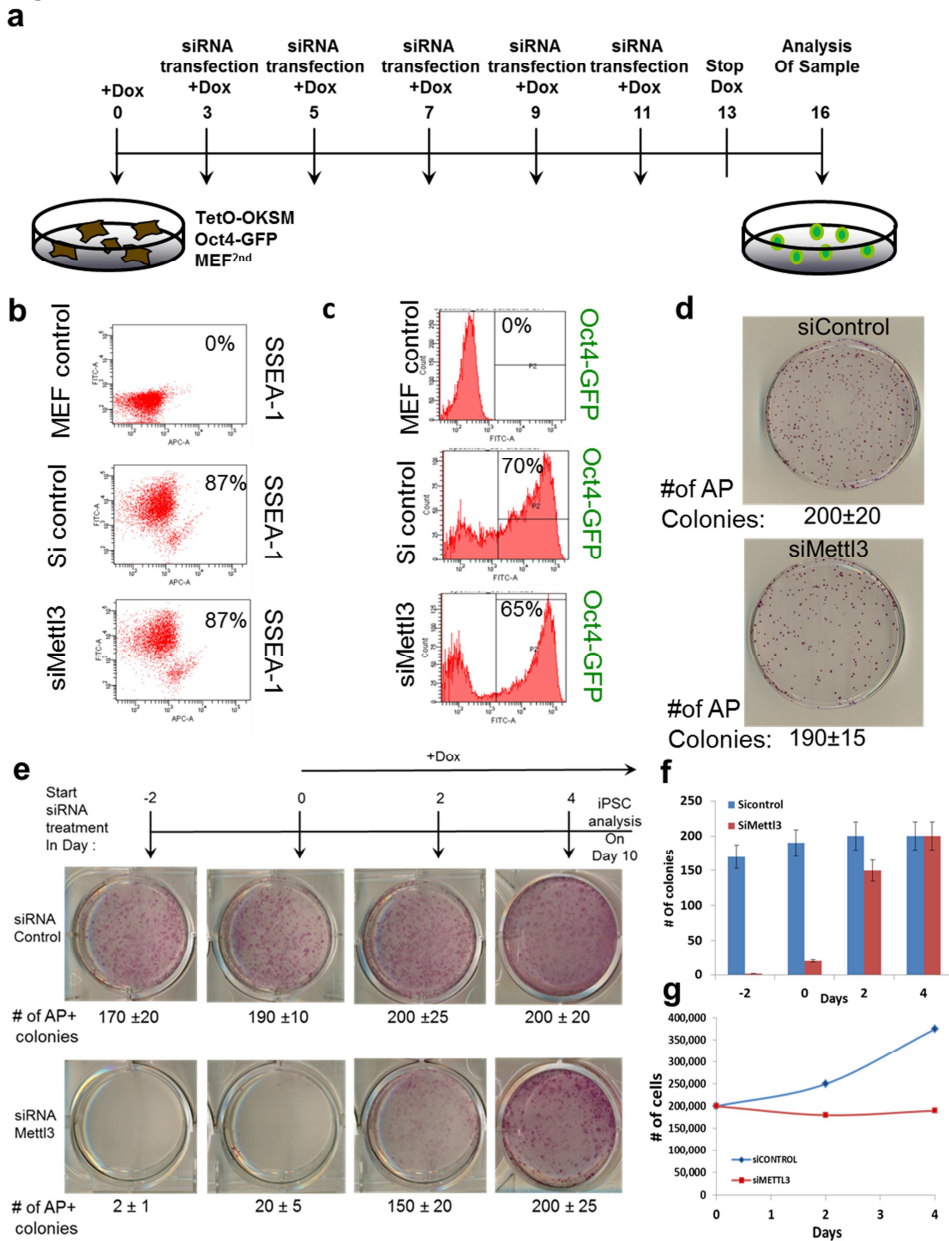


Figure 18: Mettl3 is dispensable for somatic into iPSC reprogramming.

a) 1×10^4 secondary MEFs transgenic for Dox inducible STEMCCA-OKSM vector carrying Oct4-GFP (GOF18) transgenic reporter were plated on gelatin covered plate and reprogramming was induced by adding 2ug/ml doxycycline. siRNA transfections were started in day 3 as indicated in the scheme. b) Cell reprogramming outcome conducted in (a) was analyzed by FACS for SSEA-1 expression at day 12. c) iPSC reprogramming of MEF cells was analyzed by FACS for Oct4-GFP expression at day 16. d) MEF reprogramming was also analyzed by AP activity assay in day 16. e+f) 1×10^4 secondary MEFs transgenic for Dox inducible STEMCCA-OKSM vector were plated on gelatin covered plate and reprogramming was induce by adding 2ug/ml doxycycline. siRNA

transfection was started in -2, -1, 0, +2, +4 days relative to doxycycline addition. iPSC formation was analyzed in day 10 by AP activity assay. Numbers and s.d. of 2 technical replicates are shown. g) Proliferation rate of MEF after Mettl3 depletion. 2×10^5 MEF were plated and 24h later transfected with Mettl3 or control siRNA. 24h later cell were harvested and 2×10^5 cells were re-plated. Cells number were measure in day 2 and 4. One out of 2 representative experiments is shown. These results indicate that Mettl3 is only important for early reprogramming, however this is attributed to severe block in somatic cell replication. Applying Mettl3 depletion throughout reprogramming but after at least 3 days of DOX induction did not compromise iPSC reprogramming. The latter is consistent with Mettl3 being dispensable for ICM naïve pluripotency establishment in Mettl3 KO embryos.

Mettl3 regulates pluripotent state reconfiguration and lineage priming *in-vivo*

Mettl3 KO embryos show aberrant development in the post-implantation stage

We aimed next to determine the extent to which the *in vitro* observed phenotypes correlate with *in vivo* developmental dynamics. Mettl3 is uniformly expressed in the mouse developing embryos as we can appreciate from the activity of the LacZ reporter that we introduced into the Mettl3 locus (Fig. 19a), or by immune-staining of paraffin section embryo with Mettl3 antibody (Fig. 19g).

We crossed F1 heterozygote offspring mice to obtain Mettl3^{-/-} litters. Genotyping of F2 newborn pups yielded no newborn KO mice with no evidence for escape mutants (n=202), leading to the conclusion that the KO of Mettl3 is embryonic lethal (Fig. 2a and Fig. 19b-d). Next, we aimed to detect the exact stage in which the embryo stops to develop. We started by looking at E12.5, E10.5 and E8.5 embryos and found that all KO embryos were absorbed (at expected 25% ratio, Fig. 19b-d). By examining earlier developmental stages, we found that E3.5 knockout blastocysts show normal morphology and were obtained at the expected Mendelian ratio consistent with the ability to form naïve pluripotency *in vivo* and *in vitro* (Fig. 2b-d and Fig. 3). However, post-implantation E5.5-E7.5 KO embryos were smaller in size (consistent with the observed reduced *in vitro* growth rate Fig. 3d), deformed and deficient in adopting the typical post-implantation epiblast egg cylinder shape (Fig. 19e-h). From this observation we conclude that Mettl3 KO defects manifested in or during the post-implantation stage during the *in vivo* transition between naïve to primed pluripotency state.

Mettl3 KO embryos show aberrant pre-implantation markers expression in the post-implantation stage

Closer examine of the Mettl3 KO post-implantation embryo shows that Oct4+ cells were readily detected at E5.5-E7.5 KO post-implantation epiblasts suggesting that pluripotent cells existed *in vivo* and excluded precocious differentiation as the cause for embryonic lethality (Fig. 19h and Fig. 20).

Remarkably, the typical down-regulation and retraction in Nanog (naïve pluripotent marker) expression seen in WT embryos at E5-E5.5, was not observed in KO embryos (Fig. 21a). Moreover, at E6.0-7.5, Nanog expression in WT embryos is reinitiated and restricted to proximal posterior epiblast (Fig. 21b)⁷⁰, however in KO embryos Nanog was diffusely expressed throughout the Oct4+ post-implantation epiblast cells (Fig. 21 and Fig. 22). In addition, Tfe3 showed exclusive cytoplasmic localization in WT embryos, but mixed cytoplasmic and nuclear Tfe3 localization was observed only in some of the KO embryos (Fig. 23), consistent with reduced tendency for priming⁷¹.

Mettl3 KO embryos show do not upregulate normally lineage markers in the post-implantation stage

Remarkably, reduced competence to undergo priming was also evident by the fact that early lineage markers such as Brachyury or Foxa2 were not induced in KO embryos (Fig. 24 and Fig. 25), consistent with our *in vitro* findings (Fig. 9 and Fig. 10).

However, the naïve pluripotency marker Esrrb was down-regulated in both WT and KO post-implantation embryo epiblasts. Furthermore, the up regulation of the primed marker Otx2 and the inactivation of the X chromosome in XX embryos occur both in WT and KO cells (Fig.26 a-c), indicating that some level of pluripotency priming does occur and that the phenotype is less severe in some characteristics relative to that characterized *in vitro*.

Collectively, the retention of widespread Nanog expression, maintenance of Oct4 expression without up-regulating lineage commitment genes *in vivo* are consistent with the *in vitro* observed phenotypes, and reiterate resistance to terminate naïve pluripotency and the formation of an aberrant primed pluripotent state in Mettl3 KO embryos *in vivo*.

Figure 19

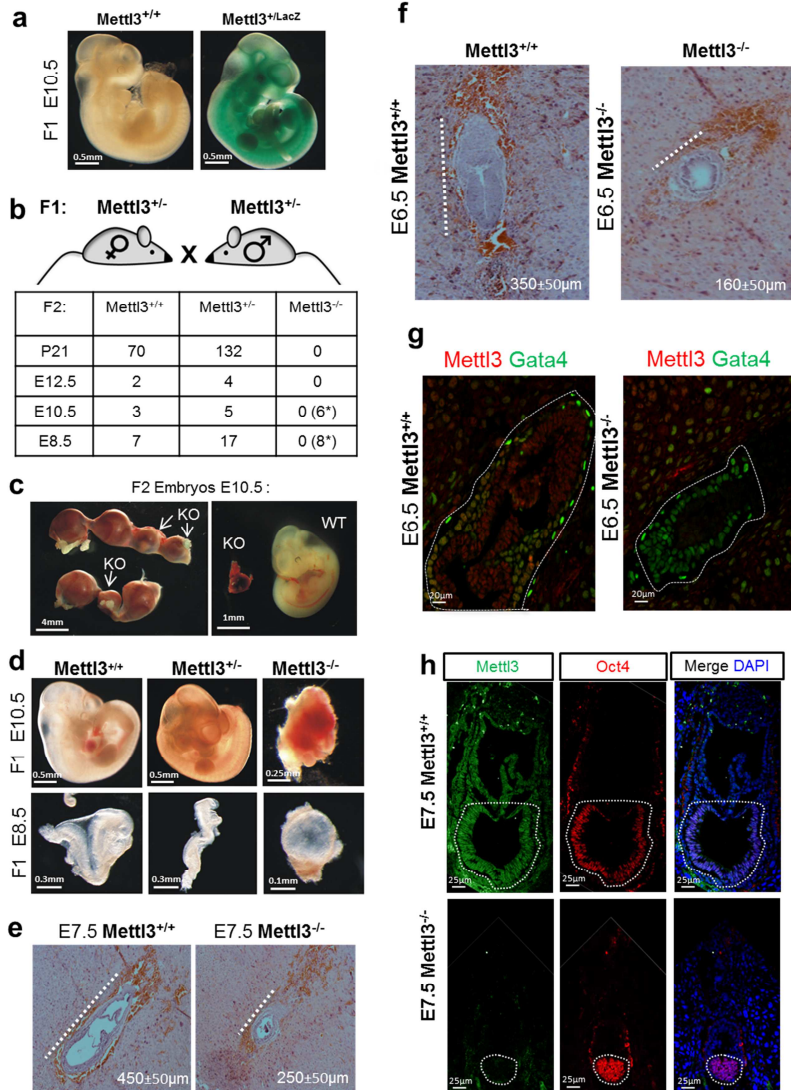


Figure 19: *Mettl3* is critical for proper embryo post-implantation *in vivo*. **a)** LacZ staining of WT and *Mettl3*^{LacZ/+} embryo, showing ubiquitous expression of *Mettl3* locus in the embryo. **b)** *Mettl3*^{+/-} mice were crossed and pups were genotyped for *Mettl3* Exon4 and for the LacZ cassette. Table summarizes number of embryos detected at each developmental stage. No living pups carrying double *Mettl3* exon4 deletion (n=202) were born. *Indicates *Mettl3*^{-/-} absorbed embryos at E8.5-E10.5. **c-d)** Representative *Mettl3*^{+/-} cross litter at E10.5 and E8.5, showing absorbed embryos, either in the uterus or after dissection. **e-f)** H&E staining of WT and KO E7.5/E6.5 histological section. The KO embryos are smaller by a factor of 1.8 and lost the typical post-implantation epiblast egg cylinder shape. **g)** Immunostaining of WT and KO E6.5 histological section, for *Mettl3* (red) and *Gata4* (green). The KO embryos do not stain positive for *Mettl3*, yet show normal development of primitive endoderm (PE) *Gata4* positive cells. PE is marked with dash line. **h)** Immunostaining of WT and KO E7.5 histological section, for *Mettl3* (green), *Oct4* (red) and DAPI (blue). KO embryos are negative for *Mettl3*, but stain positive for *Oct4* pluripotent marker in the Epiblast (dashed outline).

Figure 20

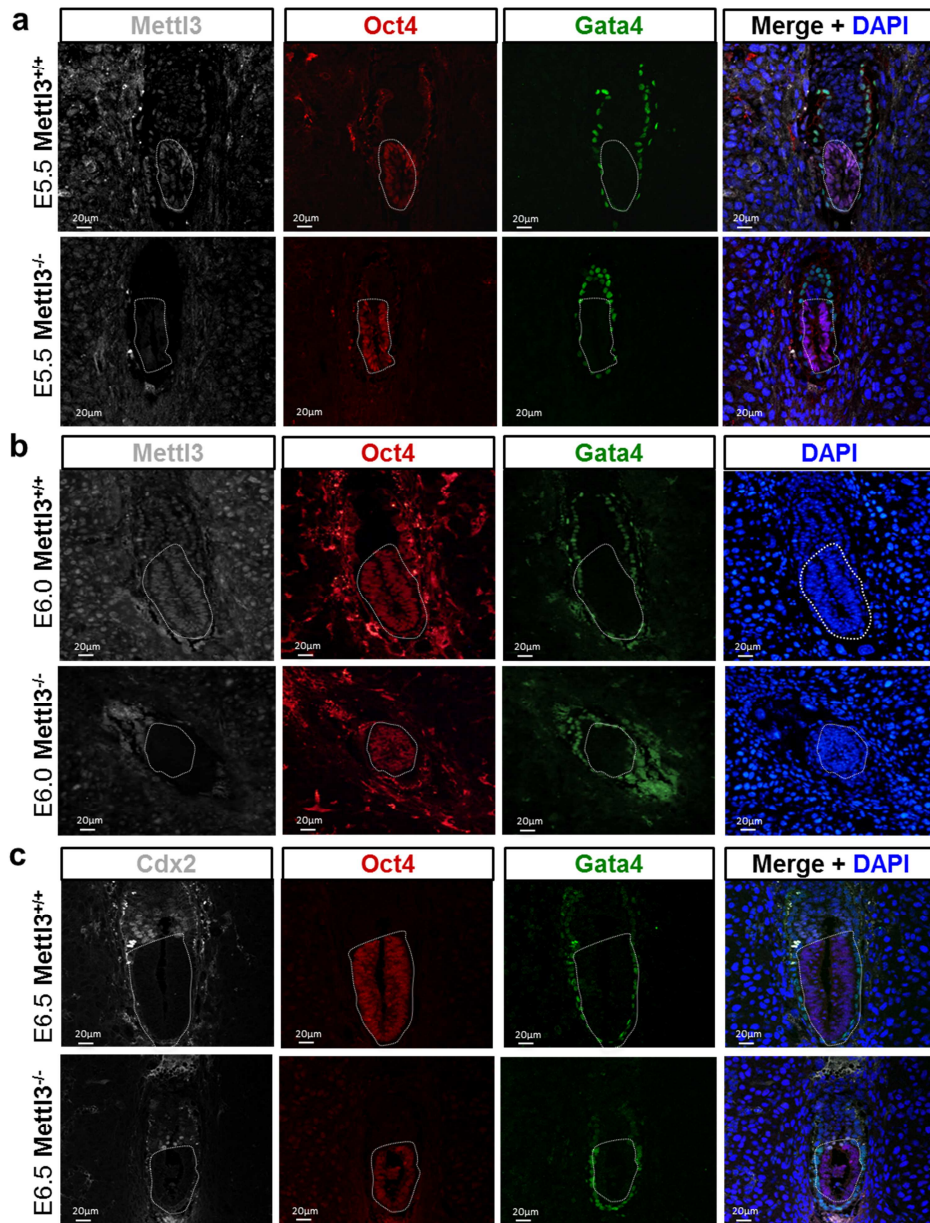


Figure 20: Mettl3 KO embryos show abnormal post-implantation morphology, while maintaining the expression of Oct4 in the epiblast pluripotent cells. Immunostaining of WT and KO histological sections. Dashed line marks the post-implantation epiblast part of the embryos. a) E5.5 and b) E6.0 embryos were stained with Mettl3 (gray), Oct4 (red, pluripotent marker) and Gata4 (green, primitive endoderm marker). c) E6.5 embryos were stained with Cdx2 (grey, extra-embryonic marker), Oct4 (red) and Gata4 (green). Note that post-implantation KO epiblasts continued to retain Oct4⁺ cells, excluding precocious differentiation and loss of pluripotency defects.

Figure 21

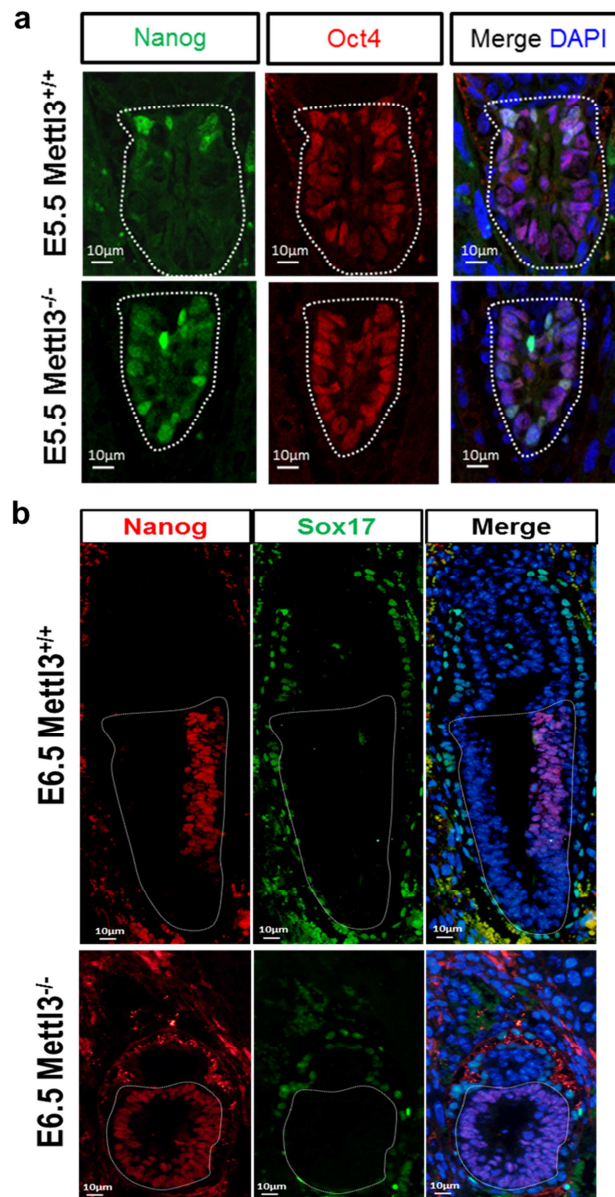


Figure 21: Aberrant expression of Nanog in Mettl3 KO Oct4+ post-implantation epiblast. Immunostaining of WT and KO histological sections. Dashed line marks the post-implantation epiblast part of the embryos. **a-b)** WT and KO E5.5 embryos. Nanog (naïve pre-implantation marker) is normally down regulated in the post-implantation E5-E5.5 embryo and is re-expressed at E6.0-E7.5 only in the proximal-posterior part of the epiblast (see WT at b). In KO embryos, not only Nanog was not down regulated at E5.5, but it was also expressed in nearly the entire Oct4+ epiblast cells and showed no spatiotemporal restriction. This result is consistent with aberrant termination of naïve pluripotency in Mettl3 KO embryos *in vivo*.

Figure 22

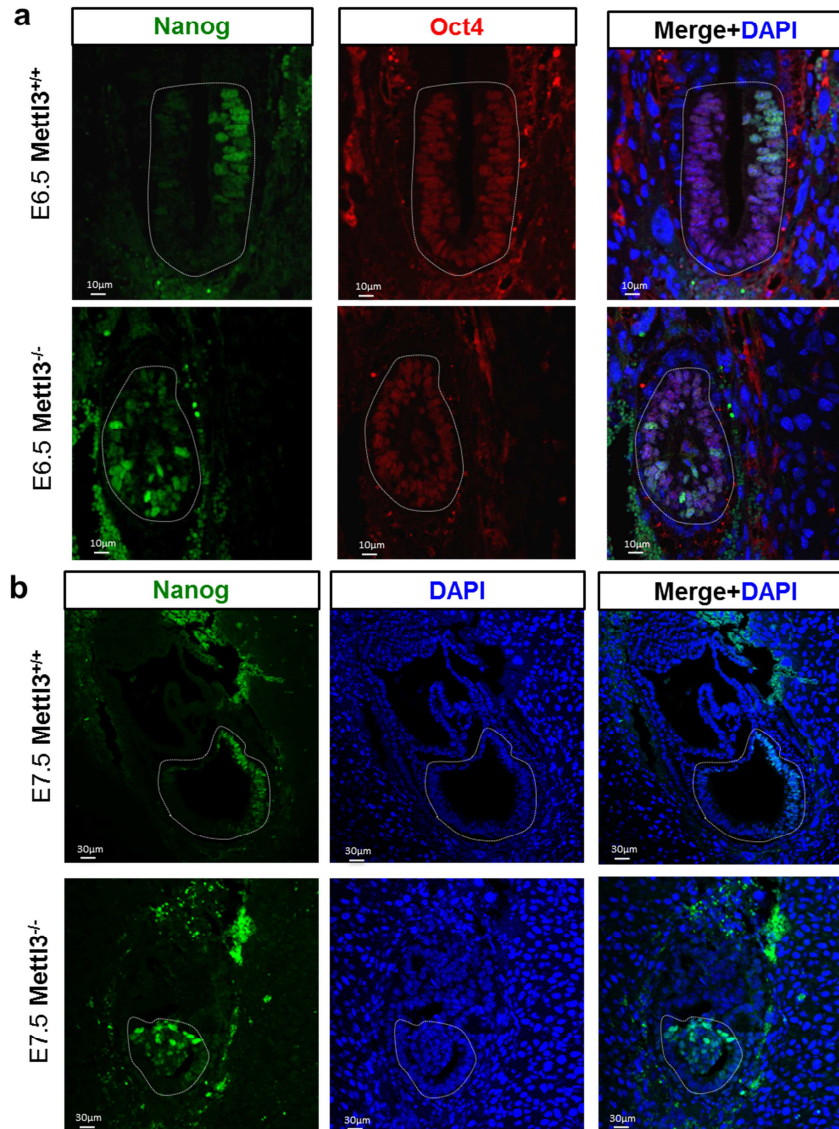


Figure 22: Aberrant expression of Nanog in *Mettl3* KO Oct4+ post-implantation epiblast. Immunostaining of WT and KO histological sections. Dashed line marks the post-implantation epiblast part of the embryos. **A-b)** Additional example of *Mettl3* KO Nanog expression.

Figure 23

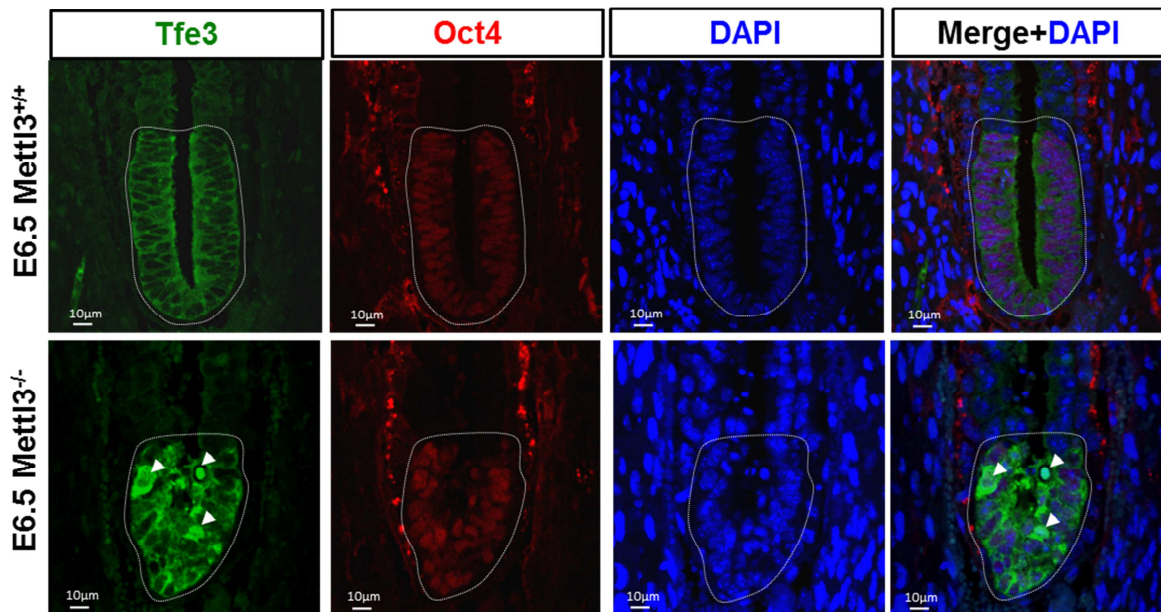


Figure 23: Mettl3 KO embryos undergo incomplete priming. Immunostaining of WT and KO embryo histological sections. Dashed line marks the post-implantation epiblast part of the embryos. E6.5 embryos were stained with Tfe3 (green) and Oct4 (red) pluripotency markers. While Tfe3 showed exclusive cytoplasmic localization in WT embryos, mixed cytoplasmic and nuclear Tfe3 localization was observed only in KO embryos (white arrowheads).

Figure 24

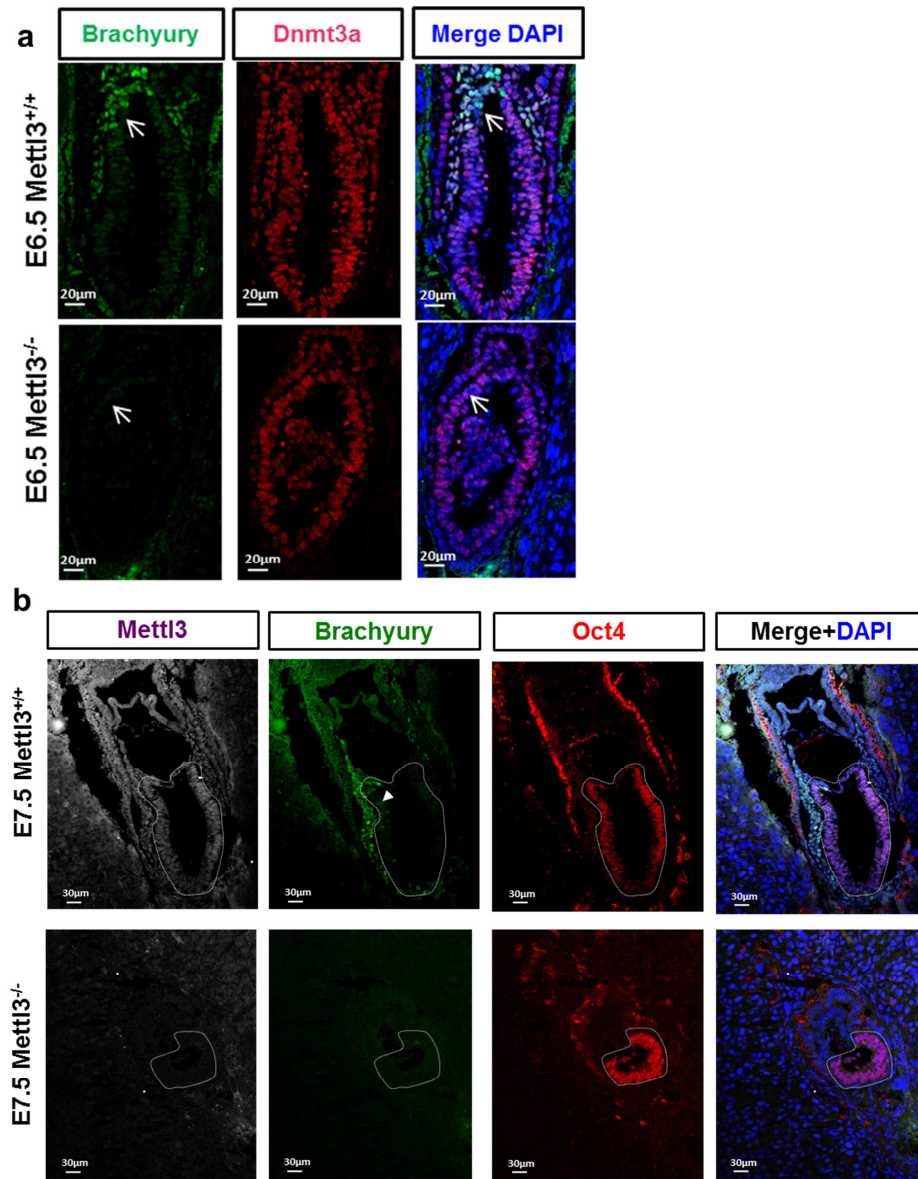


Figure 24: Mettl3 KO embryos failed to upregulate lineage commitment markers and undergo differentiation priming. Immunostaining of WT and KO embryo histological sections. The dashed line marks the post-implantation pluripotent epiblast part of the embryos. **a)** E6.5 embryos were stained with Brachyury (green, Mesodermal marker) and Dnmt3a (red, primed marker). (n=3). **b)** E7.5 embryos were stained with Mettl3 (gray), Brachyury (green, Mesodermal marker) and Oct4 (red, pluripotent marker). The KO embryos failed to up-regulate the early-developmental marker Brachyury in the post-implantation epiblast, while WT embryos expectedly did (white arrowhead) (n=4).

Figure 25

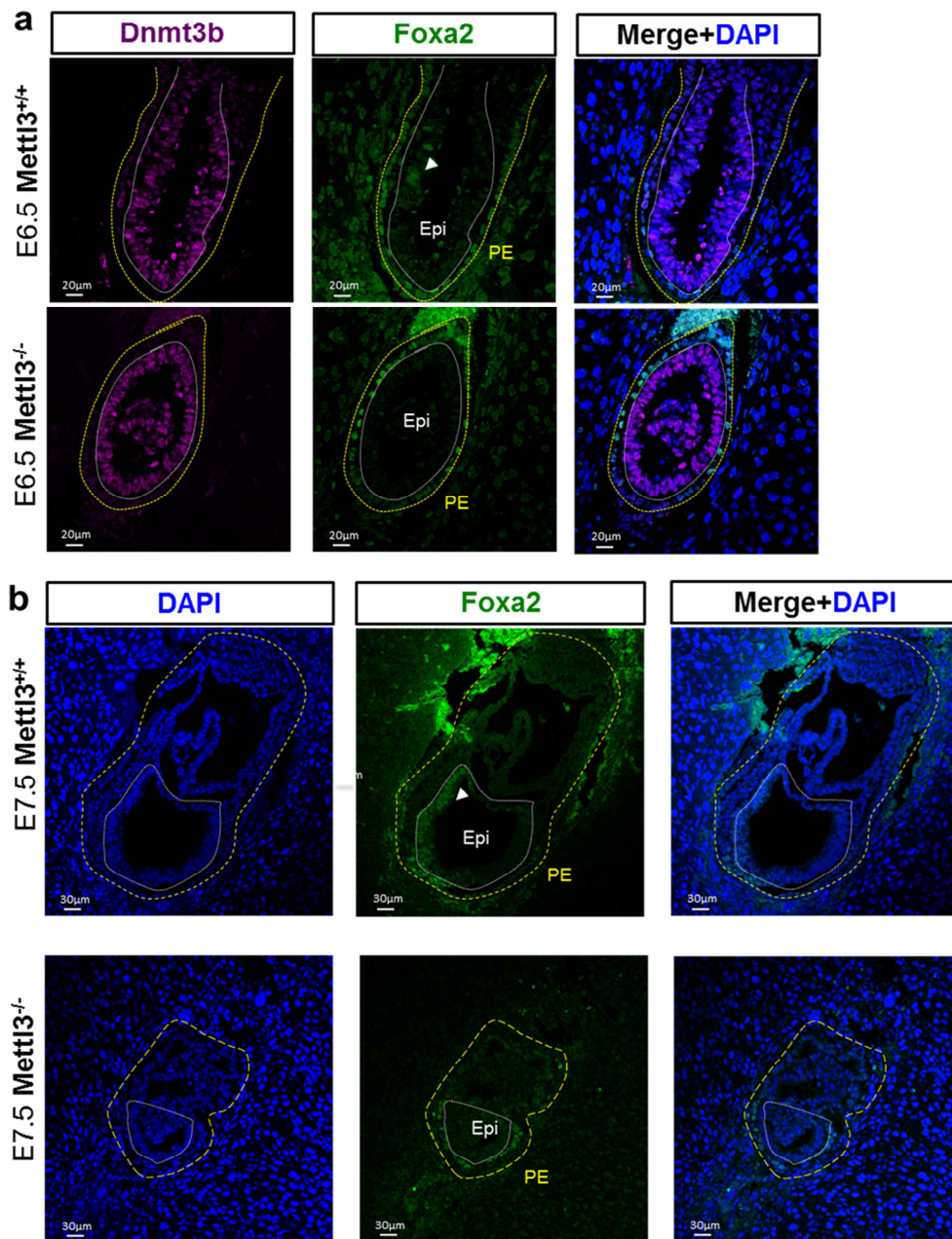


Figure 25: *Mettl3* KO embryos fail to upregulate key lineage commitment markers and undergo differentiation priming. Immunostaining of WT and KO histological sections. The dotted white line marks the pluripotent post-implantation epiblast (Epi) part of the embryo, and the yellow dashed line marks the primitive endoderm (PE). **a** E6.5 embryos were stained with *Dnmt3b* (magenta) and *Foxa2* (green, Endodermal marker). The KO embryo, like the WT, up-regulated *Dnmt3b*, but failed to up-regulate the early-development marker *Foxa2* in the post-implantation epiblast. Notice that the only cells that expressed *Foxa2* in the KO embryo are in the PE part. **b** E7.5 embryos were stained with *Foxa2* (green). As in **a**, the KO embryo failed to express *Foxa2* in the Epiblast, and expressed it only in the PE. (n=4)

Figure 26

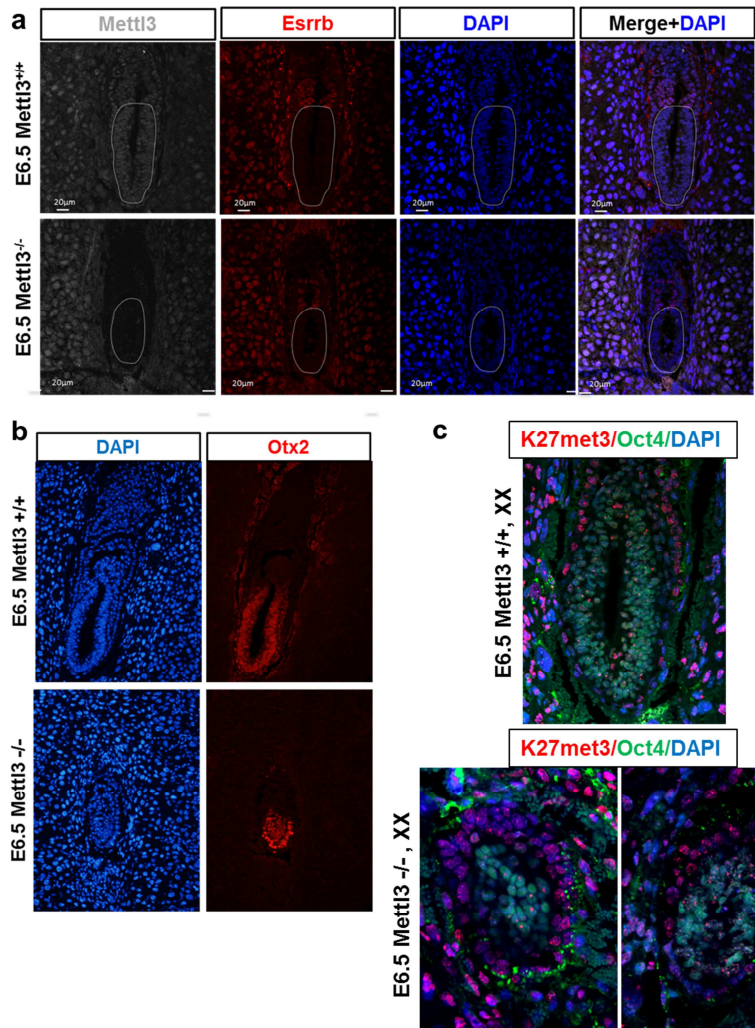


Figure 26: *In-vivo* Mettl3 KO embryos exhibit less severe phenotype as *in-vitro* cells and show partially priming. a) E6.5 embryos were stained with Mettl3 (gray) and Esrrb (red, naïve pluripotency marker). Both WT and KO embryo down-regulate the expression of Esrrb in the post-implantation epiblast *in vivo*. b) E6.5 embryos were stained with Otx2 (red, primed marker). Both WT and KO embryo up-regulate the expression of Otx2 in the post-implantation epiblast *in vivo*. c) E6.5 embryos were stained with Oct4 (green) and K27met3 (red, X inactivation primed marker). Both WT and KO female embryo undergo X inactivation in the post-implantation epiblast *in vivo*. These results suggest that some level of pluripotency priming does occur *in vivo* of Mettl3 KO embryos, and that the phenotype is not entirely identical to the characterized *in vitro*. However, the retention of widespread Nanog expression, maintenance of Oct4 expression without up-regulating lineage commitment genes *in vivo* (Fig. 20-23) is consistent with the *in vitro* observed phenotypes.

The molecular mechanisms behind m⁶A modification

Our results show that the near absence of m⁶A in mRNA of *Mettl3*^{-/-} hampers priming and differentiation competence of naive pluripotent cells. To explore the roles of m⁶A modification in mRNA and its effects on gene expression regulation governing pluripotency and differentiation, we decided to analyze changes in different aspects of the mRNA molecule between WT and *Mettl3* KO cells. We aimed to track after the mRNA molecule through transcription, splicing, editing, export from the nucleus, translation and degradation (Fig. 27a).

Figure 27

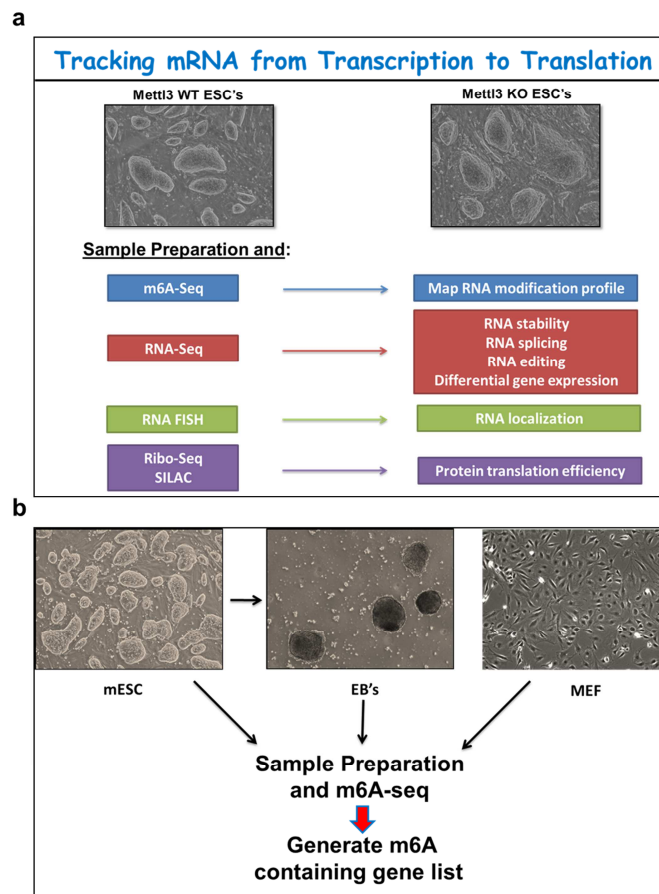


Figure 27: Decipher the molecular mechanism behind m⁶A mRNA modification.

a) Schematic description of the methods we used and the Data that we acquire from WT and *Mettl3* KO cells. b) m⁶A-seq from different cells type and generating m⁶A modifying transcripts list.

m⁶A-seq reveals m⁶A modification prevalence in pluripotent and differentiated cells

First we wanted to compose a list of the entire mRNA transcripts that undergo modification in our model system. In order to do so, we applied m⁶A-seq^{24,47} on mRNA purified from mouse naive ESC, 8-day old embryoid bodies (EB) and mouse embryonic fibroblasts (MEFs) (Fig. 27b). Reads were aligned to the mouse genome (mm10) and peaks were identified. To assess the robustness of the peak assemblies we compared the peaks called in different biological replicates. In all analyses peaks were considered only if their fold change (FC) was ≥ 2 at false detection rate (FDR) value $\leq 5\%$, and they appeared at least in 2 out of 3 independent biological replicates (Methods). We identified 10,431, 8,356 and 11,948 m⁶A peaks within 6,412, 5,504 and 6,427 adequately expressed, annotated genes of ESC, EB, and MEFs, respectively, which constitute 33-41% of expressed genes (data available on NCBI GEO: GSE61998, Geula et al 2015, Examples are presented in Fig. 28, 30-32, and Supplementary Table S1).

We then performed quality control validation and check of our data. Unbiased search for motifs enriched in regions surrounding both ESC and EB m⁶A peaks using MEME^{24,48} recapitulated the previously established m⁶A consensus motif (Fig. 29a). The distribution of the m⁶A consensus motifs around the peak summit revealed increased density of motifs flanking the summits relative to negative control peaks (Fig. 29b). In addition, ESC and EB m⁶A peaks exhibited the expected a non-random distribution along transcript architecture, appearing mostly around stop codons and within long internal exons (Fig. 29c-d), similar to previously characterized methylomes^{24,33}. Both ESC and EB m⁶A methylomes display a non-monotonic relationship between methylation and expression levels, where transcripts of moderately to mid-highly expressed genes are more likely to be methylated, and transcripts of genes expressed at the two extremes are less methylated (Fig. 29e).

To validate our ability to specify uniquely m⁶A peaks, we performed m⁶A-seq on RNA obtained from Mettl3 KO ESC, where m⁶A levels in mRNA are virtually undetectable by LC-MS/MS. Only 995 peaks out of the 10,432 WT ESC were detected in KO. The overwhelming majority of the detected peaks (63%) correspond to cap

associated m⁶Am (N⁶,2'-O-dimethyladenosine) modification near the TSS, which is not deposited by Mettl3 and is not detected by LC-MS/MS approach we applied, but is recognized by the antibody used for m⁶A-IP⁴⁷. The remaining 370 peaks (3.5% of the total WT ESC peaks) may indicate false positive peaks, and this number is in general agreement with the anticipated 5% FDR. Further support for this hypothesis may be found in the fact an unbiased motif search within the sequences of the 370 peaks failed to find neither the RRACH consensus motif nor any other significant known motifs (data not shown). Collectively, our results support major depletion of m⁶A from mRNAs following Mettl3 knockout, and high specificity of m⁶A-IP protocol applied herein. However, we cannot exclude residual compensatory m⁶A methyltransferase activity by other enzymes (e.g. Mettl14) when Mettl3 is fully depleted.

A search for functional enrichment of m⁶A methylated genes both in ES and EB revealed statistically significant enrichment of genes involved in various basic cellular processes such as transcription regulation, metabolic process regulation, protein phosphorylation and transport, cell cycle and development (FDR<1%, Fig. 29f). Importantly, 28 out of 35 critical naïve pluripotency promoting genes (80%) were methylated by m⁶A including Nanog, Klf4, Klf2, Esrrb, Prdm14, Utf1, but not Oct4 that is similarly expressed in both naïve and primed pluripotent states (Fig. 28a and Fig. 30, Supplementary Table 3). Lineage priming genes expressed in EB like Foxa2, Sox17 and Otx2, were also positive for m⁶A (Fig. 28b).

Figure 28

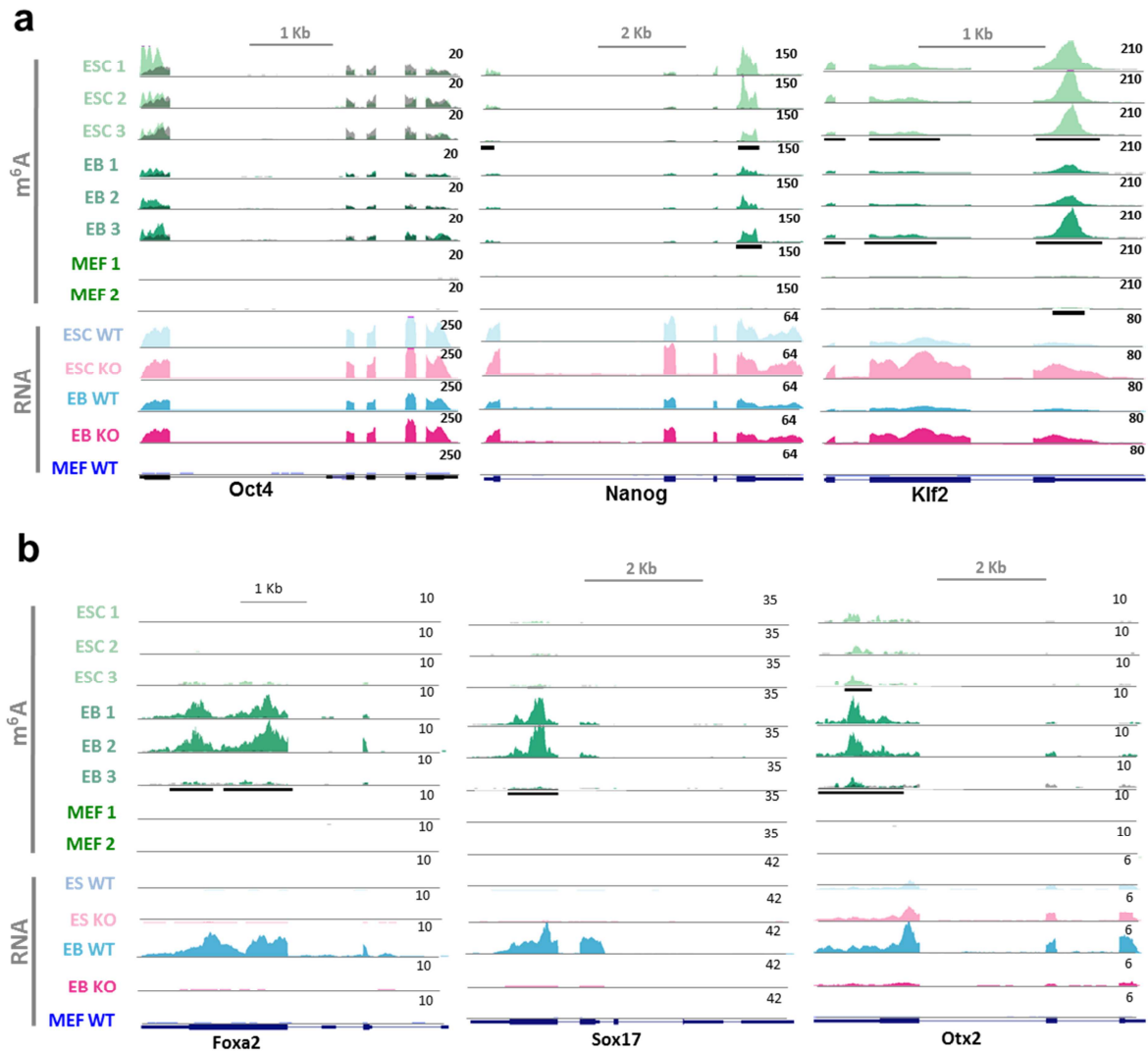


Figure 28: m⁶A-seq reveal m⁶A modification prevalence in pluripotent and differentiated cells. a-b Examples of m⁶A methylation (green) and transcriptional landscape (blue shades for WT and pink/red for Mettl3-KO) of Oct4, Nanog and Klf2 (pluripotent genes) and Foxa2, Sox17 and Otx2 (lineage commitment genes). Normalized read density (RPM) levels are shown, UCSC range is shown at the right side of each track. **Green** shades – m⁶A IP in ESCs, EBs and MEFs; **Gray** - m⁶A input in ESCs, EBs and MEFs; **Blue** shades – RNA-seq in WT ESCs, EBs and MEFs; **Pink** shades – RNA-seq in KO ESCs and EBs. In m⁶A samples all replicates are shown, in RNA-seq, one out of two replicates is shown. Significant peaks that appear in at least 2 out of 3 replicates, and at least 2-fold above input, are indicated in horizontal black squares. Levels are normalized by the number of reads in each sample. Note that Oct4 transcripts are not positive for m⁶A.

Figure 29

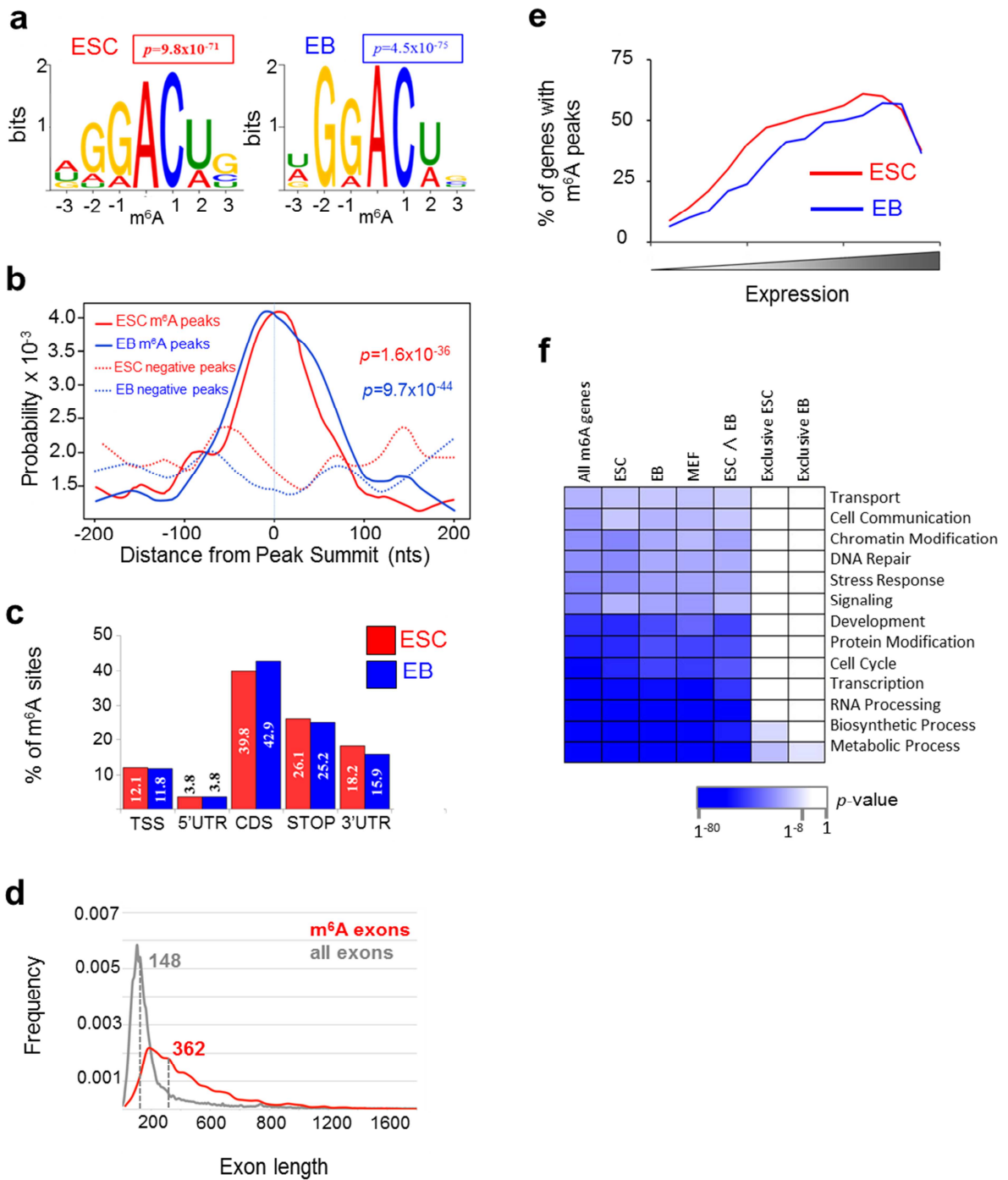


Figure 29: Molecular Characterization of m⁶A peaks. m⁶A profiles of WT ESC and EB (11days) were determined and analyzed. **a)** The previously identified consensus motif identified in m⁶A peaks of ESC (left, $p=9.8 \times 10^{-71}$) and EB (right, $p=4.5 \times 10^{-45}$) using MEME. **b)** Distribution of m⁶A consensus motifs around the peak summit was calculated using CentriMo in ESC (solid blue line) and EB (solid red line), showing increased density of the consensus motifs flanking the summits relative to negative control peaks (dashed lines). P-values are indicated in matching colors. **c)** Identified m⁶A peak distribution along the gene segments of ESC (blue) and EB (red). **d)** Distribution of exon length (in CDS only), show that exons carrying m⁶A (red line) tend to be significantly longer (T test $p < 1.9 \times 10^{-19}$, median=362 nts) compared to overall exon population (median=148, gray line). **e)** The fraction of ESC (red) and EB (blue) genes with m⁶A peaks as a function of expression level. Genes were divided into 25 bins according to their expression levels and the percentage of methylated genes in each bin was calculated. A non-monotonic relationship is observed. **f)** Compact representation of functional enrichment of methylated genes, that were calculated using gene ontology enrichment tool (<http://cbl-gorilla.cs.technion.ac.il>). Enrichment was calculated for all methylated gene lists of ESC, EB, MEF, methylated genes common to ESC and EB (ESC[∧]EB) and lists of exclusively methylated genes in ESC and EB (as indicated). GO analysis show enrichment of basic cellular processes such as metabolic processes, transcription, cell cycle, protein transport and development. Color shades reflect p-values according to the scale.

Figure 30

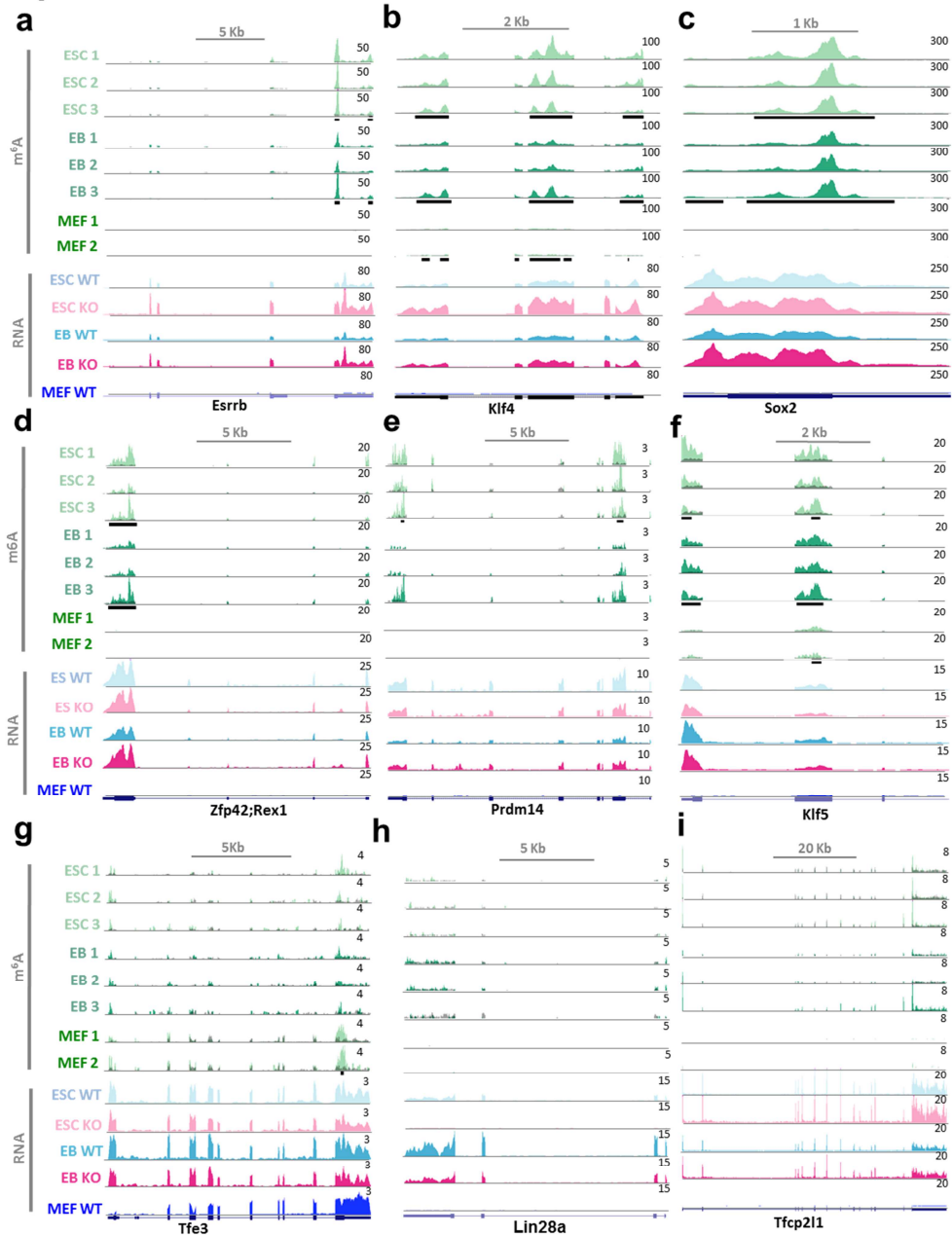


Figure 30: m⁶A methylation and transcriptional landscape of naïve pluripotency promoting genes. a-i) Normalized read density (RPM) levels are shown, UCSC range is shown at the right side of each track. **Green** shades – m⁶A IP in ESC, EB and MEF; **Gray** - m⁶A input in ESC, EB and MEF; **Blue** shades – RNA-seq in WT ESC, EB and MEF; **Pink** shades – RNA-seq in KO ESC and EB. In m⁶A samples all replicates are shown, in RNA-seq, one of out of two replicates is shown. Significant peaks that appear in at least 2 out of 3 replicates, and at least 2-fold above input, are indicated in horizontal black squares.

m⁶A topology and dynamics in pluripotent and differentiated cells

To evaluate the levels of m⁶A conservation and dynamics between ESC and EB, peak locations were first compared to identify common (overlapping) and unique (non-overlapping) peaks (Supplementary Table 2). We identified 7,205 ES peaks overlapping 6,765 EB peaks falling into 4,756 genes. A subset of 3,226 ESC peaks residing in 2,073 genes was uniquely identified in ESC, and 1,591 peaks in 1,407 genes were uniquely identified in EB. These numbers are comparable with the number of peaks obtained in yeast upon sporulation (1,308 peaks) (Schwartz et al., 2013). To estimate whether the uniquely identified peaks emerge from a differential methylation or from a mere difference in expression, RNA levels should be considered. We performed massively parallel sequencing of mRNA (mRNA-Seq) (Mortazavi et al., 2008) purified from WT and KO ESC and EB samples, in 2 biological replicates. Reads were aligned to the mouse genome (mm10) and mRNA levels were calculated. Samples of conserved m⁶A peak and differential m⁶A peak between MEF, EBs and ESC is presented in Figure 31.

We next compared (Fig. 32b-c) normalized peak levels (RPKM) in ESC compared to EB for the union of all peaks as well as for a subset of peaks that have similar mRNA level in both conditions (mRNA expression FC<1.2, shown in black), or peaks that their mRNA levels are above 2-fold higher in ESC (light blue), or in EB (blue). If methylation is differential, we should have identified cases of similar RNA and differential methylation, or cases in which methylation change is not consistent with the change in mRNA (e.g. mRNA higher in ESC, but methylation is higher in EB). Overall, most peaks in ESC and EB were correlated (Pearson R=0.547), however, there were 232 peaks mapped to 211 genes, in which the change in m⁶A methylation was not consistent with the change in expression. When comparing ESC to MEF, we observed lower correlation (Pearson R=0.346) and identified 1223 peaks mapped to 916 genes, of differential methylation that is not consistent with the change in expression (Fig. 32b, concrete examples Fig. 32c). These findings reiterate the notion that m⁶A distribution can be actively written or removed in distinguished mammalian cells, consistently with previous study in yeast⁷² and the discovery and expression of FTO and ALKBH5, two m⁶A mRNA demethylases in mammalian cells^{25,37}.

Figure 31

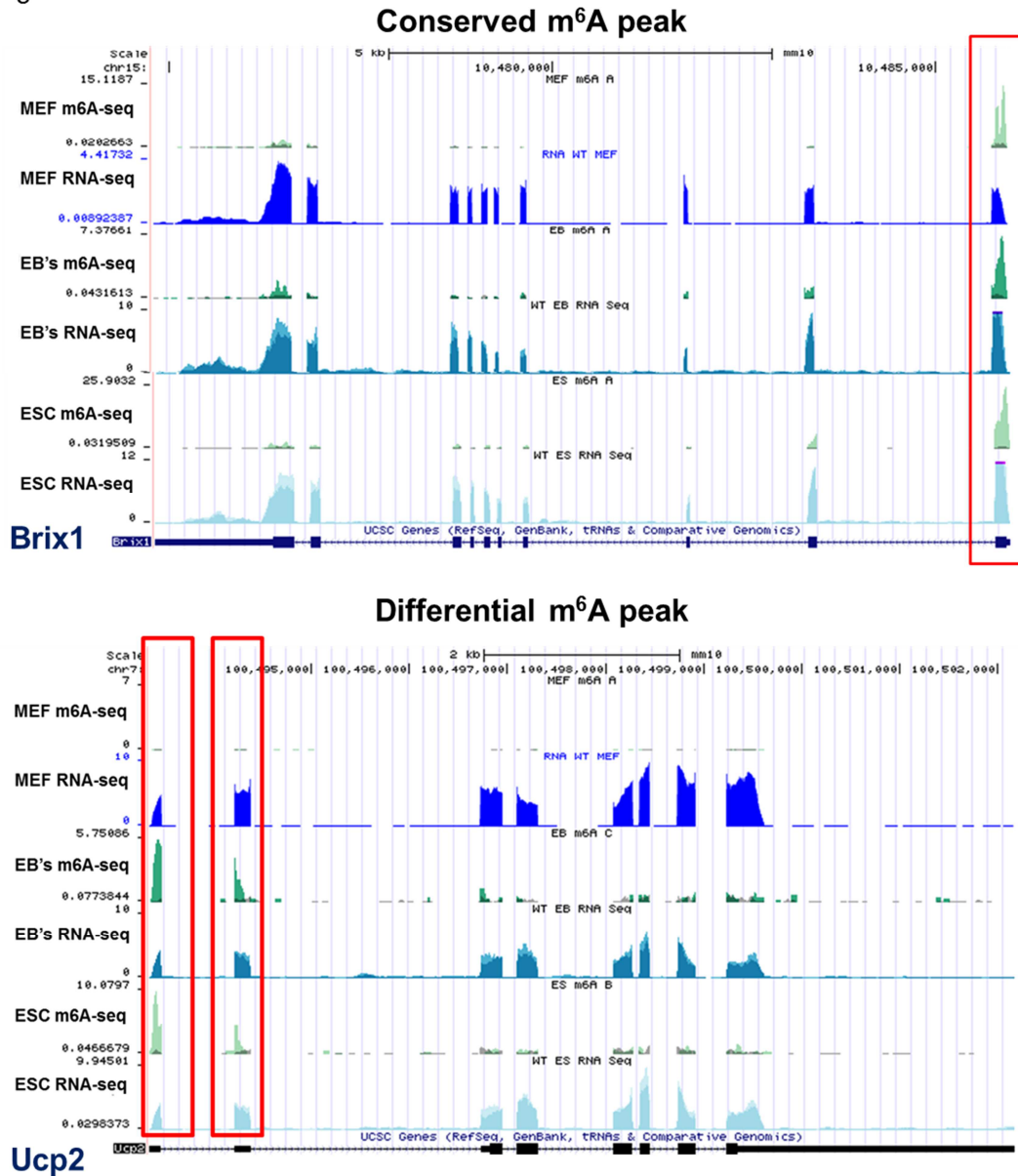


Figure 31: Characterization of differential methylation between different cell types. Examples of dynamic methylation between different cell types. In blue shades- RNA-seq data in WT ESC, EB and MEF. Green shades- m⁶A IP data in WT ESC, EB and MEF. In the upper panel: example of conserved m⁶A peak that decorate the last exon of the Brix1 transcript in all the samples. In the lower panel: an example of differential m⁶A peaks that decorate the firsts exon of Ucp2 transcripts only in the ESC and EB samples, but not in the MEF sample. Notice that the RNA-seq data shows that this gene is expressed in the same level in all the samples.

Figure 32

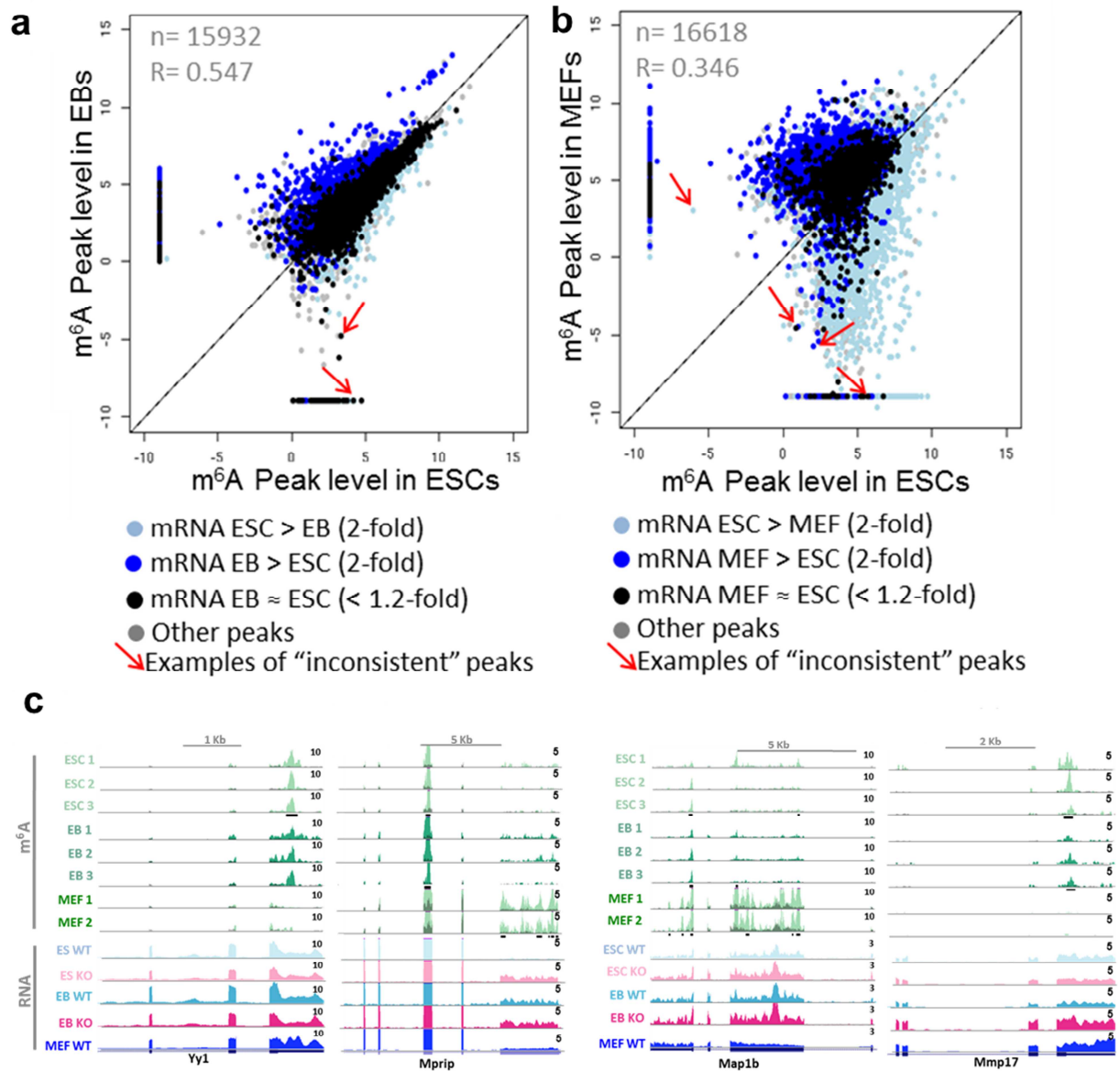


Figure 32: Characterization of differential methylation between different cell type.

a) m⁶A peak levels in ESC vs. EB. Peak levels, presented in log scale, were calculated by estimating IP coverage (RPKM) minus input coverage (RPKM) in each peak and each sample. Median was taken from triplicates. Colors indicate peaks that their normalized RNA levels (measured by RNA-Seq) are above 2 fold-change in ESC (light blue, n=733) or in EB (blue, n=1764), or peaks with similar expression level (RNA Fold-change < 1.2) in ESC and EB (black, n=5571). Pearson correlation coefficients are indicated. b) m⁶A peak levels in ESC vs. MEFs. Peaks and correlation coefficients calculated as in (a). Colors indicate peaks that their normalized RNA levels (measured by RNA-Seq) are above 2 fold-change in ESC (light blue, n=9273) or in MEFs (blue, n=2329), or peaks with similar expression level (Fold-change < 1.2) in ESC and EB (black, n=1109). c) Example of genes that have differential methylation despite similar expression levels are shown. Normalized read density (RPM) levels are shown, UCSC range is

shown at the right side of each track. Green shades – m⁶A IP in ESC, EB and MEF; Gray - m⁶A Input in ESC, EB and MEF; Blue shades – RNA-seq in WT ESC, EB and MEF; Pink shades – RNA-seq in KO ESC and EB. In m⁶A samples all replicates are shown, in RNA-seq, one of out of two replicates is shown. Significant peaks that appear in at least 2 out of 3 replicates, and at least 2-fold above input, are indicated in horizontal black squares.

Mettl3 depletion leads to specific preferential increase of mRNA levels of methylated transcripts

Our next goal was to elucidate the function of m⁶A and specifically of Mettl3 in the cell, and try to understand how does depletion of m⁶A lead to the “hyper”-naïve pluripotent phenotype we observed. Correlation assay between global expression profiles showed high similarity between WT ES, KO ES and KO EB samples, supporting the observed hyper-pluripotent phenotype (Fig. 33a). Overall a substantial number of genes had altered transcription level in the KO compared to WT (Supplementary Spreadsheet File 1), with 1487 genes significantly up-regulated and 1615 down-regulation in KO-ES compared to WT-ES, and 1503 up-regulated and 1378 down-regulated in KO-EB compared to WT-EB (consisting of 7-8% of the genes in the genome). The global effect did not have a clear trend, either up or down-regulation (Fig. 33c), however, when we looked at specific sets of genes, we found that genes that have an m⁶A peak, are significantly up regulated in KO compared to WT (Fig. 33d-e). Consistently, genes that are up regulated in KO compared to WT (>2 FC), are significantly enriched (p<10⁻¹⁷) for genes with m⁶A modification. Genes that are known targets of Ythdf2³⁹, and genes that are known targets of Mettl3 in mouse ESC³⁶, were also significantly up regulated in the KO compared to WT (Fig. 33f). Notably, the number of m⁶A peaks in a given gene positively correlated with the transcript abundance in KO compared to WT of that gene (Fig. 33d-e). The difference in ratio followed a linear trend (Fig. 33g), exhibiting an increase of ~8.8% per m⁶A peak (Pearson, r=0.995, p=3.3x10⁻⁶). Functional characterization of differentially expressed genes in KO compared to WT cells (Fig. 33c) showed that genes that are down regulated in KO EB were enriched for developmental genes (1.4 enrichment fold, FDR<0.1%), consistently with the observed functional phenotype. Genes that are up regulated in KO ESC were enriched for transcription regulation (1.75 enrichment fold, FDR<0.5%). When we looked at specific sets of genes we could see an increase in the expression of pluripotent regulatory genes in KO EB compared to WT. In a few cases, this increase happened already in ESC, e.g. Esrrb (>2.2-fold increase in KO compared to WT) and Klf4 (>2.2-fold increase). Early development genes are also highly affected from Mettl3 KO (Fig. 34a): while WT EB samples are characterized with high expression of early endodermal markers such as Foxa2, Gata4

and Gata6, in KO EB these markers are completely diminished (Fig. 34b). The results described above demonstrate that m⁶A depletion from mRNA due to Mettl3 KO positively affects mRNA levels and particularly of methylated transcripts.

Figure 33

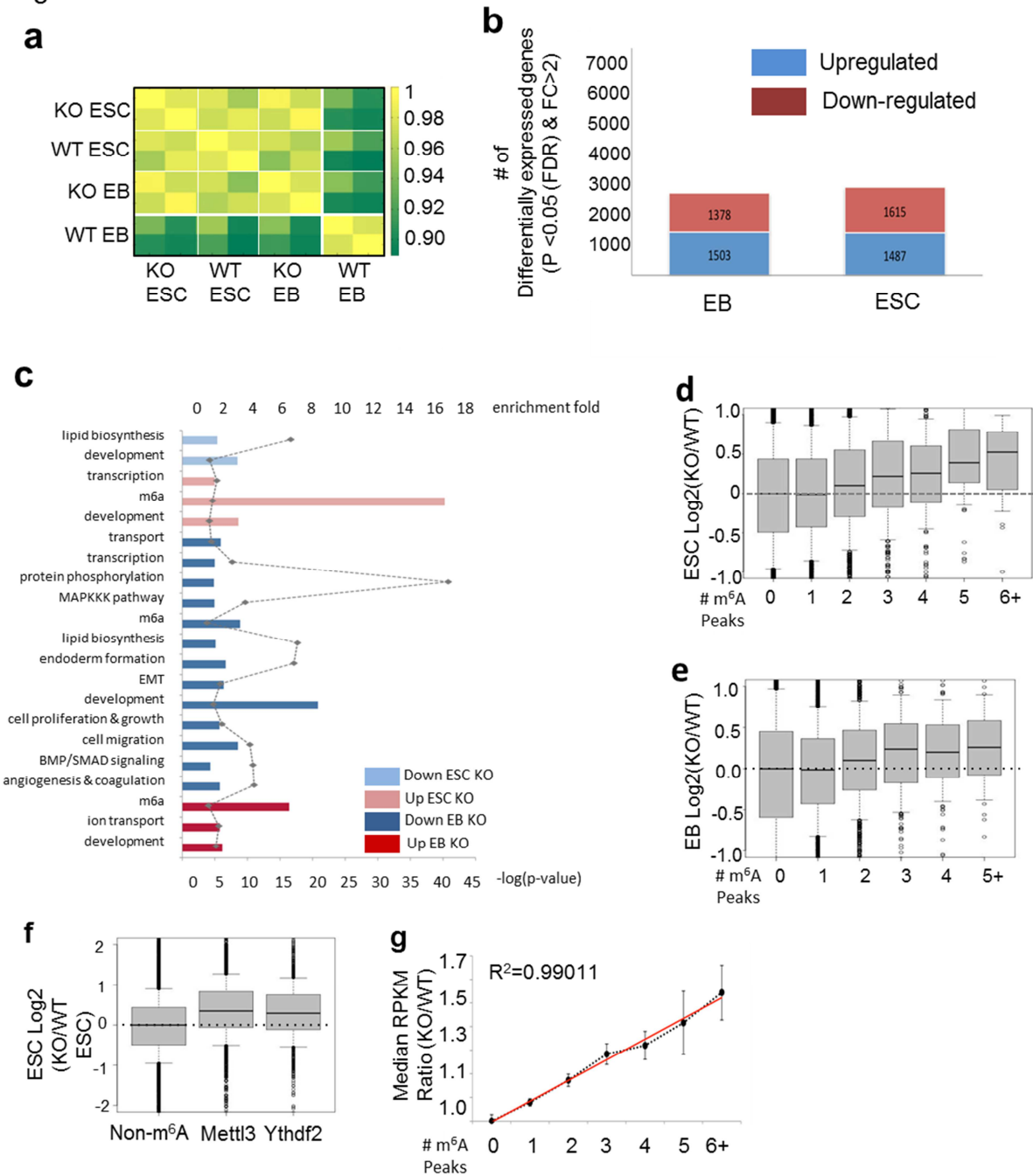


Figure 33: Characterization of Mettl3-KO transcriptional profile. **a)** Pearson correlation matrix that was calculated genome-wide between WT and KO ESC and EB samples. **b)** genes with altered transcription level (FC>2) in the KO compared to WT, with 1487 genes significantly up-regulated and 1615 down-regulation in KO-ES compared to WT-ES, and 1503 up-regulated and 1378 down-regulated in KO-EB compared to WT-EB. **c)** Functional enrichment of genes that are either up or down regulated in KO compared to WT. Genes that are down-regulated in KO EB are enriched for early development and epithelial-to-mesenchymal-transformation. Genes that are up-regulated in KO ESC and EB are enriched for m⁶A-decorated genes. Bars represent Fisher exact test $-\log(p\text{-value})$, dotted line represent enrichment fold-change **d-e)** Transcriptional change in KO ESC compared to WT ESC (**d**) or KO EB compared to WT EB (**e**), as a function of the number of m⁶A peaks found in each transcript. Transcription upregulation in Mettl3-KO increases with the number of m⁶A peaks. Box plots describe the distribution of fold-change; medians are indicated in the center of the boxes. **f)** Transcriptional change in KO ESC compared to WT ESC, of targets of Ythdf2(39) and targets of Mettl3(36). **g)** Expression levels of Mettl3 KO/WT ESC, increased as a function of the number of m⁶A peaks/transcript (ANOVA, $p=1.86 \times 10^{-7}$) in a relatively linear trend, rising by $\sim 8.8\%$ in the KO ESC per m⁶A peak in (Pearson $r=.995$, $p=3.3 \times 10^{-6}$) (16, 19).

Figure 34

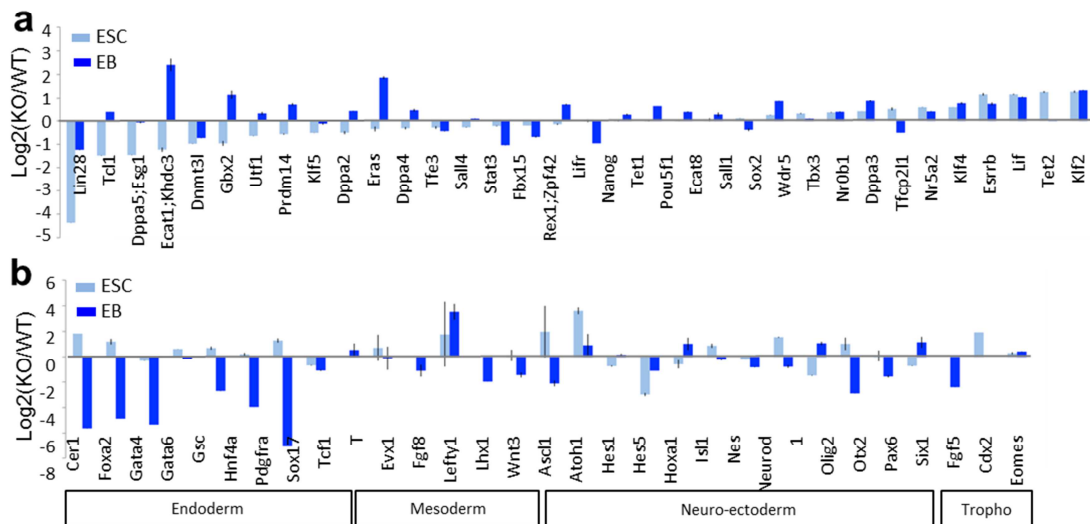


Figure 34: Characterization of Mettl3-KO transcriptional profile. **a-b)** Expression change in KO vs. WT of ESC (light blue) and EB (blue), presented as log-ratio, of selected pluripotency genes (**a**) and early developmental genes (**b**).

m⁶A positively effects the degradation rate of methylated mRNAs

Changes in mRNA levels reflect the difference between transcription and degradation rates; thus, any modulation of one or both of these processes will result in altered RNA level. Previous studies showed that m⁶A has a role in mRNA degradation; Specifically, Ythdf2 binds to m⁶A modifications and delivers the mRNA molecules to P-bodies where they are processed and degraded³⁹. To measure mRNA degradation rates independently from transcription rates, mRNA levels were monitored at times 0, 4 and 8 hours after transcription inhibition with Actinomycin D³⁶, using 3' DGE (digital gene expression) method followed by deep sequencing (Fig. 35). We then calculated degradation rate and half-life of each transcript (See Methods). Interestingly, the half-life of genes that carry m⁶A modification is significantly shorter than genes that do not carry m⁶A modification ($p < 3 \times 10^{-6}$ and $p < 0.005$ in ESC and EB respectively, Fig. 35b). Subsequently, in Mettl3-KO, the half-life of these genes is significantly longer ($p < 2 \times 10^{-16}$ in ESC and EB, Fig. 35c). In non-m⁶A genes, the half-life is also longer but to a lesser extent ($p < 0.003$ in ESC, Fig. 35c). Upon Mettl3 KO, an increase in the half-life of genes normally methylated in WT ESC was observed, regardless of the location of the m⁶A peak (Fig. 36a). Importantly, pluripotent gene transcripts also showed a significantly increased half-life that was prominent in KO EB samples (Fig. 35d and Fig. 36b-c). Previously identified mRNA bound targets of Ythdf2 also showed a significant increase in half-life, in accordance with the role of Ythdf2 (Fig. 35e). qPCR based transcript half-life with and without Actinomycin D treatment, validated increased half-life (>2 fold-change) for Klf4, Nanog and Sox2, but not for Oct4 and Mta2 whose transcripts are not methylated (used as negative controls, Fig. 35f).

Our findings suggest that the "hyper-pluripotent" phenotype induced by Mettl3 ablation results, at least in part, from increased stability of methylated pluripotent gene mRNA transcripts.

Figure 35

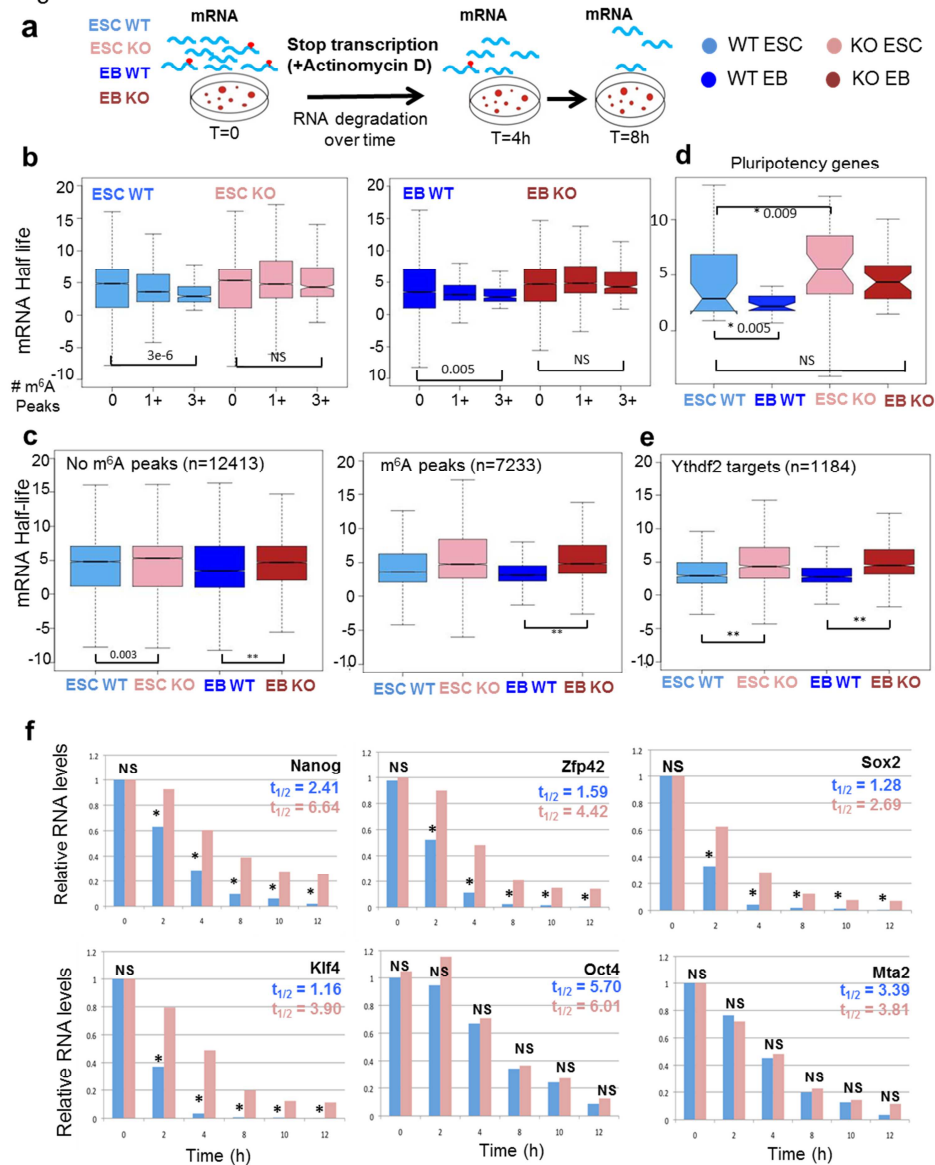


Figure 35: The effect of m⁶A depletion on mRNA degradation. **a)** mRNA levels were monitored at times 0, 4 and 8 hours after transcription inhibition with Actinomycin D, using 3' DGE (digital gene expression) method followed by deep sequencing. **b)** Distribution of transcripts half-life in ESC (left), EB (right), each for WT (blue shades) and KO (pink/red). Distributions are shown for genes without m⁶A (n=12461), genes with at least one m⁶A peak in either condition (n=7181), and genes with at least 3 peaks (n=427). The genes with 3 peaks or more have a significantly shorter half-life than the genes without m⁶A peaks (Wilcoxon *P*-values are indicated). **c)** Distribution of transcripts half-life of genes without m⁶A (left) and genes with m⁶A (right), as measured in ESC and EB, each for WT (blue shades) and KO (pink/red). Half-life of m⁶A genes is significantly longer in Mettl3-KO compared to WT, both in ESC and EB (Wilcoxon *p*-value <2⁻¹⁶). **d)** Distribution of transcripts half-life of naive pluripotency genes, as

measured in ESC and EB, each for WT (blue shades) and KO (pink/red). Half -life is significantly longer in Mettl3-KO compared to WT, both in ESC and EB, and in WT ESC compared to WT EB. **e**) Same as **(c)** for Ythdf2 targets. Here too, half-life of Ythdf2 targets is significantly longer in Mettl3-KO compared to WT, both in ESC and EB (Wilcoxon p -value $<2^{-16}$). **f**) Relative expression level of 6 genes, measured by qPCR, during 12 hours after Actinomycin-D treatment as indicated in the scheme. Transcriptional levels were measured both in WT (blue) and KO (pink), showing a reduction in degradation rate of m⁶A-decorated genes in KO compared to WT. This reduction is reflected in longer half-life (indicated numbers) in KO compared to WT. * Indicates p value <0.05 . NS – not statistically significant. One representative experiments is shown of 3 independent biological replicates performed.

Figure 36

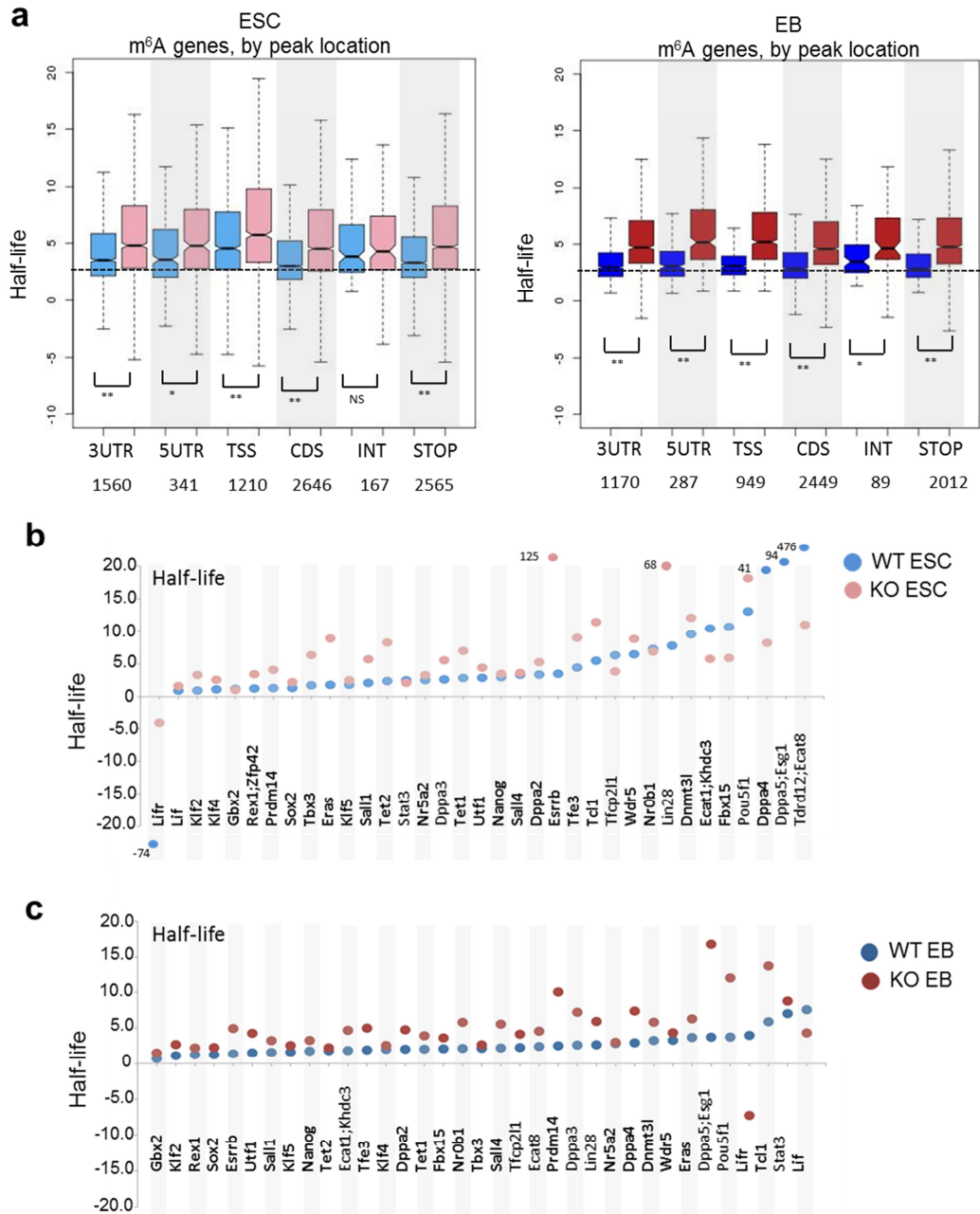


Figure 36: The effect of m⁶A depletion on mRNA degradation. **a)** Distribution of transcript half-life, of m⁶A-carrying genes, as a function of the m⁶A peak location, showing that in all locations but intronic peaks, the half-life is significantly longer (Wilcoxon p-value < 2⁻¹⁶) in ESC KO compared to ESC WT, and similarly in EB. **b-c)** Half-life (in hours) of naive pluripotency genes, measured in ESC (**b**) and EB (**c**), each for WT (blue shades) and KO (pink/red). Methylated genes are marked with bold font.

m⁶A mildly represses translation efficiency

The fact that m⁶A peaks over-populate the stop codon vicinity^{24,33}, suggests that m⁶A may affect translation. Early studies had conflicting results on the positive or negative effect of m⁶A on translation⁷³⁻⁷⁵. However such studies were confounded by lack of exacting genetic perturbations or looking at individual transcripts. Thus, we evaluated the global effect of m⁶A on translation in our system. Actively translated transcripts are found in the polysomal fraction, which can be isolated by sucrose gradient. Profiles of polysomes isolated from WT and KO ESC and separated on sucrose gradient (Fig. 37a) indicated a mild increase in translation efficiency upon m⁶A depletion as evident by decrease in the translatable mRNA pool (associated with 40S-80S subunits). To validate this and correlate with m⁶A abundance, we measured translation topology at high-resolution in WT and KO ESC and EB, by using ribosomal foot printing profiling assay (Ribo-seq)^{54,55}. Global similarity in the overall polysome-bound Ribo-seq profiles between the different cells and conditions revalidated the similarity of both ESC and EB KO samples to the WT ESC, differing from the WT EB (Fig. 37b). To identify if differences in translation correlated with m⁶A abundance, we calculated translation efficiency (TE), which is the normalized translation (RPM) in the coding sequence, divided by the normalized transcription (RPM) of the same interval⁵⁴. Remarkably, when we analyzed the TE in KO compared to WT ESC we found that m⁶A methylated genes show a modest yet significantly increased TE in KO compared to WT (p<0.017) (Fig. 37c). Such increase was not observed in unmethylated genes. To further validate the previous result, we also calculated the ribosome release score (RRS), which is the ratio between the total number of reads within the coding region and the total number of reads within the 3' UTR obtained in the Ribo-Seq, divided by the same ratio obtained from the mRNA-Seq⁵⁷. The RRS ratios between KO and WT ESC increased significantly between methylated and unmethylated genes ((Fig. 38a-b ANOVA, P=0.0001), and it changed as a function of the number of m⁶A peaks, with an increase of ~11.9% per m⁶A peak (Pearson r=0.953, P<0.05, Supplementary Fig. 38a-b). The RRS was increased in KO compared to WT, regardless of whether the m⁶A peaks is located around the stop codon (Fig. 38b). Finally, we measured protein expression profile of WT and KO ESC and EB using stable isotope labeling by amino acids in cell culture (SILAC)⁵⁸. Overall,

like with transcription and translation, WT and KO ESC profiles cluster together with KO EB, while WT EB are significantly different (Fig. 37d). A significant increase was observed in SILAC ratios between KO and WT ESC as a function of the number of m⁶A peaks (ANOVA, P=1.29 x 10⁻⁹). The difference in KO/WT ESC ratio show an increase of ~11.3% per m⁶A peak (Pearson r=.996, P=0.0002) (Fig. 38c). In summary, absence of m⁶A leads to increased RNA stability and translation efficiency of m⁶A-decorated genes, including prominent naïve pluripotency regulators that stabilize the state and shield its' responsiveness to lineage priming cues.

Effect of m⁶A methylation on alternative splicing and A-I RNA editing

m⁶A is more likely to be found in introns and exons that undergo alternative splicing^{24,33}, therefore we aimed to also globally evaluate mRNA alternative splicing in our system. To detect m⁶A-dependent differential alternative splicing events in our system, we looked for events of alternative splicing between KO and WT ESC and EB, by using MATS software⁵⁹. We found 1269 alternative splicing events in ESC and 720 in EB, compared to only 134 in the control experiment (Fig. 39a-b, Supplementary Spreadsheet, Geula et al). While 5 types of alternative splicing were tested, 2 of them, which are skipped exons and retained introns (in which the intron is included in the mature transcript) were the most frequent. Interestingly, the direction of the events was not random (Fig. 39c): In 84.5% of skipped exon events, the exon was more included in the WT and excluded in the KO. In 89.5% of retained intron events, the intron was more included in the KO and excluded in the WT. To test whether the alternative splicing events are a direct effect of lack of m⁶A, we estimated how significant the overlap between alternative splicing sites and m⁶A sites is. We found that although splicing events overall are rare (in less than 1% of the exons), the percentage of exons with alternative splicing event is significantly higher among exons that also have m⁶A peak, compared to exons without m⁶A peak (Fig. 39d). In addition, the alternative splicing events (skipped exons and retained introns) tend to appear in long exons (Fig. 39e). These results suggest that indeed there is a direct effect of Mettl3 depletion on alternative

splicing with a tendency to occur on long exons. The exact molecular mechanism by which this occurs, and how this could contribute to pluripotency mis-regulation is of future scientific interest.

Finally, we investigated the effect of m⁶A on RNA A-I editing catalyzed by ADAR (Adenosine Deaminase Acting on RNA) family enzymes, which acts on double stranded RNA⁷⁶ and can lead to protein diversification⁷⁷. We used two approaches in order to look for differential A-I editing in WT and Mettl3 KO. First, we looked at about 9,039 sites that are known to undergo editing, and compared their editing levels. In addition, we measured the global editing activity of ADARs (see methods). In both approaches (Fig. 40 a-b), we noticed a decrease in A-I editing in KO conditions compared to WT: The number of Hyper-edited sites (on average) was reduced by 1.7 fold in KO ESC, and by 1.5 in KO EB compared to the matched WT samples. Similarly, the percentage of known sites with more than 50% editing level was reduced by 1.3 in KO ESC and by 1.4 in KO EB. However this effect did not correlate with m⁶A methylation localization, suggesting a likely indirect secondary effect.

Mettl3 is a study case for how different epigenetic repressors have a divergent effect on naïve vs. primed murine PSCs

Our results show the divergent dependence on Mettl3 to maintain naïve vs. primed pluripotent states. We wondered if like Mettl3, other transcriptional and epigenetic repressors might also have such an opposing effect on naïve vs. primed pluripotent cells. We aimed to conduct a focused RNAi screen targeting transcriptional and epigenetic regulators previously implicated in pluripotency regulation. We derived knock-in Oct4-GFP^{+/+} Naïve ESC and EpiSC lines from E3.5 and E6.5 C57BL/6 mouse embryos, respectively, and conducted a targeted and selective siRNA screen for ~30 factors, in search for those that specifically perturb maintenance of the primed, but not the naïve, pluripotent state (Fig. 41a). Factors like Oct4 and Wdr5 were expectedly essential in both pluripotent states, and acute depletion of Nanog or Klf5 compromised the naïve pluripotent state, but not primed cells as the latter cells express residual levels of these factors and do not rely on them for naïve pluripotency maintenance. Remarkably, we noted a number of chromatin repressors that specifically down-regulated Oct4-GFP

detection and resulted in differentiation of primed cells only – most prominently both Polycomb components Eed and Suz12, Rest and Mbd3 co-repressors, maintenance methyltransferase Dnmt1 and Mettl3 (Fig. 41b). Our results highlight the important need to distinguish between different pluripotent states, because different regulators like DNA and RNA methyltransferase enzymes, can have drastically different influence on distinct pluripotent configurations. It is of importance to note that so far we are not aware of successful attempts to expand DNMT1 or METTL3 KO human ESCs, probably because conventional hESCs are closer to the primed state rather than the naïve state.

Figure 37

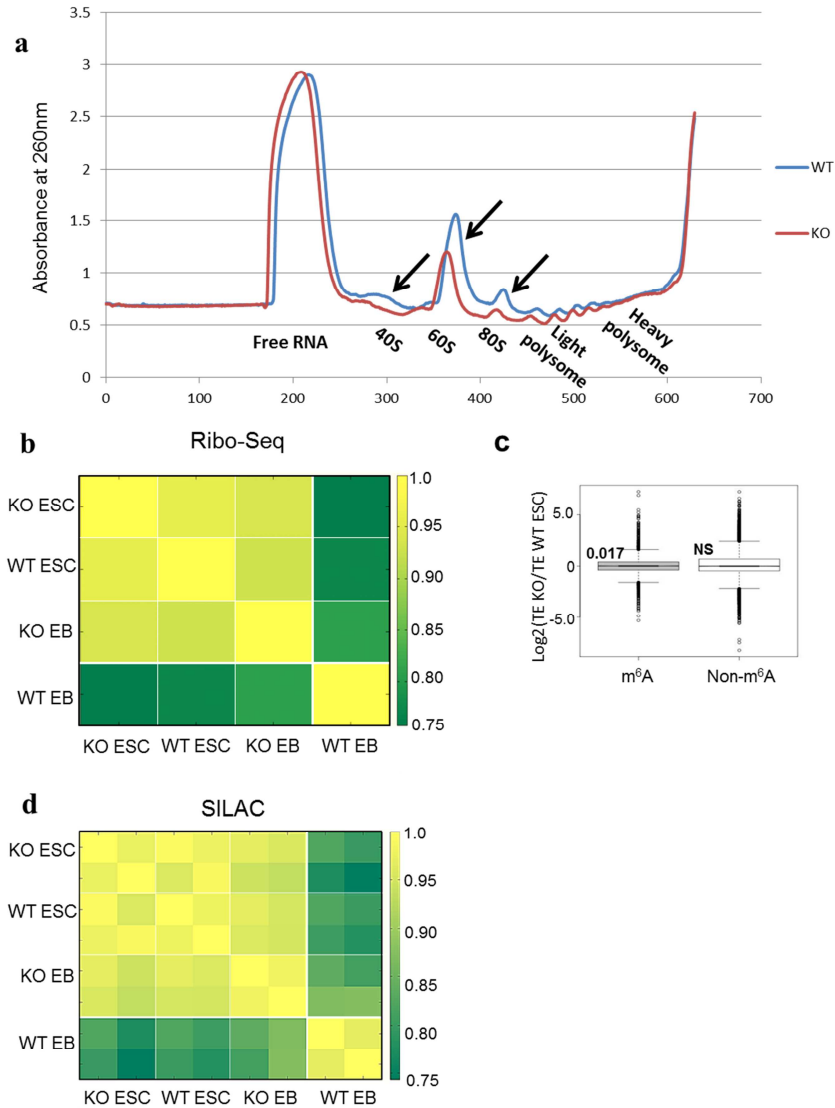


Figure 37: Mettl3-KO effect on translation. **a)** Ribosome profiling of WT and Mettl3 KO ESC revealed a slight yet reproducible decrease in the 80S ribosomal fraction in KO ESCs (1 out of 2 representative experiments is shown). **b)** Ribo-Seq profiles of WT and Mettl3 KO ESC and EB were determined and compared. Global similarity in the overall polysome-bound Ribo-Seq profiles exhibited high similarity between Mettl3 KO ESC and EB and WT ESC, differing from the WT EB. **c)** Change in Translation efficiency in KO compared to WT ESC, showing a significant slight increase (t-test P-value<0.017) in translation efficiency of m⁶A-carrying genes. **d)** Protein profiles of WT and Mettl3 KO ESC and EB were determined in duplicates using SILAC. Global similarity between protein profiles re-exhibited the similarity shown in b. showing the WT and KO ESC and KO ESC are highly similar, differing from WT EB.

Figure 38

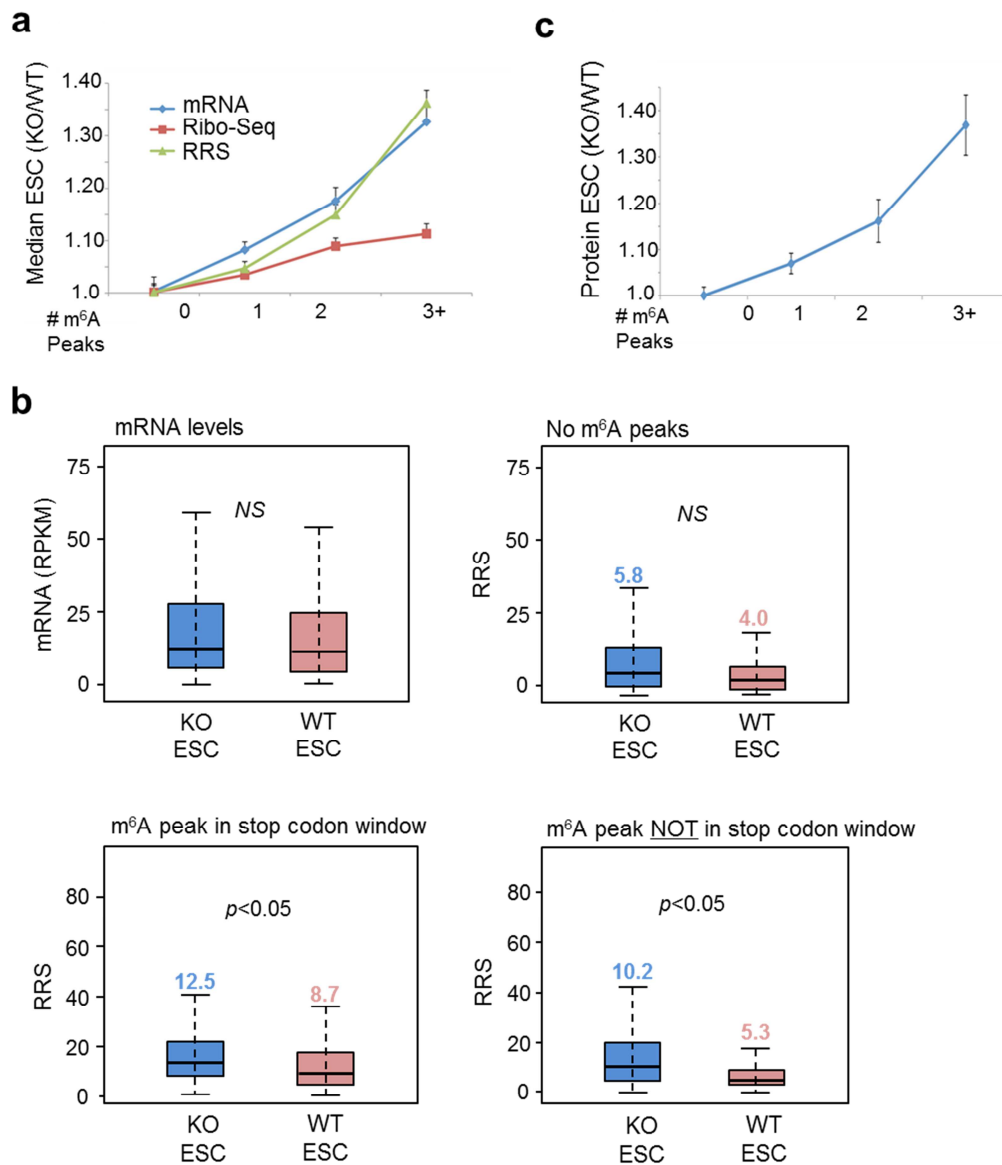


Figure 38: Mettl3-KO effect on translation. **a)** mRNA, Ribo-Seq and RRS WT/KO ratios were divided into groups of increasing number of peaks/gene transcript. The median ratio values in each group was calculated and normalized to the median ratio of non-methylated genes. All three parameters increased with the increase in peak number/gene. **b)** Median RRS values were calculated from Ribo-Seq and mRNA-Seq data of WT and Mettl3 KO ESC, for non-methylated genes, genes containing m⁶A in stop codon window and genes having m⁶A peak not in locations other than the stop codon window, compared to mRNA levels. Significant differences in RRSs were observed for genes with m⁶A peaks regardless of their location relative to the stop codon window. t-test p < 0.05. **c)** Protein intensity ratios determined by SILAC in groups of genes having increasing number of peaks/gene. Normalized ratios determined by SILAC increased with the number of peaks per gene demonstrating an effect of m⁶A on protein levels.

Figure 39

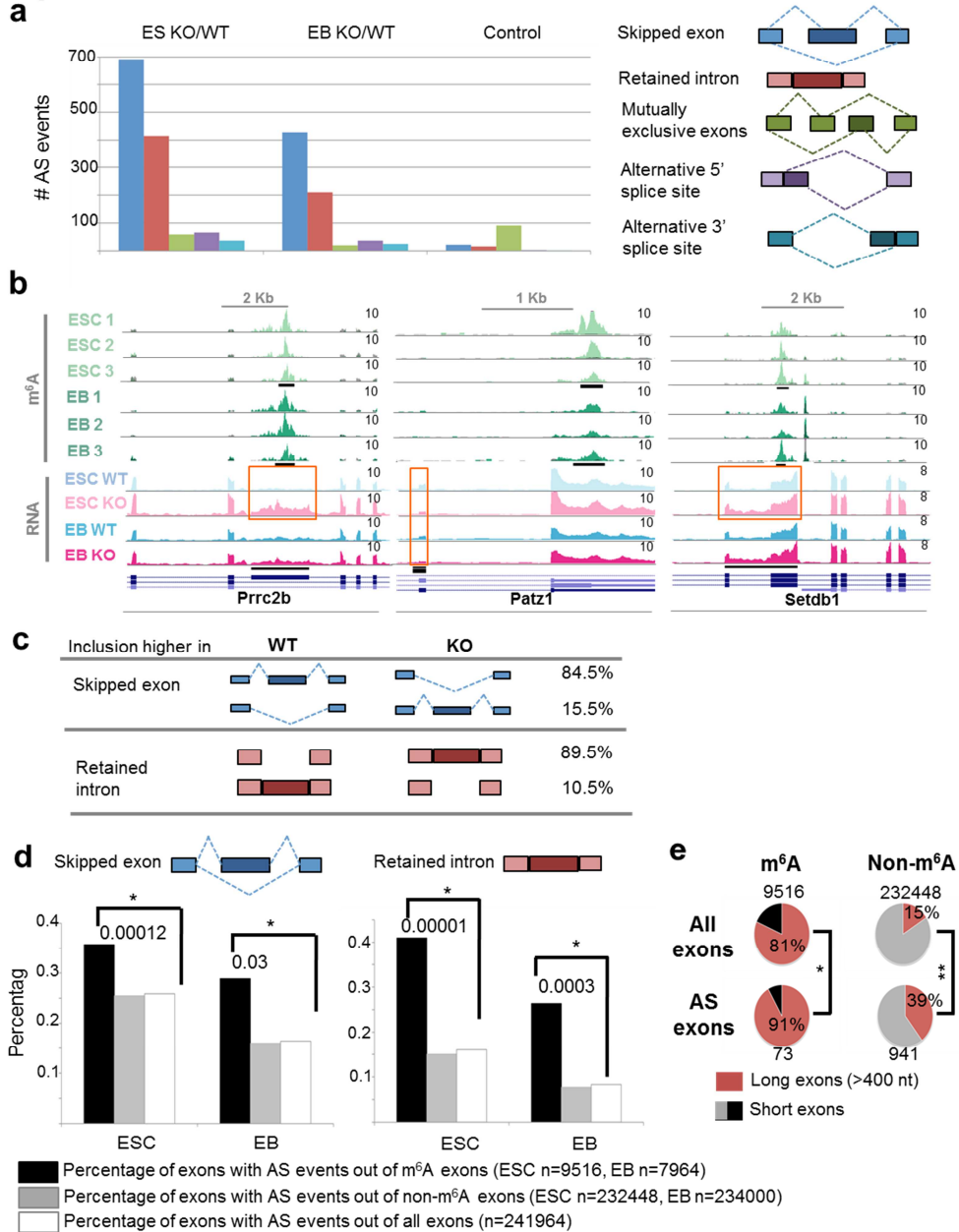


Figure 39: Mettl3-KO affects alternative splicing. **a**) Number of alternative splicing events in KO vs. WT ESC and EB and in Control. Each subplot presents the number of splicing events that are different between two conditions. Blue – skipped exon, red – retained intron, green – mutually exclusive exons, purple – Alternative 5SS, teal – Alternative 3SS. **b**) Selected examples of splicing events, which are different in KO and WT: skipped exons (Prrc2b, Patz1) and retained intron (Setdb1). Colors as in **Figure 30**. **c**) Inclusion levels of skipped exon and retained intron show a non-random inclusion, where skipped exons tend to be excluded in KO, and introns tend to be retained in KO, suggesting that m⁶A may increase splicing efficiency of un-favored splicing events. **d**) Overlap between alternative-splicing events and either exons with m⁶A modification

(black), or exons without m⁶A modification (gray). The overlap with m⁶A exons is very small (<1%), but significant (Fisher exact test p-values are indicated) compared to background exon population. **e**) Percentage of long exons (>400 nt, red) out of all exons, or exons that are part of alternative splicing (AS) event, divided to m⁶A exons (left) and non-m⁶A exons (right). AS exons are enriched for long exons, both in m⁶A exons (91% compared to 81%, Fisher exact test p<0.012) and in non-m⁶A exons (39% compared to 15%, Fisher exact test p<5.1⁻⁶⁸).

Figure 40

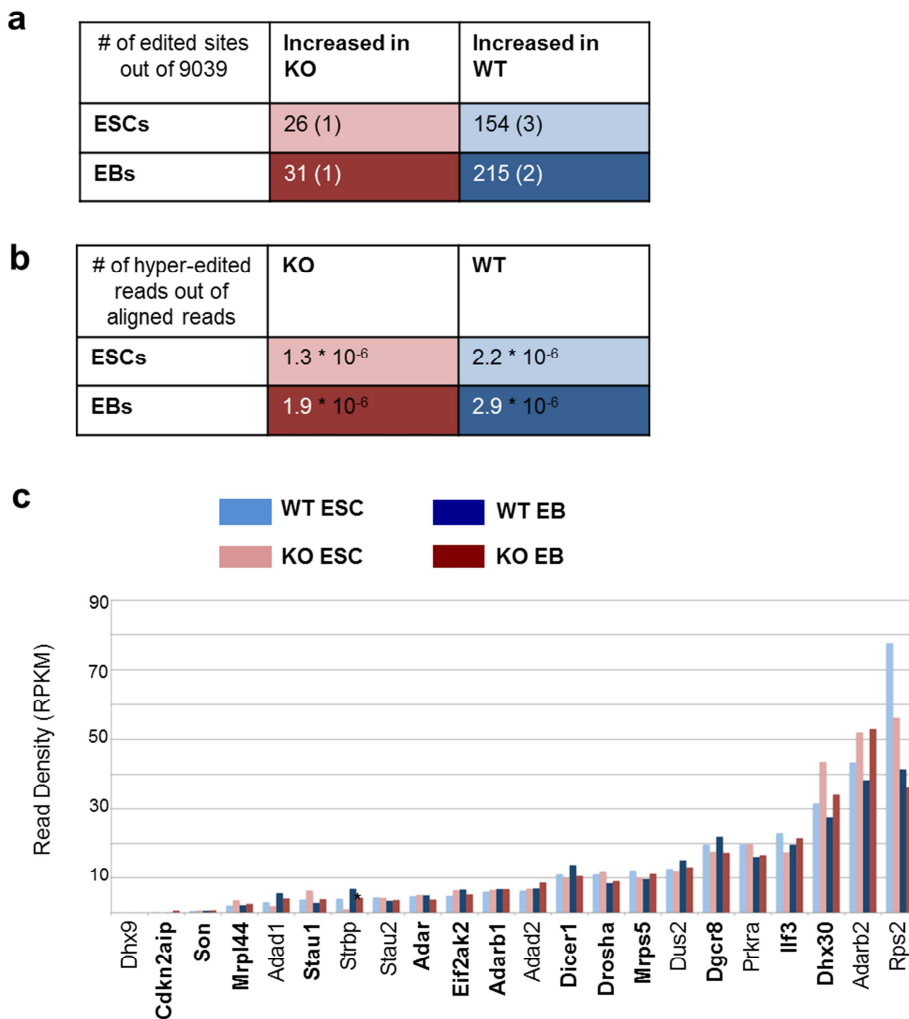


Figure 40: Mettl3-KO affects RNA editing. We used two approaches in order to look for differential A-I editing in WT and Mettl3 KO. First, we looked at about 9,039 sites that are known to undergo editing, and compared their editing levels. In addition, we measured the global editing activity of ADARs (see methods). **a**) Number of edited sites, out of 9,039 known edited sites, which are up or down-edited in KO vs. WT, ESC and EB. These sites have a low overlap with m⁶A peaks (numbers are indicated). **b**) Number of Hyper-edited reads in the different conditions. In both approaches (**a**, **b**) we noticed a decrease in A-I editing in KO conditions compared to WT: The number of Hyper-edited sites (in average) was reduced by 1.7 fold in KO ESC, and by 1.5 in KO EB compared to the matched WT samples. Similarly, the percentage of known sites with more than 50% editing level was reduced by 1.3 in KO ESC and by 1.4 in KO EB. **c**) Expression levels (RPKM) of editing-related genes (dsRNA binding proteins) in the 4 conditions. Genes that carry m⁶A peaks are bold.

Figure 41

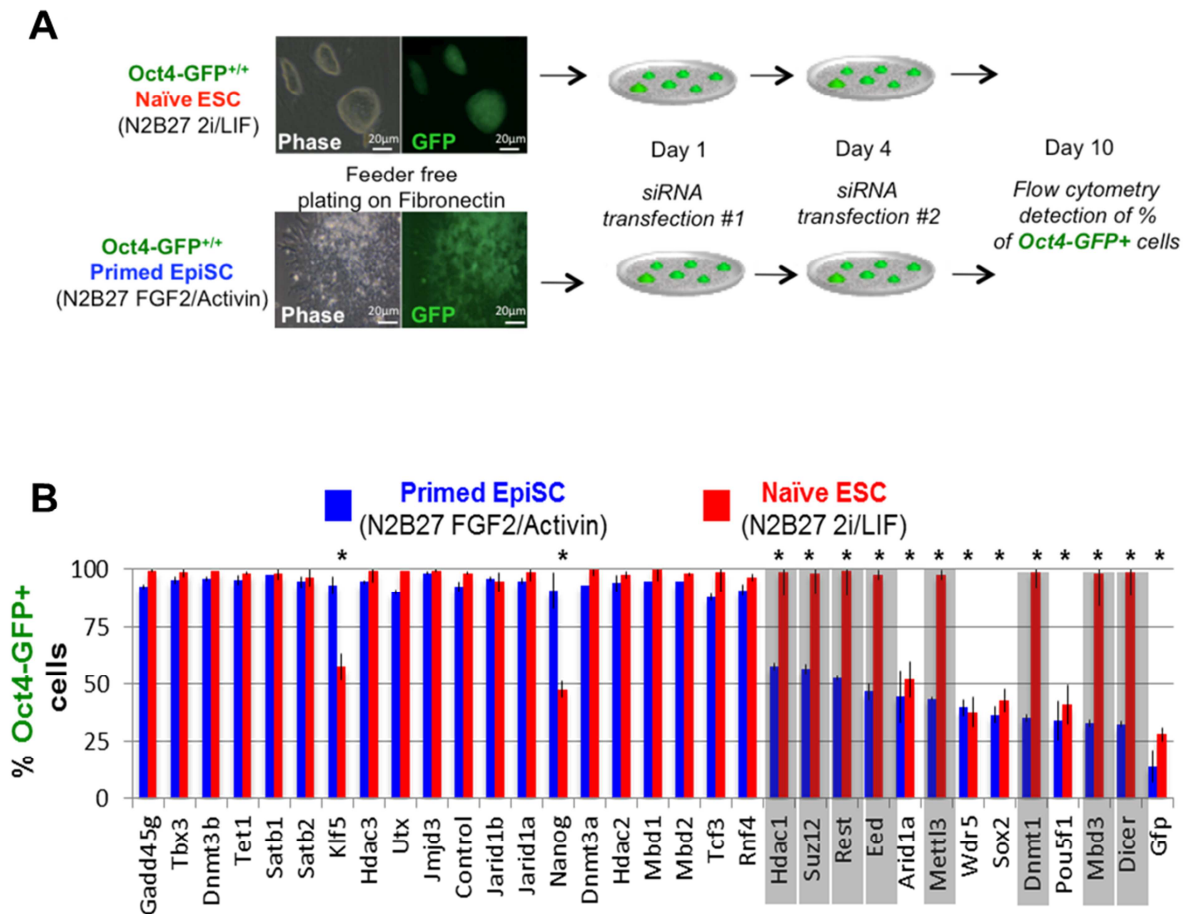


Figure 41: different chromatin repressor has a divergent effect on naïve and primed murine PSCs. a) Targeted siRNA screen for regulators that differentially stabilize mouse naïve or primed pluripotent cells. Naïve Oct4-GFP+ cells or epiblast derived Oct4-GFP+ primed cells were transfected with the indicated validated siRNAs and analyzed after 10 days by FACS for Oct4-GFP levels. Error bars indicate s.d. (n=3). * Indicates t-test p value < 0.05 relative to matched siRNA control. Gray shades highlight genes specifically perturbing the primed, but not naïve, murine pluripotent state.

Discussion

m⁶A RNA methylation and the decay of naïve pluripotency program

The findings reported herein highlight m⁶A mRNA methylation as a critical regulation layer, acting during termination of murine naïve pluripotency to safeguard an efficient, timely and authentic down-regulation of naïve pluripotency network. m⁶A modify and destabilize many of the naïve pluripotent transcripts (Fig. 27, Fig. 29, Fig. 35 and Fig. 36). This down-regulation is critical for adequate exiting the naïve state and proper establishment of the primed pluripotent state and endowing it with competence to response to developmental cues and undergoes lineage priming at the post-implantation stage. Knockout of *Mettl3* and the subsequent major depletion of m⁶A, results in developmental failure at the early post-implantation stages (Fig.18-24), and not the pre-implantation pluripotent epiblast (Fig. 2-3). Thus emphasizing the fact that m⁶A is dispensable for establishing the naïve ground state of pluripotency, and is rather important for terminating that state. These results underscore the dramatic importance of m⁶A in early mammalian embryogenesis and pluripotency transitions.

The fact that most of naïve-pluripotency promoting genes are methylated (Supplementary Table S3) and previous evidences that m⁶A affects mRNA degradation^{36,39}, led us to evaluate that in *Mettl3*-KO in the context of pluripotent cells. M⁶A marked naïve pluripotency gene transcripts are indeed not degraded at the expected kinetics. Since these genes are highly expressed in the naïve state, increased stabilization of their mRNA molecules prevents the “cellular developmental program” to overtake their place, which leads to the exaggerated or “hyper-pluripotent” phenotype that was observed both in-vivo and in-vitro (Fig. 42). However it is important to highlight that m⁶A does not exclusively mark pluripotency genes, and regulates other networks in ESCs and in other cell types. However, as most of bona fide naïve pluripotency genes are targeted by *Mettl3*, this leads to amplification and over-stabilization of the most dominant transcriptional circuit in the ground state of pluripotency (Fig. 16 – upper panel, Fig. 35 and Fig. 36).

In normally established wild-type EpiSCs, naïve pluripotency genes typically carrying m⁶A are down regulated. Simultaneously, m⁶A labeled lineage priming gene transcripts (e.g. *Foxa2*, *Sox17*, Fig.28b) are naturally upregulated in the primed pluripotent state (Fig. 16). Thus, the outcome of *Mettl3* depletion has an opposite effect on naïve and primed states (Fig .15 and Fig. 16– lower panel), because in primed cells the differentiation priming genes are expressed at much higher levels, and their further boosting following *Mettl3* depletion pushes the cells above a critical threshold toward differentiation (Fig. 42) The latter occurs despite the accompanying slight increase in the weakly expressed pluripotency genes in primed pluripotent cells upon *Mettl3* depletion. Notably, it will be of interest to analyze *in vivo* developmental phenotype where *Mettl3* is specifically depleted only after implantation. In summary, the outcome of the pluripotency (de)stabilization can change between media conditions depending on the pluripotent state they promote and maintain (naïve vs. primed). A recent independent study by Prof. Howard Chang group (Stanford) ⁷⁸ that also analyzed KO of *Mettl3* in mouse ESC reached similar conclusions.

Figure 42

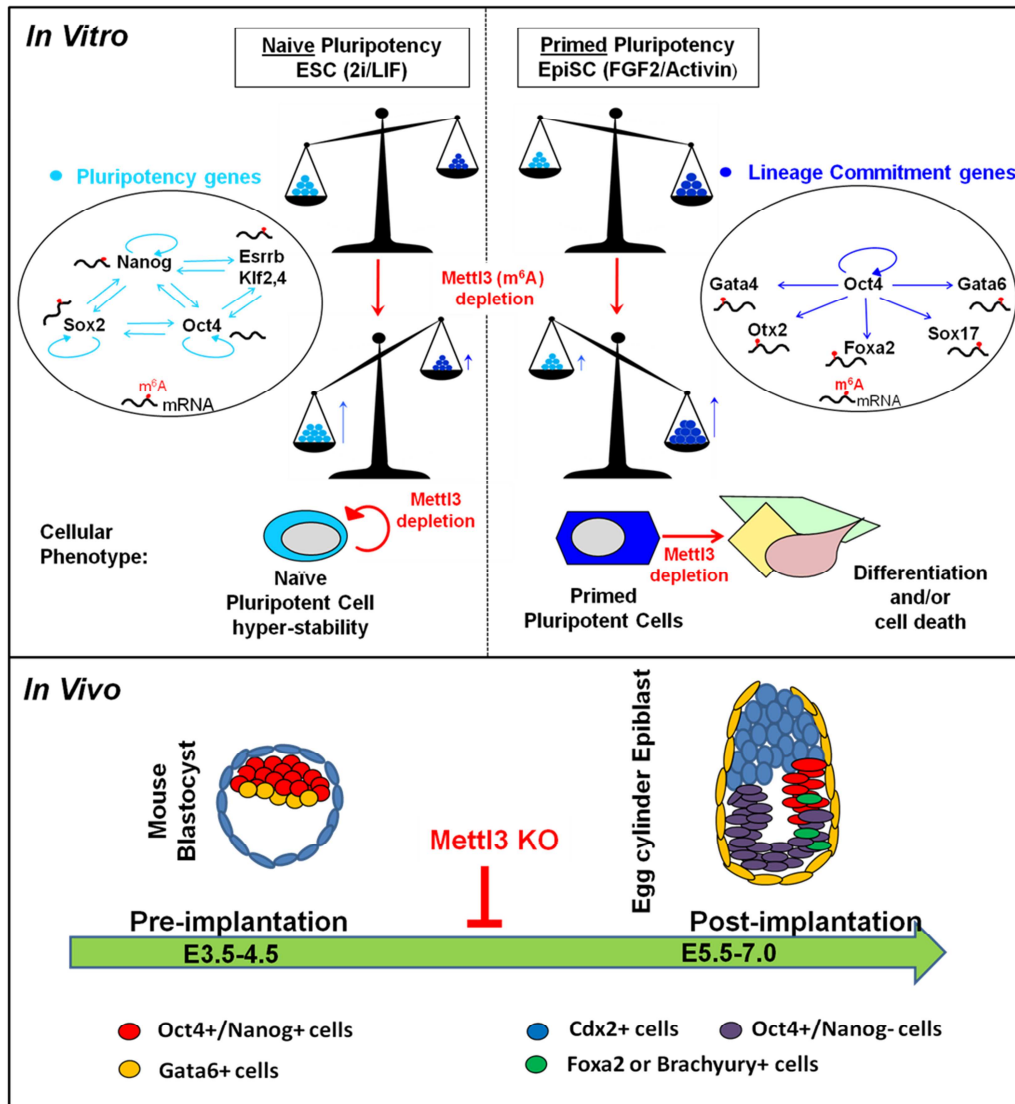


Figure 42: Summarizing model. m⁶A marked mRNA transcripts (blue) are decorated with a red circle. See discussion for detailed explanations and summary.

Direct and indirect regulatory effects for m⁶A on mRNA

Our results point to a dramatic effect for Mettl3 ablation on mRNA degradation rate (Fig. 33-36). However, this perturbation has also a significant effect on other aspects of mRNA processing and function in the cell. We showed that mRNA translation efficiency is slightly, yet significantly, higher in Mettl3-KO cells as shown by two different statistical methods (Fig. 37-38). Alternative splicing is also directly affected in our model system by the presence of m⁶A methylation in the spliced region (Fig. 39). In both cases of translation and splicing, the exact mechanism by which m⁶A has an effect is yet to be revealed. This is also the case with RNA editing. The effect of Mettl3-KO on editing is profound (Fig. 40). In fact, as far as we know, this is the largest reduce of editing activity, caused by manipulation of a non-ADAR genes. Unlike the case of translation and splicing, here the overlap between m⁶A peak and edited sites is very low, thus indicating that the effect is like to be indirect. For instance, the latter may be due to a change in the expression of a double-strand binding protein or ADAR family member, whose expression is perturbed by depletion of m⁶A, or by changing in mRNA secondary structure do to the depletion of m⁶A.

Our findings may set the stage for dissecting the role of m⁶A in regulating other programming and reprogramming developmental events *in vivo*, and to thoroughly explore other potential regulatory roles for m⁶A in regulating gene expression. This may include influencing secondary RNA structure or localization. It will also be of future interest to contrast the developmental potency phenotypes in mice and pluripotent cells deficient for different combinations of m⁶A readers including Ytfdh1, 2,3 and Elavl1. The latter follow-up studies should also test the hypothesis whether distinct influences on different aspects RNA metabolism and processing are dictated by specific readers, and/or whether mRNA target specificity exists for such readers. The fact that murine naive pluripotent cells seem stable to such drastic perturbation in m⁶A regulators, is likely to render them as a key platform for allowing such in depth mechanistic studies. As such, our study has emphasized the ability to recapitulate to satisfying extent *in vivo* developmental phenotypes related to m⁶A perturbations in multiple in-vitro systems,

including embryoid bodies formation, teratoma assays and directed differentiation in the petri dish.

m⁶A as a dynamic modification between different cells state

The fact that m⁶A mRNA modification is process by a large methyltransferase complex that only several members in it identify (Mettl3, Mettl14), and the fact that until now two different m⁶A demethylation enzyme also have been identify in mammalian cells, suggest that this modification have a dynamic nature. We tested this dynamic between different cells state, in Pluripotent naïve mESC, in early differentiated cells- EB and in somatic cells –MEF. It is critical to understand that m⁶A modification is occurring only on expressed RNA. And even if it expressed we cannot map all of it duo to detection limitation in low expressed RNA. Therefore, when we looking for differential m⁶A methylation site we need to compare between transcripts that have similar expression level between the different samples. When we look at this dynamic we can see that overall, most peaks in ESC and EB were correlated. However, there were 232 peaks mapped to 211 genes, in which the change in m⁶A methylation was not consistent with the change in expression. When comparing ESC to MEF, we observed lower correlation and identified 1223 peaks mapped to 916 genes, of differential methylation that is not consistent with the change in expression. (Fig. 31-32). These finding suggest a dynamic regulation, in the methyltransferase process or the demethylation process, on m⁶A modification between different cell types. It will be interesting to study how this differential modified gene change their stability or translation efficiency in different cells type relatively to their methylation status.

Opposing outcomes for defined perturbations in naïve and primed pluripotent stem cells

While previous global profiling genomic studies have indicated transcriptional and epigenetic differences between naïve and primed pluripotent states, limited knowledge is available on whether cardinal differences exist in their lineage decision

making that go beyond dependence on distinct signaling pathways in response to defined molecular perturbations. In addition to *Mettl3*, depletion of multiple epigenetic repressors was found to promote EpiSC differentiation (Fig. 41), but not of naïve ESCs. This includes polycomb components *Eed* and *Suz12*, whom have been previously shown to be dispensable for naïve murine ESC stability. The identification of *Dnmt1*, is also consistent with previous studies showing the *Dnmt1* KO ESCs are viable and naïve ESCs are hypo-methylated, while EpiSCs upregulate DNA methylation towards that of somatic cells. *Dnmt1* KO is lethal at the post-implantation stage and *Dnmt1* KO ESCs can be from KO blastocysts, reminiscent to the phenotypes described herein for *Mettl3* KO.

The fact that murine naïve cells, rather than primed cells, are tolerant to depletion of epigenetic and transcriptional repressors supports the concept of naïve pluripotency, in comparison to primed pluripotent and somatic cells, as a configuration with a relatively minimal requirement for epigenetic repression. The divergent responses for naïve and primed pluripotent cells have direct implication on potential outcomes when analyzing potential regulators of pluripotency maintenance and induction, and possibly should be routinely taken into account in future studies. The latter may be particularly relevant when comparing ESCs in expanded in serum containing undefined conditions and from different genetic backgrounds.

Finally, we note that conventional human ESCs that are known to resemble to a large extent murine EpiSCs, do not tolerate complete and permanent ablation of a variety of epigenetic repressors including *METTL3* and *DNMT1* (unpublished observations). Thus, ability to tolerate ablation of such epigenetic repressors may be another one of the features of naïve pluripotency across different species. Therefore, it will be of great interest to evaluate whether newly devised conditions to generate MAPK independent naïve pluripotent cells may allow generation of such KO human pluripotent cell model systems.

Supplementary Tables

Supplementary Tables and Legends

Table S1. Summary of m⁶A peaks in mouse naïve ESCs, EBs and MEFs.

*To avoid mistakes due to low coverage, only MACS2-assigned peaks (FC \geq 2, FDR \leq 5%), that occur in genes with expression level above the lower quartile and were identified in at least two biological replicates, were considered. **Expressed genes were considered when RPKM $>$ 1 in two replicates. ***Percent of methylated genes was calculated from the total number of expressed genes.

Category	ESC	EB	MEF
Total # of peaks	11,617	9,282	12,369
Peaks in genes*	10,431	8,356	11,948
Genes with peaks	6,427	5,518	6,273
coding genes	6,331	5,453	5993
non-coding genes	96	65	280
All expressed genes**	12,206	12,392	12,638
% of methylated genes***	52.7%	44.5%	49.6%

Table S2. Numbers of common and unique m⁶A peaks in mouse naïve ESCs and EBs.

Common=overlapping peaks; Unique=non-overlapping peaks. * Due to differences in peak length 7,205 ESC peaks overlap 6,765 in EBs.

Peak	# of peaks in genes	# of genes with peaks
Common	7,205*	4,756
Unique ESC	3,226	2,703
Unique EB	1,591	1,407

Table S3. List of pluripotency promoting genes and their m⁶A mRNA methylation status. Y= methylated mRNA transcript, N= not methylated mRNA transcript.

Gene ID	Name	ESC	EB	MEF
383491	Prdm14	Y	N	N
50764	Fbx15	Y	N	N
73703	Dppa2	Y	N	N
16878	Lif	Y	N	Y
11614	Nr0b1	Y	Y	N
140858	Wdr5	Y	Y	N
14472	Gbx2	Y	Y	N
20674	Sox2	Y	Y	N
21432	Tcl1	Y	Y	N
22286	Utf1	Y	Y	N
22702	Rex1	Y	Y	N
26380	Esrrb	Y	Y	N
26424	Nr5a2	Y	Y	N
353283	Eras	Y	Y	N
54427	Dnmt3l	Y	Y	N
58198	Sall1	Y	Y	N
71950	Nanog	Y	Y	N
73693	Dppa4	Y	Y	N
99377	Sall4	Y	Y	N
12224	Klf5	Y	Y	Y
16598	Klf2	Y	Y	Y
16600	Klf4	Y	Y	Y
16880	Lifr	Y	Y	Y
21386	Tbx3	Y	Y	Y
214133	Tet2	Y	Y	Y
52463	Tet1	Y	Y	Y
209446	Tfe3	N	N	Y
66991	Ecat1;Khdc3	N	Y	N
20848	Stat3	N	N	N
434423	Dppa5;Esg1	N	N	N
71981	Ecat8	N	N	N
73708	Dppa3	N	N	N
81879	Tfcp2l1	N	N	N
83557	Lin28	N	N	N
18999	Pou5f1	N	N	N

References

1. Evans, M. Discovering pluripotency: 30 years of mouse embryonic stem cells. *Nature Reviews Molecular Cell Biology* **12**, 680–686 (2011).
2. KLEINSMITH, L. J. & PIERCE, G. B. MULTIPOTENTIALITY OF SINGLE EMBRYONAL CARCINOMA CELLS. *Cancer Res.* **24**, 1544–1551 (1964).
3. Chambers, I. & Smith, A. Self-renewal of teratocarcinoma and embryonic stem cells. *Oncogene* **23**, 7150–7160 (2004).
4. Kahan, B. W. & Ephrussi, B. Developmental potentialities of clonal in vitro cultures of mouse testicular teratoma. *J. Natl. Cancer Inst.* **44**, 1015–1036 (1970).
5. Evans, M. J. & Kaufman, M. H. Establishment in culture of pluripotential cells from mouse embryos. *Nature* **292**, 154–156 (1981).
6. Martin, G. R. Isolation of a pluripotent cell line from early mouse embryos cultured in medium conditioned by teratocarcinoma stem cells. *Proc. Natl. Acad. Sci. U. S. A.* **78**, 7634–7638 (1981).
7. Thomson, J. A. Embryonic Stem Cell Lines Derived from Human Blastocysts. *Science* **282**, 1145–1147 (1998).
8. Xie, D. *et al.* Rewirable gene regulatory networks in the preimplantation embryonic development of three mammalian species. *Genome Res.* **20**, 804–815 (2010).
9. Jaenisch, R. & Mintz, B. Simian virus 40 DNA sequences in DNA of healthy adult mice derived from preimplantation blastocysts injected with viral DNA. *Proc. Natl. Acad. Sci. U. S. A.* **71**, 1250–1254 (1974).
10. Bokar, J. A., Rath-Shambaugh, M. E., Ludwiczak, R., Narayan, P. & Rottman, F. Characterization and partial purification of mRNA N6-adenosine methyltransferase from HeLa cell nuclei. Internal mRNA methylation requires a multisubunit complex. *J. Biol. Chem.* **269**, 17697–17704 (1994).
11. Adewumi, O. *et al.* Characterization of human embryonic stem cell lines by the International Stem Cell Initiative. *Nat. Biotechnol.* **25**, 803–16 (2007).
12. de Souza, N. Testing pluripotency. *Nat. Methods* **8**, 287 (2011).
13. Boroviak, T., Loos, R., Bertone, P., Smith, A. & Nichols, J. The ability of inner-cell-mass cells to self-renew as embryonic stem cells is acquired following epiblast

- specification. *Nat. Cell Biol.* **16**, 516–28 (2014).
14. Briggs, R. & King, T. J. Transplantation of Living Nuclei From Blastula Cells into Enucleated Frogs' Eggs. *Proc. Natl. Acad. Sci. U. S. A.* **38**, 455–463 (1952).
 15. Gurdon, J. B., Elsdale, T. R. & Fischberg, M. Sexually mature individuals of *Xenopus laevis* from the transplantation of single somatic nuclei. *Nature* **182**, 64–65 (1958).
 16. Tachibana, M. *et al.* Human Embryonic Stem Cells Derived by Somatic Cell Nuclear Transfer. *Cell* **153**, 1228–1238 (2013).
 17. Takahashi, K. & Yamanaka, S. Induction of Pluripotent Stem Cells from Mouse Embryonic and Adult Fibroblast Cultures by Defined Factors. *Cell* **126**, 663–676 (2006).
 18. Hanna, J. *et al.* Direct Reprogramming of Terminally Differentiated Mature B Lymphocytes to Pluripotency. *Cell* **133**, 250–264 (2008).
 19. Takahashi, K. *et al.* Induction of Pluripotent Stem Cells from Adult Human Fibroblasts by Defined Factors. *Cell* **131**, 861–872 (2007).
 20. Brons, I. G. M. *et al.* Derivation of pluripotent epiblast stem cells from mammalian embryos. *Nature* **448**, 191–195 (2007).
 21. Li, E. Chromatin modification and epigenetic reprogramming in mammalian development. *Nat. Rev. Genet.* **3**, 662–673 (2002).
 22. Cantara, W. a. *et al.* The RNA modification database, RNAMDB: 2011 update. *Nucleic Acids Res.* **39**, 195–201 (2011).
 23. Saletore, Y. *et al.* The birth of the Epitranscriptome: deciphering the function of RNA modifications. *Genome Biol.* **13**, 175 (2012).
 24. Dominissini, D. *et al.* Topology of the human and mouse m6A RNA methylomes revealed by m6A-seq. *Nature* **485**, 201–206 (2012).
 25. Jia, G. *et al.* N6-Methyladenosine in nuclear RNA is a major substrate of the obesity-associated FTO. *Nature Chemical Biology* **7**, 885–887 (2011).
 26. Desrosiers, R., Friderici, K. & Rottman, F. Identification of methylated nucleosides in messenger RNA from Novikoff hepatoma cells. *Proc. Natl. Acad. Sci. U. S. A.* **71**, 3971–5 (1974).
 27. Perry, R. P. & Kelley, D. E. Existence of methylated messenger RNA in mouse L

- cells. *Cell* **1**, 37–42 (1974).
28. Kane, S. E. & Beemon, K. Precise localization of m6A in Rous sarcoma virus RNA reveals clustering of methylation sites: implications for RNA processing. *Mol. Cell. Biol.* **5**, 2298–306 (1985).
 29. Dimock, K. & Stoltzfus, C. M. Sequence specificity of internal methylation in B77 avian sarcoma virus RNA subunits. *Biochemistry* **16**, 471–478 (1977).
 30. Beemon, K. & Keith, J. Localization of N6-methyladenosine in the Rous sarcoma virus genome. *J. Mol. Biol.* **113**, 165–179 (1977).
 31. Nichols, J. L. & Welder, L. Nucleotides adjacent to N6-methyladenosine in maize poly(A)-containing RNA. *Plant Sci. Lett.* **21**, 75–81 (1981).
 32. Liu, J. & Jia, G. Methylation Modifications in Eukaryotic Messenger RNA. *Journal of Genetics and Genomics* **41**, 21–33 (2014).
 33. Meyer, K. D. *et al.* Comprehensive analysis of mRNA methylation reveals enrichment in 3' UTRs and near stop codons. *Cell* **149**, 1635–1646 (2012).
 34. Liu, J. *et al.* A METTL3-METTL14 complex mediates mammalian nuclear RNA N(6)-adenosine methylation. *Nat. Chem. Biol.* **10**, 93–5 (2014).
 35. Ping, X.-L. *et al.* Mammalian WTAP is a regulatory subunit of the RNA N6-methyladenosine methyltransferase. *Cell Res.* **24**, 177–189 (2014).
 36. Wang, Y. *et al.* N(6)-methyladenosine modification destabilizes developmental regulators in embryonic stem cells. *Nat. Cell Biol.* **16**, 191–8 (2014).
 37. Zheng, G. *et al.* ALKBH5 Is a Mammalian RNA Demethylase that Impacts RNA Metabolism and Mouse Fertility. *Mol. Cell* **49**, 18–29 (2013).
 38. Hess, M. E. *et al.* The fat mass and obesity associated gene (Fto) regulates activity of the dopaminergic midbrain circuitry. *Nat. Neurosci.* **16**, 1042–8 (2013).
 39. Wang, X. *et al.* N6-methyladenosine-dependent regulation of messenger RNA stability. *Nature* **505**, 117–20 (2014).
 40. Rais, Y. *et al.* Deterministic direct reprogramming of somatic cells to pluripotency. *Nature* **502**, 65–70 (2013).
 41. Cong, L. *et al.* Multiplex genome engineering using CRISPR/Cas systems. *Science* **339**, 819–23 (2013).
 42. Stadtfeld, M., Maherali, N., Borkent, M. & Hochedlinger, K. A reprogrammable

- mouse strain from gene-targeted embryonic stem cells. *Nat. Methods* **7**, 53–5 (2010).
43. Trapnell, C. & Salzberg, S. L. How to map billions of short reads onto genomes. *Nat. Biotechnol.* **27**, 455–457 (2009).
 44. Anders, S., Pyl, P. T. & Huber, W. HTSeq – A Python framework to work with high-throughput sequencing data HTSeq – A Python framework to work with high-throughput sequencing data. *Bioinformatics.* **31**, 0–5 (2014).
 45. Anders, S. & Huber, W. Differential expression analysis for sequence count data. *Genome Biol.* **11**, R106 (2010).
 46. Robinson, M. D., McCarthy, D. J. & Smyth, G. K. edgeR: a Bioconductor package for differential expression analysis of digital gene expression data. *Bioinformatics* **26**, 139–40 (2010).
 47. Dominissini, D., Moshitch-Moshkovitz, S., Salmon-Divon, M., Amariglio, N. & Rechavi, G. Transcriptome-wide mapping of N(6)-methyladenosine by m(6)A-seq based on immunocapturing and massively parallel sequencing. *Nat. Protoc.* **8**, 176–89 (2013).
 48. Machanick, P. & Bailey, T. L. MEME-ChIP: Motif analysis of large DNA datasets. *Bioinformatics* **27**, 1696–1697 (2011).
 49. Quinlan, A. R. & Hall, I. M. BEDTools: A flexible suite of utilities for comparing genomic features. *Bioinformatics* **26**, 841–842 (2010).
 50. Kent, W. J. *et al.* The Human Genome Browser at UCSC. *Genome Res.* **12**, 996–1006 (2002).
 51. Langmead, B. & Salzberg, S. L. Fast gapped-read alignment with Bowtie 2. *Nat Methods* **9**, 357–359 (2012).
 52. Chen, C. Y. A., Ezzeddine, N. & Shyu, A. Bin. Chapter 17 Messenger RNA Half-Life Measurements in Mammalian Cells. *Methods in Enzymology* **448**, 335–357 (2008).
 53. Sharova, L. V. *et al.* Database for mRNA half-life of 19 977 genes obtained by DNA microarray analysis of pluripotent and differentiating mouse embryonic stem cells. *DNA Res.* **16**, 45–58 (2009).
 54. Stern-Ginossar, N. *et al.* Decoding human cytomegalovirus. *Science* **338**, 1088–93

- (2012).
55. Ingolia, N. T., Lareau, L. F. & Weissman, J. S. Ribosome profiling of mouse embryonic stem cells reveals the complexity and dynamics of mammalian proteomes. *Cell* **147**, 789–802 (2011).
 56. Chew, G.-L. *et al.* Ribosome profiling reveals resemblance between long non-coding RNAs and 5' leaders of coding RNAs. *Development* **140**, 2828–2834 (2013).
 57. Guttman, M., Russell, P., Ingolia, N. T., Weissman, J. S. & Lander, E. S. Ribosome profiling provides evidence that large noncoding RNAs do not encode proteins. *Cell* **154**, 240–251 (2013).
 58. Perez-Cornejo, P. *et al.* Anoctamin 1 (Tmem16A) Ca²⁺-activated chloride channel stoichiometrically interacts with an ezrin-radixin-moesin network. *Proc. Natl. Acad. Sci.* **109**, 10376–10381 (2012).
 59. Shen, S. *et al.* MATS: A Bayesian framework for flexible detection of differential alternative splicing from RNA-Seq data. *Nucleic Acids Res.* **40**, (2012).
 60. Porath, H. T., Carmi, S. & Levanon, E. Y. A genome-wide map of hyper-edited RNA reveals numerous new sites. *Nat. Commun.* **5**, 4726 (2014).
 61. Dobin, A. *et al.* STAR: Ultrafast universal RNA-seq aligner. *Bioinformatics* **29**, 15–21 (2013).
 62. Pinto, Y., Cohen, H. Y. & Levanon, E. Y. Mammalian conserved ADAR targets comprise only a small fragment of the human editosome. *Genome Biol.* **15**, R5 (2014).
 63. Picardi, E. & Pesole, G. REDIttools: High-throughput RNA editing detection made easy. *Bioinformatics* **29**, 1813–1814 (2013).
 64. Iwanami, Y. & Brown, G. M. Methylated bases of ribosomal ribonucleic acid from HeLa cells. *Arch. Biochem. Biophys.* **126**, 8–15 (1968).
 65. Havugimana, P. C. *et al.* A census of human soluble protein complexes. *Cell* **150**, 1068–1081 (2012).
 66. Bokar, J. A. *in Fine-Tuning of RNA Functions by Modification and Editing.* (2005).
 67. Guo, G. *et al.* Klf4 reverts developmentally programmed restriction of ground state

- pluripotency. *Development* **136**, 1063–1069 (2009).
68. Factor, D. C. *et al.* Epigenomic comparison reveals activation of ‘seed’ enhancers during transition from naive to primed pluripotency. *Cell Stem Cell* **14**, 854–863 (2014).
 69. Marks, H. *et al.* The transcriptional and epigenomic foundations of ground state pluripotency. *Cell* **149**, 590–604 (2012).
 70. Acampora, D., Di Giovannantonio, L. G. & Simeone, A. Otx2 is an intrinsic determinant of the embryonic stem cell state and is required for transition to a stable epiblast stem cell condition. *Development* **140**, 43–55 (2013).
 71. Betschinger, J. *et al.* Exit from pluripotency is gated by intracellular redistribution of the bHLH transcription factor Tfe3. *Cell* **153**, 335–347 (2013).
 72. Schwartz, S. *et al.* High-Resolution mapping reveals a conserved, widespread, dynamic mRNA methylation program in yeast meiosis. *Cell* **155**, 1409–1421 (2013).
 73. Heilman, K. L., Leach, R. A. & Tuck, M. T. Internal 6-methyladenine residues increase the in vitro translation efficiency of dihydrofolate reductase messenger RNA. *Int. J. Biochem. Cell Biol.* **28**, 823–829 (1996).
 74. Meyer, K. D. & Jaffrey, S. R. The dynamic epitranscriptome: N6-methyladenosine and gene expression control. *Nat. Rev. Mol. Cell Biol.* **15**, 313–26 (2014).
 75. Karikó, K. *et al.* Incorporation of pseudouridine into mRNA yields superior nonimmunogenic vector with increased translational capacity and biological stability. *Mol. Ther.* **16**, 1833–1840 (2008).
 76. Bass, B. L. RNA editing by adenosine deaminases that act on RNA. *Annu. Rev. Biochem.* **71**, 817–846 (2002).
 77. Savva, Y. a, Rieder, L. E. & Reenan, R. a. The ADAR protein family. *Genome Biol.* **13**, 252 (2012).
 78. Batista, P. J. *et al.* M⁶A RNA modification controls cell fate transition in mammalian embryonic stem cells. *Cell Stem Cell* **15**, 707–719 (2014).

Student declaration

I hereby declare that the thesis presented summarizes my independent research work under the supervision of Dr. Jacob H. Hanna at the Department of Molecular Genetics, the Weismann Institute of Science. Mirie Zerbib conducted microinjections in mice blastocysts. Dr. Noa Novershtern analyzed the m⁶A-seq and RNA-seq Data. Dr. Abed AlFatah Mansour assisted in and supervised microscopy imaging and analysis. Dr. Noam Stern-Ginossar help with the Ribo-seq preparation and analysis. This work done in collaboration with Prof. Gideon Rechavi, Dr. Dan Dominissini and Dr. Sharon Moshitch-Moshkovitz (Sheba Hospital, Israel).

List of publication during the course of the Ph.D.

1. I. Maza, I. Caspi, A. Zviran, E. Chomsky, Y. Rais, S. Viukov, **S. Geula**, J. D. Buenrostro, L. Weinberger, V. Krupalnik, S. Hanna, M. Zerbib, J. R. Dutton, W. J. Greenleaf, R. Massarwa, N. Novershtern, and J. H. Hanna, “**Transient acquisition of pluripotency during somatic cell transdifferentiation with iPSC reprogramming factors.**” *Nature Biotechnology*, vol. 33, no. 7, pp. 769–774, 2015.
2. **S. Geula**, S. Moshitch-Moshkovitz, D. Dominissini, A. A. Mansour, N. Kol, M. Salmon-Divon, V. Hershkovitz, E. Peer, N. Mor, Y. S. Manor, M. S. Ben-Haim, E. Eyal, S. Yunger, Y. Pinto, D. A. Jaitin, S. Viukov, Y. Rais, V. Krupalnik, E. Chomsky, M. Zerbib, I. Maza, Y. Rechavi, R. Massarwa, S. Hanna, I. Amit, E. Y. Levanon, N. Amariglio, N. Stern-Ginossar, N. Novershtern, G. Rechavi, and J. H. Hanna, “**m⁶A mRNA methylation facilitates resolution of naïve pluripotency toward differentiation.**” *Science*, vol. 347, no. 6225, pp. 1002–6, 2015.
3. O. Gafni, L. Weinberger, A. A. Mansour, Y. S. Manor, E. Chomsky, D. Ben-Yosef, Y. Kalma, S. Viukov, I. Maza, A. Zviran, Y. Rais, Z. Shipony, Z. Mukamel, V. Krupalnik, M. Zerbib, **S. Geula**, I. Caspi, D. Schneir, T. Shwartz, S. Gilad, D. Amann-Zalcenstein, S. Benjamin, I. Amit, A. Tanay, R. Massarwa, N. Novershtern, and J. H. Hanna, “**Derivation of novel human ground state naïve pluripotent stem cells.**” *Nature*, vol. 504, pp. 282–6, 2013.
4. Y. Rais*, A. Zviran*, **S. Geula***, O. Gafni, E. Chomsky, S. Viukov, A. A. Mansour, I. Caspi, V. Krupalnik, M. Zerbib, I. Maza, N. Mor, D. Baran, L. Weinberger, D. a. Jaitin, D. Lara-Astiaso, R. Blecher-Gonen, Z. Shipony, Z. Mukamel, T. Hagai, S. Gilad, D. Amann-Zalcenstein, A. Tanay, I. Amit, N. Novershtern, and J. H. Hanna, “**Deterministic direct reprogramming of somatic cells to pluripotency.**” *Nature*, vol. 502, pp. 65–70, 2013. (238 citations)
* First author equal contribution
5. A.A. Mansour, O. Gafni, L. Weinberger, A. Zviran, M. Ayyash, Y. Rais, V. Krupalnik, M. Zerbib, D. Amann-Zalcenstein, I. Maza, **S. Geula**, S. Viukov, L. Holtzman, A. Pribluda, E. Canaani, S. Horn-Saban, I. Amit, N. Novershtern, and J. H. Hanna, “**The H3K27 demethylase Utx regulates somatic and germ cell epigenetic reprogramming.**” *Nature*, vol. 488, pp. 409–413, 2012.

Acknowledgements

It is hard for me to grasp the long way that I have done during my PhD studies. And it is even harder to imagine such a journey coming to an end. Therefore, I want to thank all of my lab members that were first of all great friends, and the best colleagues that any young student can wish for. I thank my mentor Jacob Hanna that helped navigate the ship and fight very hard to push my research as higher as it can go. I know that you worked and sacrificed no less than I did. I want to thank my family that supported me in any way they could, you made my academic path much easier. Last but not least, I thank my wife Dana. You helped me see that life has more things to offer other than the lab neon lights. Meeting you was the true gift from this PhD.